Calibration and Response of the High Pseudorapidity Region of the ATLAS Liquid Argon End-cap Calorimeters

by

Warren Shaw
B.Sc., Physics, University of Calgary, 2000
B.Sc., Astrophysics, University of Calgary, 2000

A Thesis Submitted in Partial Fullfillment of the
Requirements for the Degree of
MASTER OF SCIENCE
in the Department of Physics and Astronomy

© Warren Shaw, 2006
University of Victoria

All rights reserved. This thesis may not be reproduced in whole or in part, by photocopy or other means, without the permission of the author.

Calibration and Response of the High Pseudorapidity Region of the ATLAS Liquid Argon End-cap Calorimeters

by

Warren Shaw
B.Sc., Physics, University of Calgary, 2000
B.Sc., Astrophysics, University of Calgary, 2000

Supervisory Committee

Dr. R. K. Keeler

Supervisor (Department of Physics and Astronomy)

Dr. R. McPherson

Supervisor (Department of Physics and Astronomy)

Dr. M. Lefebvre

Departmental Member (Department of Physics and Astronomy)

Dr. C. Bohne

Outside Member (Department of Chemistry)

Dr. M. Vetterli

External Examiner (Simon Fraser University)

Supervisory Committee

Dr. R. K. Keeler

Supervisor (Department of Physics and Astronomy)

Dr. R. McPherson

Supervisor (Department of Physics and Astronomy)

Dr. M. Lefebvre

Departmental Member (Department of Physics and Astronomy)

Dr. C. Bohne

Outside Member (Department of Chemistry)

Dr. M. Vetterli

External Examiner (Simon Fraser University)

Abstract

In preparation for the ATLAS experiment at the LHC at CERN, the high pseudorapidity region ($|\eta| > 2.5$) of the ATLAS end-cap liquid argon calorimeters underwent particle beam testing in 2004. One of the main goals of these tests is to study energy reconstruction in the complex interface region between the electromagnetic, hadronic, and forward calorimeters at $|\eta| \sim 3.2$. These detectors were exposed to beams of electrons and pions with energies ranging from 6 GeV to 200 GeV. Three methods of calibration in the electromagnetic end-cap calorimeter (EMEC) are studied and compared to the results of a previous beam test of the EMEC. The electromagnetic scale factor (α_{EM}) is computed and compared to the previous beam test value. Studies of the energy response and resolution of the high pseudorapidity region of the three end-cap calorimeters to the particle beam position scans are given.

Table of Contents

Supervisory Committee ii

Abstract iii

Table of Contents iv

List of Figures vii

List of Tables xi

Glossary of Abbreviations xii

Acknowledgements xiv

Dedication xvi

1 Introduction 1

1.1 The LHC Environment 3

1.2 The ATLAS Experiment 5

1.3 Calorimeter Beam Tests 7

1.4 Calibration and Response 8

2 ATLAS Liquid Argon Calorimetry **10**

2.1 Electromagnetic Showers 12

2.1.1 Electromagnetic Interactions 12

2.1.2 Electromagnetic Shower Size 17

2.2 Hadronic Showers 20

2.2.1 Particle sector 22

2.2.2 Nuclear Sector 24

2.2.3 Hadronic Shower Size 26

2.2.4 EM Energy Scale 27

2.3 ATLAS End-Cap Calorimeters 28

2.3.1 EMEC 29

2.3.2 HEC 34

2.3.3 FCAL 36

3 Experimental Setup for Particle Beam Tests **40**

3.1 Beam Detectors 41

3.2 Calorimeter Module Setup 44

3.3 Modified Setup for Period 2 54

3.4 Impact Points and Detector Layers 57

4 Signal Reconstruction **65**

4.1 Event Pre-selection 65

4.2 Signal Shape and Digitization 67

4.3 Gain mode 69

4.4 Pedestals 69

4.5 Event Phase and Pulse Shape Accumulation 70

4.6 Digital Filtering 71

5 EMEC Calibration **73**

5.1 Calibration Coefficients Overview 75

5.2 EMEC Ramp Study 77

5.2.1 Calibration Runs 77

5.2.2 Ramp Calibration Methods and Comparison 80

5.3 DAC to μA Conversion 94

5.4 μA to MeV Conversion 97

5.5 Calibration Signal to Physics Signal correction 98

5.6 EMEC HV-dependent correction 100

6 Calorimeter Energy Response **103**

6.1 Clustering Algorithms 103

6.2 Event Selection 106

6.3 Calorimeter y-Scans 110

6.4 Electron/Positron y-Scan Results 114

6.4.1 Calculation of α_{EM} for the EMEC 126

6.5 Pion y-Scan Results 128

7 Conclusions and Outlook **135**

References **138**

List of Figures

1.1 General overall view of the LHC experiments. 4
1.2 The ATLAS detector. 5
1.3 The pseudorapidity region of the ATLAS end-cap calorimeter exposed to particle beams in the 2004 combined beam tests. 9

2.1 Illustration of the ATLAS calorimeters. 11
2.2 Fractional energy loss per unit length in lead as a function of electron or positron energy [2]. 13
2.3 Photon cross sections for different energy loss mechanisms in lead as a function of photon energy [2]. 14
2.4 Energy classifications within a typical hadronic shower profile [17, 18]. 21
2.5 Schematic of the end-cap cryostat containing the EMEC, HEC, and FCAL detectors [14]. 29
2.6 Schematic of the inner and outer wheels of the full EMEC (left) and a single module (right) [20]. 30
2.7 Illustration (left) of the EMEC inner wheel electrode structure between two lead absorber plates, and the equivalent circuit (right). 32
2.8 EMEC and HEC cell volumes and segmentation [18]. 34

2.9 Schematic of the HEC illustrating the dimensions (in mm) of the two HEC wheels [14]. 35
2.10 HEC electrode structure between two copper absorber plates [14]. . . 37
2.11 Diagram of the FCAL liquid argon gap structure [14]. 38

3.1 Layout of the testbeam setup as viewed from above 42
3.2 The end-cap calorimeter modules before being lowered into the cryostat. 46
3.3 View of the calorimeter modules looking down into the cryostat. . . . 47
3.4 Side view of the EMEC, HEC, and FCAL testbeam modules. 48
3.5 Front view of the EMEC, HEC, and FCAL testbeam modules. 50
3.6 The FCAL1 and FCAL2 modules, along with the CTC. 52
3.7 Front view of the EMEC, HEC, and FCAL testbeam modules during period 2. 56
3.8 Schematic of the EMEC inner wheel front layer (sampling 2). 58
3.9 Schematic of the EMEC inner wheel back layer (sampling 3). 59
3.10 Schematic of the HEC1 wheel front layer (sampling 1). 60
3.11 Schematic of the HEC1 wheel back layer (sampling 2), and the FCAL 1 module. 61
3.12 Schematic of the HEC2 wheel front layer (sampling 3), and the FCAL 2 module. 62
3.13 Schematic of the CTC ϕ-section. 63
3.14 Schematic of the CTC η-section. 64

4.1 Typical signal shapes: the triangular ionization shape produced in the LAr gap, and the readout physics pulse shape with time samples (points) indicated [14]. 68

5.1 Illustration of an EMEC liquid argon cell circuit [32]. 74
5.2 Typical EMEC channel ramp calibration graph for high gain mode. . 79
5.3 Linear (top) and quadratic (bottom) ramp calibration coefficients at high gain for the EMEC inner wheel. 81
5.4 Linear (top) and quadratic (bottom) ramp calibration coefficients at medium gain for the EMEC inner wheel. 82
5.5 Examples of EMEC calibration pulse shapes for two front layer channels (top) and two back layer channels (bottom). 84
5.6 Linear ramp coefficient ($P1$) obtained from the parabolic interpolation method, plotted as a function of delay for four typical EMEC channels. 86
5.7 Linear ramp coefficient ($P1$) obtained from the calibration pulse shape method, plotted as a function of delay for four typical EMEC channels. 89
5.8 A sample calibration pulse shape for an EMEC channel at medium gain that is missing delay data. 90
5.9 Schematic diagram of the calibration and readout chain. 95
5.10 Pulse shape response to a physics signal and a calibration signal of the same initial current. 99
5.11 High voltage variation along η in the EMEC. 100
5.12 Schematic of a flat inner wheel electrode showing the two HV sectors. 101

6.1 Histograms of the energy response of the calorimeters to a 120 GeV e^+ beam at impact point B in the EMEC. 108
6.2 Histograms of the energy response of the calorimeters to a 120 GeV e^+ beam at impact point H in the FCAL. 109
6.3 Front view of the central region of the testbeam modules during period 2. 111

6.4 Gaussian fit to the reconstructed cluster energy distribution of a 120 GeV e^+ beam at impact point B in the EMEC. 115

6.5 Gaussian fit to the reconstructed cluster energy distribution of a 120 GeV e^+ beam at impact point G. 116

6.6 Calorimeter response (top) and resolution (bottom) as a function of cluster pseudorapidity to electron and positron beam vertical scans. . 118

6.7 Calorimeter response to the 193 GeV e^- y-scan (top) and the 120 GeV e^+ y-scan (bottom) as a function of mean cluster pseudorapidity. . . . 121

6.8 Calorimeter response to the 60 GeV positron y-scan at $x = 0$ mm (top) and the 60 GeV positron y-scan at $x = -120$ mm (bottom) as a function of mean cluster pseudorapidity. 122

6.9 Calorimeter resolution as a function of beam energy for two of the y-scan impact points. 125

6.10 The reconstructed signal (in μA) plotted as a function of pseudorapidity for a 193 GeV electron y-scan of the EMEC inner wheel. 127

6.11 Calorimeter response (top) and resolution (bottom) as a function of cluster pseudorapidity to pion vertical scans. 130

6.12 Calorimeter response to the 200 GeV π^- y-scan (top), the 120 GeV π^- y-scan (middle), and the 60 GeV π^+ y-scan (bottom) as a function of mean cluster pseudorapidity. 132

6.13 Calorimeter resolution as a function of pion beam energy for two of the y-scan impact points. 134

List of Tables

2.1 End-cap calorimeter material properties. 18

3.1 Dimensions of several beam line scintillation counters. 43

3.2 Period 2 cryostat position with respect to the original testbeam coordinate system. 55

4.1 Gain modes for the different calorimeters in the beam test. 69

5.1 Calibration runs used for the EMEC ramp study. 78

5.2 EMEC inner wheel calibration resistances (in Ω). 97

6.1 Data run numbers used in $e^{\pm}$ particle beam y-scans. 112

6.2 Data run numbers used in $\pi^{\pm}$ particle beam y-scans. 113

Glossary of Abbreviations

ADC	Analog to Digital Converter
ATLAS	A Toroidal LHC ApparatuS
CBT-EC2	The second Combined Beam Test of the End-cap Calorimeter
CERN	European Organization for Nuclear Research
CTC	Cold Tail-Catcher
DAC	Digital to Analog Converter
EM	Electromagnetic
EMEC	Electromagnetic End-cap Calorimeter
FCAL	Forward Calorimeter
FEB	Front End Board
FEC	Front End Crate
FT	FeedThrough
HEC	Hadronic End-cap Calorimeter
HV	High Voltage
HWID	HardWare IDentifier
IW	Inner Wheel
LAr	Liquid Argon
LHC	Large Hadron Collider

OFC	Optimal Filtering Coefficients
SPS	Super Proton Synchrotron
TDC	Time to Digital Converter
WTC	Warm Tail-Catcher

Acknowledgements

I would like to acknowledge my supervisors, Richard and Rob, for all their help during my graduate studies. Richard, thank you for your knowledge, guidance and support every week, for patiently proofreading the drafts of this thesis, and for all the wise revisions. Rob, thank you for helping me get going with ATHENA, for all your knowledge, technical assistance, and bug-fixes that helped move this research forward, and for always being just an email away.

My gratitude is extended to everyone in the ATLAS group at UVic for their support and the many helpful discussions along the way. Specifically, I'd like to thank Michel for his inspiring teaching style, willingness to answer my many questions, and for making me feel like a colleague when we were working together at CERN; also Tayfun and Tamara for helping me get going on ATLAS when I first started grad school. Also, cheers to all the others that I had the privilege of working with on ATLAS; especially Marco (my testbeam sympathizer) for all the help, and Malachi for getting me away from CERN and into the Alps.

I'd like to thank my fellow grad-students at UVic for making this such a fun place to study and work. I'd especially like to thank Gabe and Matek for the serious study sessions in the office, the lunch adventures, but mostly for their friendship.

Last but certainly not least, I'd like to thank those who have been closest to

me and have supported me behind the scenes throughout my time as a grad student: God for His grace and provision, and for blessing me with this experience; my family (Mom, Dad, Heather and Carl) for always supporting me and encouraging me in all I do; and my wonderful wife Carla Rae—thank you for your love, encouragement, and for always believing in me.

To Carla Rae,

for marrying a grad student.

Chapter 1

Introduction

Particle physics is the study of the structure of matter at the most fundamental level, and the interactions between the constituents. The current understanding of how nature works at this level is called the Standard Model[1]. Experiments in particle physics test this model, and provide opportunities for the discovery of new physics beyond the Standard Model.

One branch of experimental particle physics probes nature at the smallest scale through the use of high energy particle colliders. A collider is a machine that accelerates particles to relativistic speeds, giving them a large amount of energy, and then brings them into collision with similarly accelerated particles traveling in the opposite direction. A new energy frontier will be reached with the completion of the Large Hadron Collider (LHC) [3] in 2007 at the European Organization for Nuclear Research (CERN) facility. The LHC will provide the deepest experimental probe of

[1]See references [1], [2], and references therein.

the constituents of matter yet achieved.

A given collision at the LHC will result in energetic particles emerging from the collision point while still conserving the energy and momentum of the colliding protons. By surrounding the collision point with a detector capable of measuring the properties of the emerging particles, information about the underlying interaction can be reconstructed. ATLAS (A Toroidal LHC ApparatuS) [4] [5] is an experiment located at one of the collision points at the LHC. The ATLAS collaboration was formed in 1992, and the ATLAS detector will begin taking data in 2007.

Tests of the different ATLAS detector sub-systems have occurred from the time of prototype development through to the present. These tests ensure that the detector is built to the specifications required to meet the experimental goals, and they also provide a means to calibrate the detector and study its response before the experiment begins. This thesis focuses on tests that were performed on a specific region of the ATLAS detector, namely the liquid argon end-cap calorimeters. Sections of the ATLAS end-cap calorimeters were exposed to beams of particles, and the calibration and response of these detectors is studied. This thesis looks at the calibration of the inner wheel of the electromagnetic end-cap calorimeter (EMEC), as well as the response of all end-cap calorimeters to particle beams.

The four sections in this initial chapter provide: an introduction to the LHC environment at CERN, an overview of the ATLAS experiment, background information on the previous end-cap calorimeter beam tests with motivation as to why

the latest beam tests are necessary, and an overview of the calibration and response studies performed.

1.1 The LHC Environment

The Large Hadron Collider is currently under construction at CERN. It is a circular accelerator with a circumference of 27 km, and is built approximately 100 m underground straddling the Switzerland-France border (figure 1.1). The LHC accelerates two counter-rotating beams of protons. The beams each consist of proton bunches separated in time by 25 ns. These beams are brought into collision at four locations around the LHC ring, one of which is at the center of ATLAS with a proton-proton center-of-mass collision energy of 14 TeV. The event rate in a collider, R, at which a given interaction process will occur is given by:

$$R = L\sigma, \tag{1.1}$$

where σ is the cross-section for the process, and the luminosity (L) is the factor of proportionality [2]. The design luminosity of the LHC is $L = 10^{34}$ cm^{-2}s^{-1}. With an estimated total inelastic cross-section[2] of 70 mb, the total inelastic proton-proton interaction rate at design luminosity is $R = 0.7 \times 10^9$ s^{-1}. The high luminosity will provide sufficient rates to study rare interactions: for example, the rate of producing

[2]Cross-sections are often expressed in barns (b) where 1 b = 10^{-28} m^2.

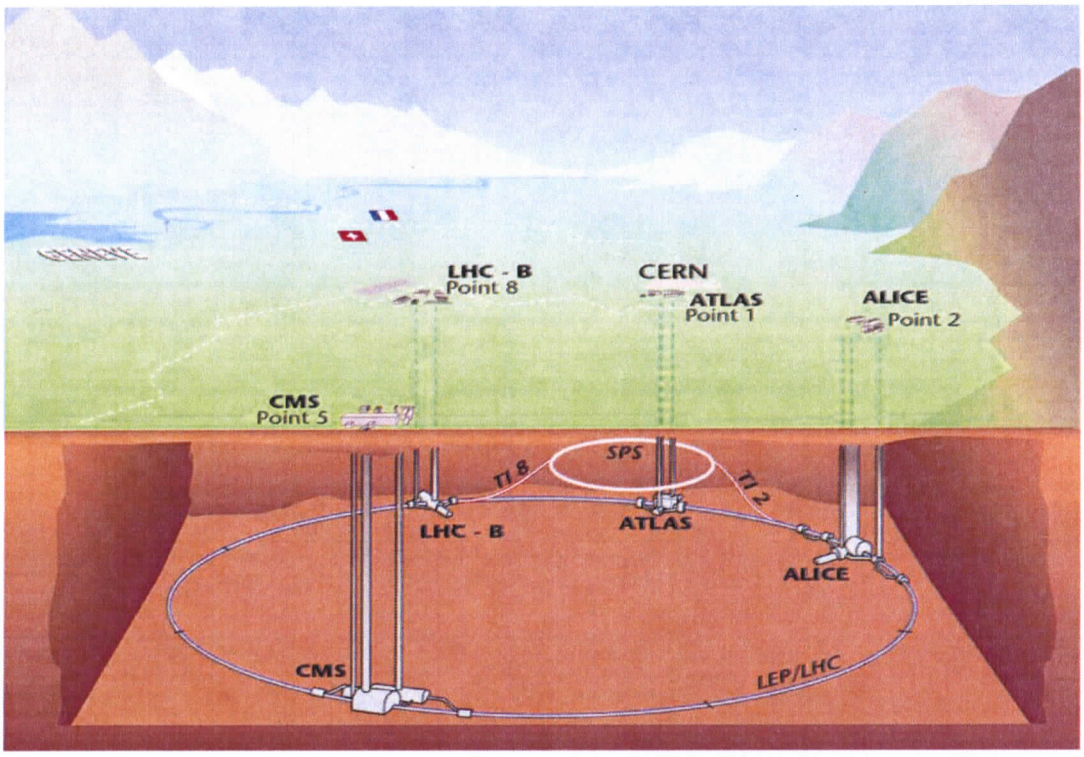

Figure 1.1: General overall view of the LHC experiments. ATLAS and CMS are general purpose detectors built for the discovery potential of the LHC environment. ALICE is a dedicated heavy ion experiment. LHCb will study b-physics and CP violation. The TOTEM experiment (located in the CMS forward region) will aim to measure the total p-p cross-section [3].

a top quark and anti-top quark, $pp \rightarrow t\bar{t} + X$, at this luminosity is $R \sim 6\ \mathrm{s}^{-1}$ [6, 7].

Combining LHC's high luminosity with its high proton collision energy makes the LHC environment rich with potential for more accurate measurements of Standard Model physics, especially the Higgs particle which is the only particle predicted by the Standard Model but not yet experimentally discovered, as well as discovery of new physics beyond the Standard Model.

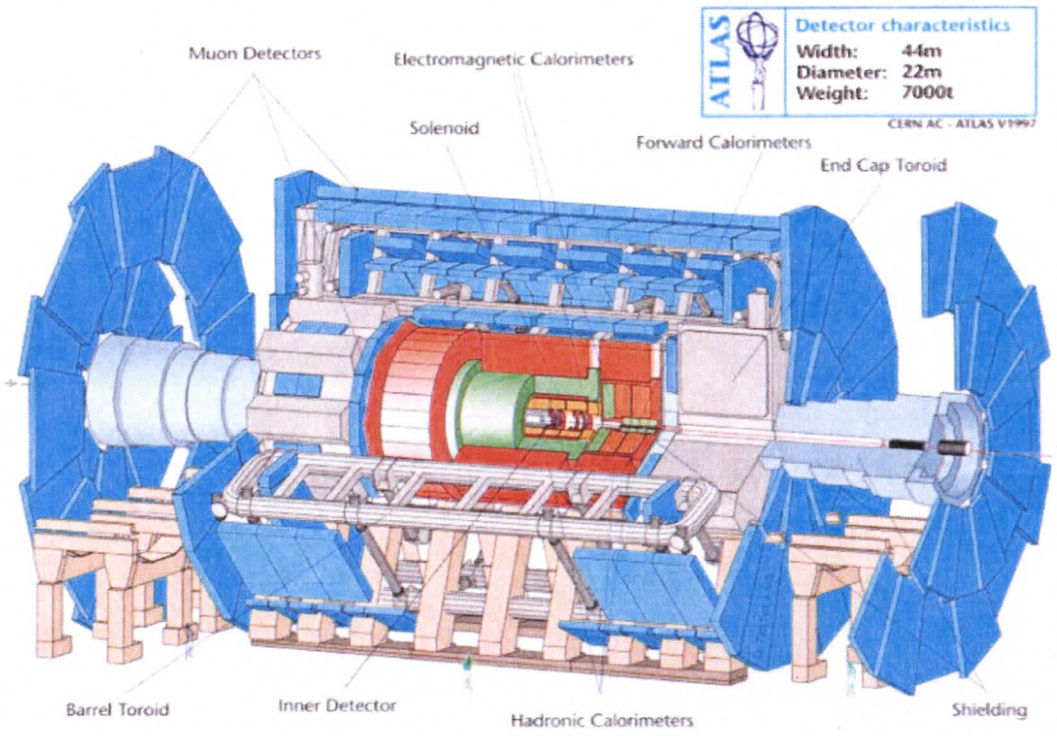

Figure 1.2: The ATLAS detector is a cylindrical apparatus which surrounds the LHC beam pipe, and is comprised of several detector systems. The muon detection system is shown in blue; the electromagnetic and hadronic calorimeters are shown in orange and green, respectively; the inner tracker is yellow. The central solenoid, along with the barrel and end-cap toroids, provide the magnetic fields used to bend the trajectories of charged particles to provide momentum measurement.

1.2 The ATLAS Experiment

Surrounding one of the collision points in the LHC is the ATLAS experiment. It is a general purpose detector designed to collect the maximum amount of information possible about the particles coming from the proton-proton collisions.

ATLAS has a complex design involving several detector systems, as shown in figure 1.2. Detectors are arranged in concentric shells: the inner most detect and mea-

sure charged particle momentum, followed by calorimeters for energy measurements, and finally a system to measure muon momentum. Specifically, collision products emerging from the interaction point first pass through the inner tracker in the presence of a magnetic field created by the central solenoid. The inner detector tracks the charged particles and measures their momentum through the radius of curvature of their trajectory in the magnetic field. Following the inner detector, particles interact with the electromagnetic and hadronic calorimeters, and all (except muons and neutrinos) are absorbed. In the process, the calorimeters measure the energy of the particles incident on the calorimeter face, and also aid in identifying the particle type and the trajectory. Chapter 2 will give a more detailed description of the principles of calorimetry, and of the ATLAS calorimeters.

Muons exit the calorimeter system and pass through the muon spectrometer system. The barrel and end-cap toroids produce the magnetic field bending the muon paths, and the three layers of muon detectors provide three sets of measurements from which the momentum and electric charge are obtained.

The only known particles that will escape ATLAS undetected are neutrinos. However, because ATLAS is a hermetic detector (it completely surrounds the collision point), except right along the beam pipe, neutrinos can be indirectly measured through the measurement of the event's missing transverse momentum.

The ATLAS detector is currently being installed at CERN. Commissioning studies and calibration activities are underway, and ATLAS is scheduled to be ready

to acquire data when the LHC starts up in 2007.

1.3 Calorimeter Beam Tests

As mentioned above, the ATLAS calorimetry system is responsible for measuring the energy of the particles emerging from a collision. Testing the calorimeters with well understood beams of energetic particles is an important step in preparing the ATLAS calorimeters for operation. Exposing the modules (components that make up the full detectors) to energetic beams of particles creates an environment as similar to ATLAS as possible before the LHC is operational. Through these particle beam tests the response and performance of the calorimeters are studied, and additionally, they allow other necessary components (electronics, cryogenics, software) to be tested.

There are three calorimeters in the ATLAS end-cap: the electromagnetic end-cap calorimeter (EMEC), the hadronic end-cap calorimeter (HEC), and the forward calorimeter (FCAL). Between 1996 and 2003 each of these calorimeters have individually undergone various stand-alone beam tests aimed mainly at quality control of module production [8, 9, 10]. In 2002, combined tests of the outer sections of the EMEC and HEC were performed using particle beams allowing for studies of position and energy resolution, and energy reconstruction methods [11, 12, 13].

However, none of the previous beam tests had all three end-cap calorimeters combined together for simultaneous testing. This was achieved in 2004 when modules

of the end-cap calorimeters located nearest to the beam pipe were exposed to beams of particles. One of the main purposes of this experiment is to study the energy reconstruction in the transition region between the three end-cap calorimeters [14]. The range in *pseudorapidity*[3], η, of the EMEC, HEC, and FCAL modules exposed to beams during the 2004 combined beam tests was from $|\eta| = 2.5$ to $|\eta| = 4.0$, and can be seen in figure 1.3. The principles of calorimetry and the general characteristics of the end-cap calorimeters are given in chapter 2. The details of the experimental setup for the 2004 combined beam tests are presented in chapter 3.

1.4 Calibration and Response

When one of the beam particles interacts with the ATLAS end-cap calorimeters an electric current is produced, and chapter 4 describes how that signal is reconstructed. Understanding the relationship between the energy deposited in a calorimeter cell and the reconstructed signal requires a cell-by-cell calibration of the detectors. Chapter 5 motivates and provides an overview of the calibration procedure for the ATLAS end-cap calorimeters, and also presents the EMEC calibration study performed as part of

[3]ATLAS can be described using a (z, θ, ϕ) coordinate system, where z points along the beam pipe, the polar angle θ is measured from the z-axis, and ϕ is the azimuthal angle. A useful variable to describe hadronic interactions is rapidity because the shape of the distributions expressed in rapidity are invariant under boosts in the z-direction [2]. Pseudorapidity is used to approximate rapidity when the mass (m) and momentum (p) of a particle is unknown (it assumes $p \gg m$). Therefore, in practice, the polar coordinate of particles emerging from a collision point, as well as of the coordinates of the detectors themselves, are expressed in terms of pseudorapidity, η, which is defined as:

$$\eta \equiv -\ln \tan\left(\frac{\theta}{2}\right). \tag{1.2}$$

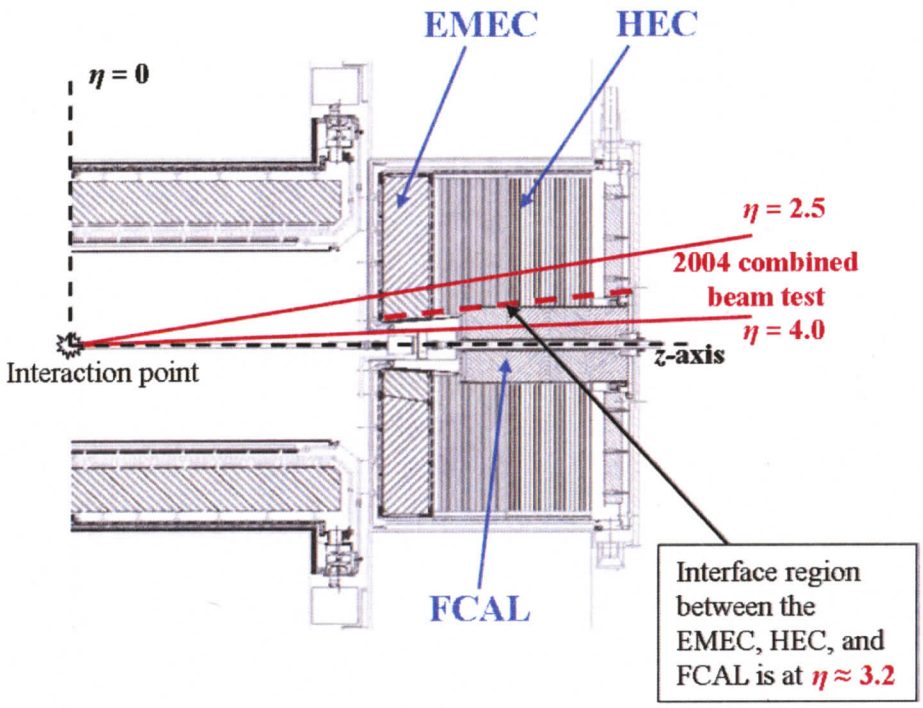

Figure 1.3: The pseudorapidity region of the ATLAS end-cap calorimeters exposed to particle beams in the 2004 combined beam tests. The EMEC, HEC, and FCAL calorimeters are described in chapter 2.

this thesis. Once the detectors are calibrated, their response to particle beams can be analyzed. Chapter 6 presents the response of the high pseudorapidity region of the end-cap calorimeter to beams of electrons/positrons and pions at energies of 60, 120, 193, and 200 GeV. Finally, chapter 7 gives some conclusions of the analysis presented here, and provides an outlook toward future research that would complement what has been completed here.

Chapter 2

ATLAS Liquid Argon Calorimetry

Calorimetry within the discipline of particle physics is essentially the detection and measurement of the energy of subatomic particles[1]. A calorimeter is a type of particle detector that absorbs the energy of incident particles, and in the process gives a measurable response that is proportional to the particle's energy. Sampling calorimeters consist of two components: a *passive* absorber material to degrade the energy of the incident particle, and an *active* material that produces the detectable signal. Calorimeters are sensitive to both neutral and charged particles over an energy range of several orders of magnitude. Particles interact with the calorimeter via strong or electromagnetic processes resulting in hadronic showers and electromagnetic showers.

The ATLAS calorimetry system uses sampling calorimeters with alternating layers of active and passive materials. The energy of the incident particle is measured

[1]Calorimeters also provide, to some extent, information regarding the position and type of incident particles.

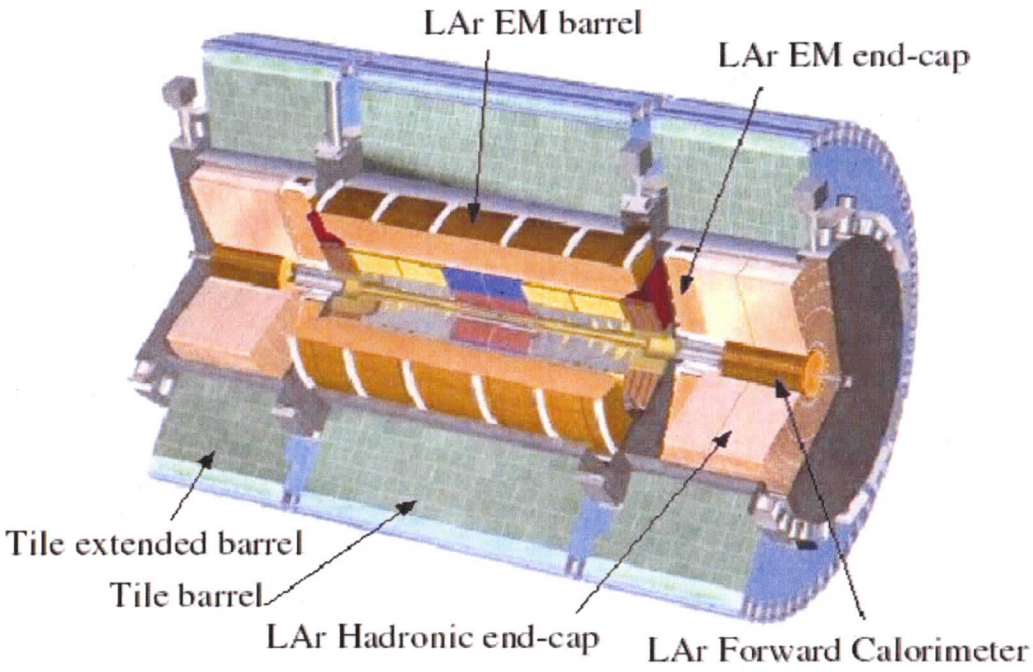

Figure 2.1: Illustration of the ATLAS calorimeters. The inner most calorimeters (orange) are liquid argon sampling calorimeters, and the outer calorimeters (green) are scintillating tile sampling calorimeters.

(sampled) only in the active layers. As figure 2.1 illustrates, ATLAS has two types of calorimeters: the first type use liquid argon (typically abbreviated as LAr) as the active material and have lead (Pb), copper (Cu), or tungsten (W) absorbers. Surrounding the LAr calorimeters are the Tile calorimeters that use plastic scintillator tiles (active material) embedded in a passive iron absorber which is also the flux return of the central ATLAS solenoid magnet. This thesis focuses on the LAr end-cap calorimeters.

In the first two sections of this chapter, the fundamentals of electromagnetic and hadronic showers are developed. Armed with the knowledge of how particles

interact with matter and how calorimeters measure particle energy, the ATLAS liquid argon end-cap calorimeters are then discussed in the third section of this chapter. Details of the LAr barrel and the tile calorimeters can be found in reference [14].

2.1 Electromagnetic Showers

When a proton-proton collision occurs at the center of the ATLAS detector, collision products may emerge in any direction and will impact the ATLAS calorimeters. If the particles are the electron (e^-), positron (e^+), or the photon (γ) they will predominantly interact electromagnetically with the matter in the calorimeter in what is called an EM *shower* (or *cascade*).

2.1.1 Electromagnetic Interactions

When a charged particle passes through matter it loses energy by ionization and excitation of the atoms in the material. The mean rate of energy loss (dE/dx) due to ionization and excitation is given by the Bethe-Bloch equation [2]:

$$-\frac{dE}{dx}\left(\frac{\text{MeV}}{\text{g/cm}^2}\right) = 4\pi N_A r_e^2 m_e c^2 z^2 \frac{Z}{A}\frac{1}{\beta^2}\left[\frac{1}{2}\ln\left(\frac{2m_e c^2\beta^2 T_{\max}}{I^2(1-\beta^2)}\right) - \beta^2 - \frac{\delta}{2}\right], \qquad (2.1)$$

where N_A is Avogadro's number, r_e is the classical electron radius, $m_e c^2$ is the mass, z is the charge of the incident particle, Z and A are the atomic number and atomic mass of the material, β is the particle velocity ($\beta = v/c$), and δ is the density effect

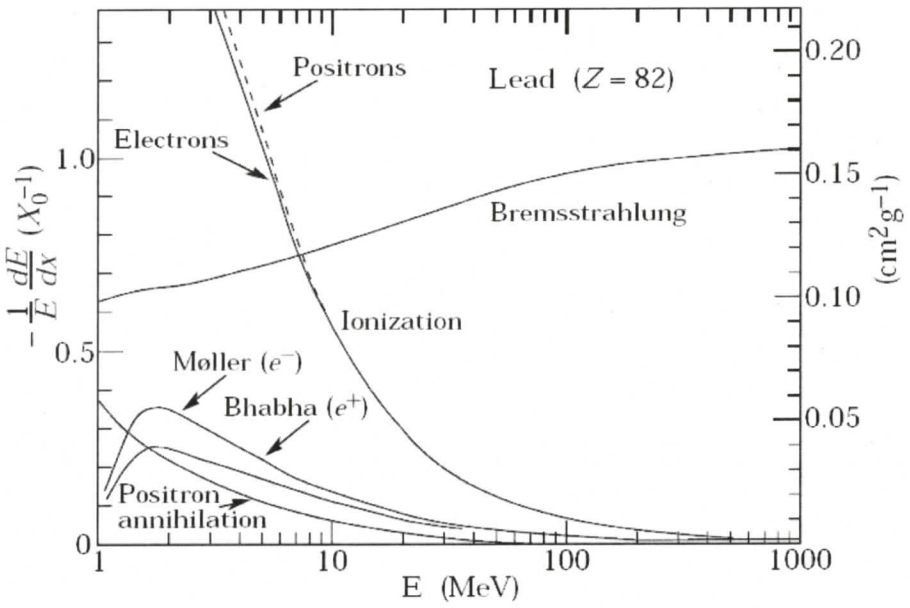

Figure 2.2: Fractional energy loss per unit length in lead as a function of electron or positron energy [2]. This figure shows the different mechanisms by which electrons and positrons lose energy in matter. This figure indicates that there are two dominating processes governing energy deposition: bremsstrahlung losses and ionization losses, with the transition occurring at a critical energy on the order of ~10 MeV.

correction to ionization energy loss. $T_{\max}$ is the maximum kinetic energy that can be given to a free electron in a single collision, and I is the mean excitation energy of the atoms in the material.

Figure 2.2 shows several mechanisms by which electrons and positrons lose energy in lead. The amount that each mechanism contributes to the energy loss is dependent on the energy of the particle. At low energy (below ~10 MeV) electrons and positrons lose energy mainly through ionization of the material[2].

[2]The three other processes shown that minimally contribute below 10 MeV are: positron annihilation with an electron, Møller electron scattering ($e^- + e^- \rightarrow e^- + e^-$), and Bhabha positron scattering ($e^+ + e^- \rightarrow e^+ + e^-$).

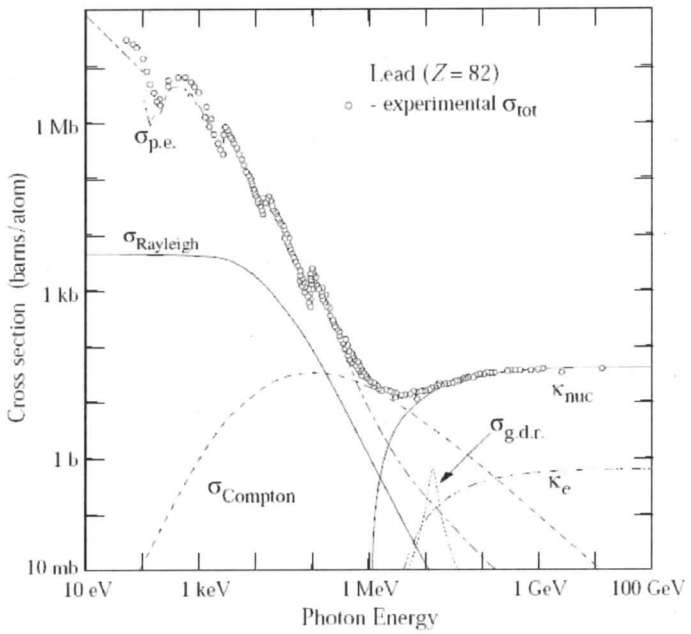

Figure 2.3: Photon cross sections for different energy loss mechanisms in lead as a function of photon energy: photoelectric effect ($\sigma_{\text{p.e.}}$), Rayleigh (σ_{Rayleigh}) and Compton (σ_{Compton}) scattering processes, pair production from nuclear (κ_{nuc}) and electron (κ_{e}) fields, and the giant-dipole-resonance photonuclear interaction ($\sigma_{\text{g.d.r.}}$). Experimentally determined total cross sections at different photon energies are shown as circular data points [2].

There are also several energy dependent processes by which photons deposit energy in matter. Figure 2.3 shows the cross section (likelihood of interacting) for various photon interaction mechanisms as a function of the photon energy, plotted with logarithmic scales. At low energies below 100 keV, the photoelectric effect dominates over Rayleigh scattering[3] as the major source of energy loss. In the photoelectric effect, photons are absorbed by the calorimeter material and an electron is ejected. The ejected electron, also called a δ-ray, proceeds to deposit its energy by the methods

[3]Rayleigh scattering is coherent scattering of a photon off an atom that is neither ionized nor excited.

shown in figure 2.2. Between 100 keV and 10 MeV, the dominant process is Compton scattering where a photon transfers energy and momentum to an electron thereby scattering it. The photon is left with reduced 4-momentum (longer wavelength).

In both the $e^{\pm}$ and γ cases, there is an energy threshold on the order of 10 MeV beyond which the energy is shed by creating secondary particles. For electrons and positrons, it is through the bremsstrahlung (braking radiation) process. The charged particle passing through the detector is decelerated by the electric fields from the atoms (classically described as the Coulomb force) and emits a photon. In the process, the electron or positron may experience a small change in direction, diverting it slightly away from the initial direction. This process contributes to the transverse spread of the electromagnetic shower.

At this threshold energy, when ionization losses equal the bremsstrahlung losses in some material:

$$\left.\frac{dE}{dx}\right|_{\text{ionization}} = \left.\frac{dE}{dx}\right|_{\text{bremsstrahlung}}, \tag{2.2}$$

the particle is said to have critical energy, E_c. Empirical expressions [15] give the critical energy approximately as:

$$E_c \simeq \frac{610 \text{ MeV}}{Z + 1.24}, \text{ (solids, liquids)} \tag{2.3}$$

$$E_c \simeq \frac{710 \text{ MeV}}{Z + 0.92}, \text{ (gases)} \tag{2.4}$$

which relates the critical energy to the atomic number Z of the absorber material. Consider an example where electrons deposit energy in lead ($Z = 82$). Equation 2.3 gives $E_c \simeq 7.33$ MeV which is in agreement with the intersection of the bremsstrahlung and ionization curves in figure 2.2.

For photons traversing the detector material with energies above the 10 MeV threshold, pair production is dominant. A photon may convert into an electron and positron in the presence of a nucleus to balance momentum and energy conservation. The created e^+e^- pair interact with the material as described above.

Thus, electrons, positrons, and photons above the critical energy lose energy through particle creation. Furthermore, if the secondary particles also have energies above the critical energy threshold, they too will produce another generation of particles where each generation has a fraction of the initial energy. The electromagnetic shower is now evident: initial high-energy electrons and positrons impacting the calorimeter material emit bremsstrahlung photons. These photons, along with any incident photons, can be sufficiently energetic to produce pairs of electrons and positrons. These secondary charged particles (with energies above ~10 MeV) emit bremsstrahlung photons, which in turn pair produce. The cycle continues yielding a multiplication of particles with degraded energy after each generation. Eventually, particle energies fall below the critical energy at which point particle multiplication ceases. After particles cross this threshold, ionization of the medium is the dominant energy loss mechanism. Note that the energy of an incident particle deposited in the

calorimeter via EM shower processes is, in principle, detectable, and the EM signal has a linear response to different incident particle energies [15, 16].

2.1.2 Electromagnetic Shower Size

A variable called the *radiation length* (X_0) is introduced to describe the size of the EM shower. The compact formula given in [2] for the radiation length is:

$$X_0 \simeq \frac{(716.4\ \mathrm{g/cm^2})A}{Z(Z+1)\ln(287/\sqrt{Z})} \tag{2.5}$$

where Z and A are the atomic number and atomic weight of the detector material respectively. Furthermore, the radiation length of a mixture of materials or a compound is determined by

$$\frac{1}{X_0} = \sum_j \frac{w_j}{X_j} \tag{2.6}$$

where X_j is the radiation length of the j^{th} component, and w_j is the fraction by weight of the j^{th} component. For an electron emitting bremsstrahlung photons, X_0 represents the average distance x of material traversed to leave the electron with $1/e$ of it's initial energy E_0:

$$E(x) = E_0 e^{-(x/X_0)}. \tag{2.7}$$

Likewise, the intensity of a beam of pair producing photons is reduced to $1/e$ of the initial intensity I_0 after traveling a distance $x = \frac{9}{7}X_0$:

$$I(x) = I_0 e^{-(7/9)(x/X_0)}. \tag{2.8}$$

Using radiation lengths provides a material independent distance scale for describing EM showers. Table 2.1 lists the radiation lengths and other properties of the

Material	**Z**	**Density** (g/cm^3)	X_0 (cm)	R_M (cm)	$\lambda_{\mathbf{int}}$ (cm)	E_c (MeV)
Ar (liquid)	18	1.40	14.0	8.0	83.7	37
Cu	29	8.96	1.43	1.52	15.1	20
W	74	19.3	0.35	0.93	9.6	8.0
Pb	82	11.3	0.56	1.60	17.0	7.4

Table 2.1: End-cap calorimeter material properties.

calorimeter materials.

Using the radiation length X_0 and the critical energy E_c, the physical size of particle showers can be conveniently described. An incident particle (e^+, e^-, γ) will impact the calorimeter and initiate a shower that will penetrate into the calorimeter along its original direction (longitudinal development), as well as spread out radially from the original direction (lateral spread). The extent of longitudinal development that contains 95% of the EM shower energy, expressed in terms of numbers of radiation lengths, $t_{95\%}$, is given in [15] as approximately:

$$t_{95\%} \simeq t_{max} + 0.08Z + 9.6, \tag{2.9}$$

where Z is the atomic number, and where $t_{\max}$ is given by:

$$t_{\max} = \frac{\ln(E_0/E_c)}{\ln 2}. \tag{2.10}$$

E_0 is the initial energy of the incident particle, and E_c is the critical energy (as defined in equations 2.3 and 2.4)[4].

The lateral spread of the shower can also be characterized in terms of radiation lengths and critical energy. The source of the lateral spread is due to the scattering of the electron and positron, as well as the bremsstrahlung photon emission. The Molière radius R_M describes the radial distance away from the incident particle direction:

$$R_M = m_e c^2 \sqrt{4\pi/\alpha}\, \frac{X_0}{E_c} \tag{2.11}$$

where m_e is the electron mass, c is the speed of light, and α is the fine structure constant. Thus, $R_M = 21.2$ MeV $\times X_0/E_c$. On average, a cylinder of radius R_M over the full longitudinal depth will contain 90% of the shower energy, and 95% will be contained within $2R_M$ [15]. The Molière radii of mixtures or compounds can be computed with equation (2.6) by replacing the radiation length X_j by R_j.

There are two general properties of radial shower development to note: first, the size of the lateral spread is essentially independent of the initial incident particle

[4]Equation 2.10 indicates that the shower depth scales logarithmically with incident particle energy. This implies that the size of calorimeters needed to contain the showers only scales logarithmically, making calorimeters practical instruments to use for energy measurement as experiments move to higher and higher energies.

energy, according to equation 2.11. Second, the Molière radius is roughly independent of the absorber material: notice that R_M is proportional to the ratio of the radiation length to the critical energy. According to equation 2.5, the radiation length scales with A/Z^2. However, since $A \propto Z$ to first order, we see that $X_0 \propto 1/Z$. The critical energy (equation 2.4) also has a $1/Z$ dependence. Therefore, the lateral EM shower development as given by the Molière radius involving the ratio of these quantities (equation 2.11) is, to a first approximation, Z independent [15].

2.2 Hadronic Showers

In a general sense, the hadronic shower proceeds similarly to the EM shower. High-energy hadrons incident on the detector will typically interact strongly (as well as electromagnetically) with the nuclei of the atoms in the detector. These interactions lead to the initial particle losing its energy through creation of secondary particles, which in turn interact to create more particles, and a cascade develops. The number of secondaries increases with detector depth, but eventually the absorption of these secondaries balances out the multiplication of particles.

Some of the energy in a hadronic shower is deposited through the electromagnetic shower processes described above. Neutral pions (π^0) created in the hadronic cascade will nearly always decay to two photons before they have the chance to interact with another detector nucleus. Once these energetic photons are created they

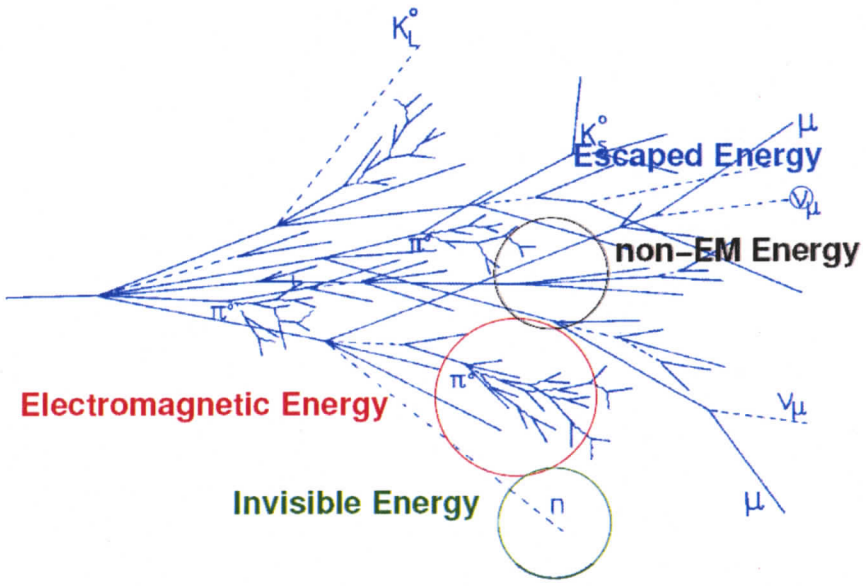

Figure 2.4: Energy classifications within a typical hadronic shower profile [17, 18].

will continue along the EM shower route described in the previous section.

Hadronic showers are more complicated than the EM counterpart, as figure 2.4 illustrates. In addition to the EM component (coming from π^0s), hadronic showers include non-EM energy, invisible energy (mainly from neutron interactions and binding energy losses), and escaping neutrino energy. Therefore, there are substantial differences between the EM and hadronic cases, and these differences have large implications for the performance and understanding of hadronic calorimeters. Hadronic showers are dominated by the strong interactions between the detector atomic nuclei and the incident hadron. The variety and complexity of the mechanisms contributing to hadronic shower spread are greater than the EM case because strong interactions occur between bound composite objects (quarks and gluons confined via the strong

force), and also due to the large number of nucleons in the nuclei of the detector material.

In the remainder of this section, an overview of the hadronic processes responsible for shower production are presented, followed by a general description of hadronic shower size, and the EM energy scale used for hadronic energy reconstruction.

2.2.1 Particle sector

A hadron interacting strongly with a nucleus in the calorimeter material gives rise to effects that can be classified as either being a part of the *particle sector* (high energy region dominated by particle production) or the *nuclear sector* (nuclear interactions with characteristic energies at the MeV scale) of the hadronic shower. The particle sector describes the energetic secondary hadrons that are produced when an initial energetic hadron impacts a nucleus. The secondary particles are often called leading particles because they continue on a trajectory close to that of the incident particle, and they carry a large portion of the incident hadron momentum (typically $\sim 1/2$). The dominant secondaries produced are pions where 2/3 of the pions are charged (π^+ and π^-), and 1/3 are neutral (π^0) [16]. The π^0s decay electromagnetically before they have a chance to collide with another nucleus. Thus, all hadronic showers have a central component of EM energy.

If the secondary particles are sufficiently energetic, they also will interact to produce additional π^0s that decay and deposit their energy electromagnetically. Thus,

higher energy incident particles will produce hadronic showers with a greater EM fraction. An empirical expression for the electromagnetic fraction of the hadronic shower is:

$$f_{\mathrm{EM}} = 1 - \left(\frac{E}{E_s}\right)^{k-1} \tag{2.12}$$

where E is the energy of the initial particle, E_s is a scale factor corresponding to the average energy needed for the production of one pion (E_s = 0.7 GeV and 1.3 GeV for copper and lead, respectively). The factor k is related to the average multiplicity of meson production and the fraction of π^0s created in the reactions, and has an approximate value of $k \sim 0.8$ [16]. The exponent on the energy term in equation 2.12 indicates that the electromagnetic fraction of a hadronic shower has a non-linear dependence on the energy of the initial particle. As the incident particle energy increases so does the EM fraction of the ensuing shower via π^0 production. Therefore, at higher energies the response of calorimeters to hadronic showers increases because there is a larger fraction of energy being deposited via electromagnetic processes.

In addition to the neutral pions, the particle sector includes charged pions ($\pi^{\pm}$) and baryons. These particles are produced in nuclear interactions and deposit energy through ionization. The secondary charged particles will go on to interact with a nucleus giving rise to the next generation in the shower.

Finally, the particle sector includes energetic neutral baryons, dominated by the neutron. Due to the lack of charge and the long lifetime of the neutron, the only

way for these leading neutrons to deposit energy is through nuclear collisions. The energy of the neutrons is eventually reduced to the MeV scale through these elastic collisions. At this energy scale, these low-energy ("soft") neutrons have passed into the nuclear sector where there are different mechanisms by which neutrons interact with the detector.

2.2.2 Nuclear Sector

While some of the initial particle energy is carried by the secondary particles created in a nuclear interaction, the remaining energy goes into nuclear processes such as spallation, excitation, and nucleon evaporation [15]. Spallation is described as a two stage process: the first stage is called the intra-nuclear cascade where a hadron collides with the nucleons, which in turn collide with other nucleons within the nucleus, distributing the kinetic energy. Some protons and neutrons may gain enough energy to escape as energetic particles. Also, if the energy transfer is high enough, new hadrons (mostly pions) may be emitted. The second stage in spallation is where the intermediate excited nucleus sheds it's extra energy. This is achieved by "evaporating" or ejecting nucleons (typically neutrons, but also protons and even α-particles). Evaporated neutrons carry away the extra energy in the excited nucleus. The nucleus will continue to eject these particles isotropically until the excess energy is below the binding energy of a nucleon. The remaining energy at this point (on the order of 1 MeV) is emitted via nuclear γ-rays. These nuclear photons are emitted with a sub-

stantial delay which means that the majority may not be detected and are effectively a source of calorimeter energy loss [15].

Up until now, energy deposited into the detector yielding a measurable signal has been detected through ionization in the active component of the calorimeters. Even the neutral pions follow this approach due to their decay into photon pairs. The low energy evaporation neutrons do not interact electromagnetically, and the weak decay lifetime is too long for consideration in calorimeters. The strong interactions are the only way for neutrons to deposit kinetic energy and eventually be absorbed by the detector. The evaporation neutrons emitted from the excited nucleus have a kinetic energy spectrum generally described by a Boltzmann-Maxwell distribution

$$\frac{dN}{dE} \propto \sqrt{E} e^{-E/T} \tag{2.13}$$

with a temperature of $T \sim 2$ MeV. When nucleons emerge from the nucleus, some of the initial particle energy is consumed in overcoming the nuclear binding energy. The average kinetic energy of the soft neutrons is on the MeV scale, which is 1/2 to 1/3 of the nuclear binding energy that had held it in the nucleus. This binding energy is *invisible* to the calorimeter and is an important source of lost energy in hadronic showers. Invisible energy present within hadronic showers (but not EM showers) is one reason that the calorimeter response to hadronic energy may be reduced compared to the same initial EM energy. Furthermore, the amount of invisible energy in

any given event can vary greatly due to the wide range of possible hadronic interactions. It is possible to build *compensating* calorimeters that have the same response to electromagnetic and hadronic processes. Due to experimental conditions at the LHC, ATLAS calorimeters are constructed in such a way as to be non-compensating. However, some level of offline software compensation is performed in ATLAS.

The eventual fate of neutrons also affects hadronic calorimeter response. Neutrons will lose energy mainly through elastic and inelastic collisions with nuclei. An inelastic interaction excites the nucleus which then emits a photon to shed that energy. After nearly all kinetic energy has been lost, a neutron will be captured by a nucleus thereby transforming the nucleus into a different isotope. In the process, the binding energy that originally had to be spent in freeing that neutron is released to the system in the form of a photon with a large time delay. This photon may not be detected and so the binding energy may remain invisible to the calorimeter.

2.2.3 Hadronic Shower Size

On average, the hadronic shower extends further along the direction of the incident particle and spreads out wider in the lateral direction as compared to the profiles of the electromagnetic shower. The shower development is dominated by nuclear interactions, and so the size of the resulting shower depends on the nuclear interaction length λ_{int}. It is the average distance a high energy hadron travels in a medium before a nuclear interaction occurs. The nuclear interaction length for specific materials is

computed approximately as:

$$\lambda_{\text{int}} \approx 35A^{1/3}(\text{g/cm}^2) \tag{2.14}$$

where A is the atomic weight of the absorber material [19]. Table 2.1 in the previous section lists the interaction lengths of the end-cap calorimeter materials. The nuclear interaction length for a compound substance or mixture is determined in the same way as for the radiation length (see equation 2.6). λ_{int} has the same units as the radiation length X_0, and is also an approximately material independent distance scale.

Recall that a fraction of the hadronic energy is deposited via EM interactions, which have smaller spread and penetration. Thus, the expected lateral profile has a prominent central core surrounding the incident particle direction, due to the EM component, and a more extended hadronic halo. Furthermore, as this same profile is taken at increasing depths into the detector volume, the prominence of the central core diminishes.

2.2.4 EM Energy Scale

In EM showers, the signal produced in the calorimeter (in the form of ionization current in ATLAS) is linearly proportional to the energy of the incident particle (electron). The relationship between the current measured in the calorimeter from the EM shower and the energy of the incident electron is called the electromagnetic

(EM) energy scale. The EM energy scale is the benchmark with which reconstructed calorimeter energy is expressed.

ATLAS calorimeters are non-compensating, and the signal measured by the calorimeter is lower for an incident hadron than it is for an incident electron of the same energy. Hence, hadronic calorimeters are exposed to electrons and an EM energy scale is established. The EM energy scale is used in this thesis to calculate energy in the hadronic calorimeters. In order to estimate the energy of an incident hadron from the observed signal, several methods of hadronic energy scale calibration are being considered in ATLAS (for example, see reference [13]).

2.3 ATLAS End-Cap Calorimeters

The previous two sections have provided an overview of how energetic particles will lose energy in matter. Attention is now given to the ATLAS end-cap calorimeters, and how they measure particle energy.

Three calorimeters make up the ATLAS end-cap calorimeter: the electromagnetic end-cap calorimeter (EMEC), the hadronic end-cap calorimeter (HEC), and the forward calorimeter (FCAL). Figure 2.5 shows the positioning of the three calorimeters inside the aluminum end-cap cryostat. The pseudorapidity range[5] of the calorimeters is $1.375 < |\eta| < 4.9$. The general characteristics of the end-cap calorimeters are

[5]Using equation 1.2 this corresponds to a polar angle range of $0.9 < \theta < 29.0$ degrees measured from the z-axis (beam pipe).

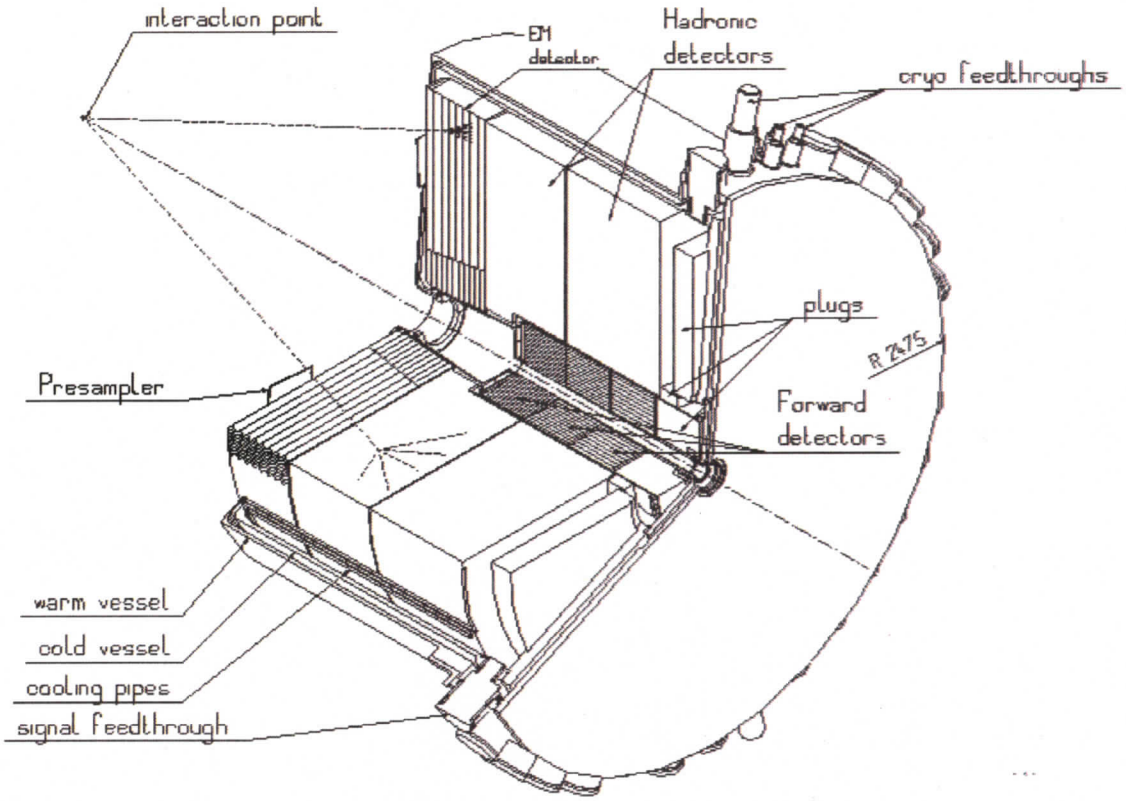

Figure 2.5: Schematic of the end-cap cryostat containing the EMEC, HEC, and FCAL detectors [14]. This view shows the back of the cryostat, and looks inward toward the ATLAS interaction point. The end-cap is filled with liquid argon through the cryo-feedthroughs, and the calorimeter signals are brought out of the cryostat through the signal feedthroughs.

presented in this section, with emphasis on the structure at the LAr gap level.

2.3.1 EMEC

The electromagnetic end-cap calorimeter is a sampling calorimeter with liquid argon as the active material between layers of lead absorbers. The EMEC utilizes a unique geometry for the lead absorber plates, which can be seen in figure 2.6. The EMEC

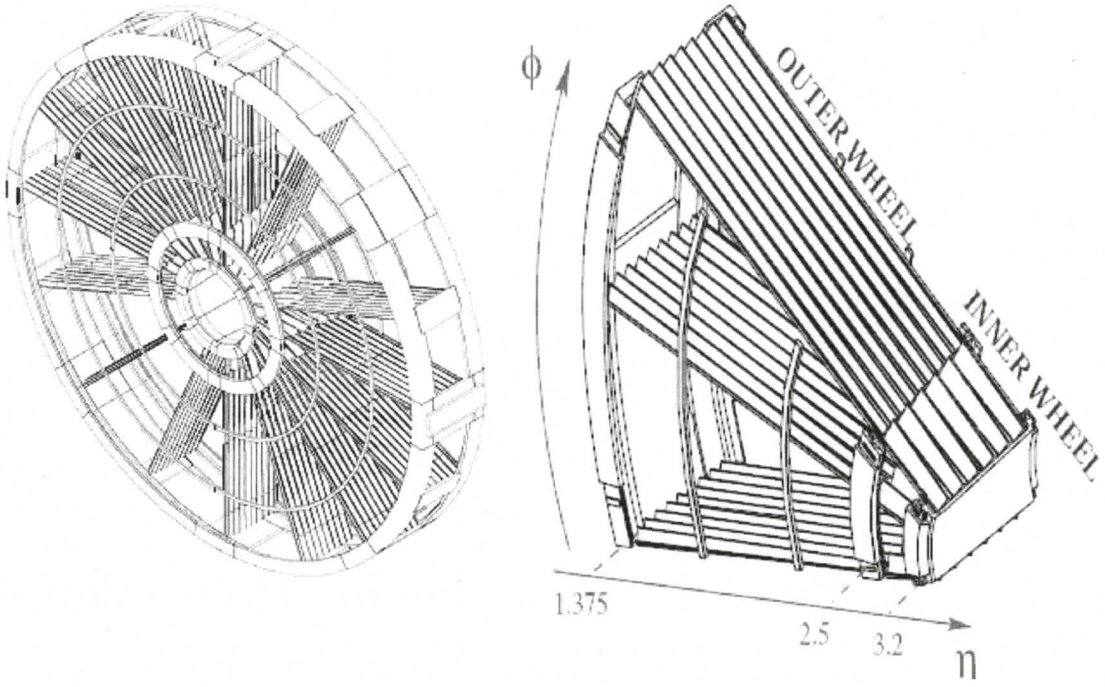

Figure 2.6: Schematic of the inner and outer wheels of the front face of the full EMEC (left) and a single module (right) which is 1/8 of the full wheel [20]. Only a few absorber layers are illustrated. Due to the unique folding of the absorber layers, the ATLAS EM calorimeters are often described as having an "accordion" geometry.

wheel consists of two concentric wheels of radially arranged absorber plates. The plates are folded into "waves" resulting in an "accordion" geometry. Filling the gap between absorber plates is liquid argon, and centered in the LAr gap are electrodes. In this geometry, the ends of the electrodes are brought out of the calorimeter at the front and rear faces of the wheels. Therefore, although the EMEC is structurally separated into eight ϕ modules, the accordion geometry allows for full ϕ hermetic coverage in the end-cap with no cracks between the modules.

Figure 2.6 also illustrates that the folds of the absorbers vary with wheel radius.

Because the LAr gaps naturally increase with radius, and because the absorbers have a constant thickness, the folding angle and wave height must be varied with radius. This keeps the lead-to-LAr ratio approximately constant everywhere in order to maintain a nearly uniform detector response.

The full EMEC wheel has an outer radius of 2077 mm and is 632 mm thick (at room temperature). The thickness in terms of radiation lengths is a function of pseudorapidity and varies from about 26 X_0 to 36 X_0. Two concentric wheels, the inner wheel and the outer wheel, are needed to span the full EMEC dimension[6]. The inner wheel consists of 256 lead plates (with a constant thickness of 2.2 mm) and 256 electrodes. The outer wheel has 768 lead plates (with a constant thickness of 1.7 mm) and 756 electrodes. The inner wheel uses absorbers and electrodes with six waves, whereas the outer wheel uses nine waves. The two wheels are separated by a 3 mm crack at $|\eta| = 2.5$. The lead absorbers have a 0.2 mm skin of stainless steel glued[7] to either side to provide mechanical strength [14].

A particle traversing the EMEC will cross multiple folds of several accordion absorbers and electrodes, and ionizes the liquid argon along its trajectory. A detectable signal proportional to the ionization is produced from the motion of the ionization electrons in the LAr gap between the absorbers. In this way, the deposited ionization energy is sampled in each LAr gap. A schematic of the EMEC inner wheel

[6]Technical limitations on the degree to which lead absorber sheets can be folded prevent one single EMEC wheel from covering the full η range [14].

[7]A 0.13 mm thick fiberglass cloth pre-impregnated with epoxy resin is used to glue the steel skin to the lead absorbers.

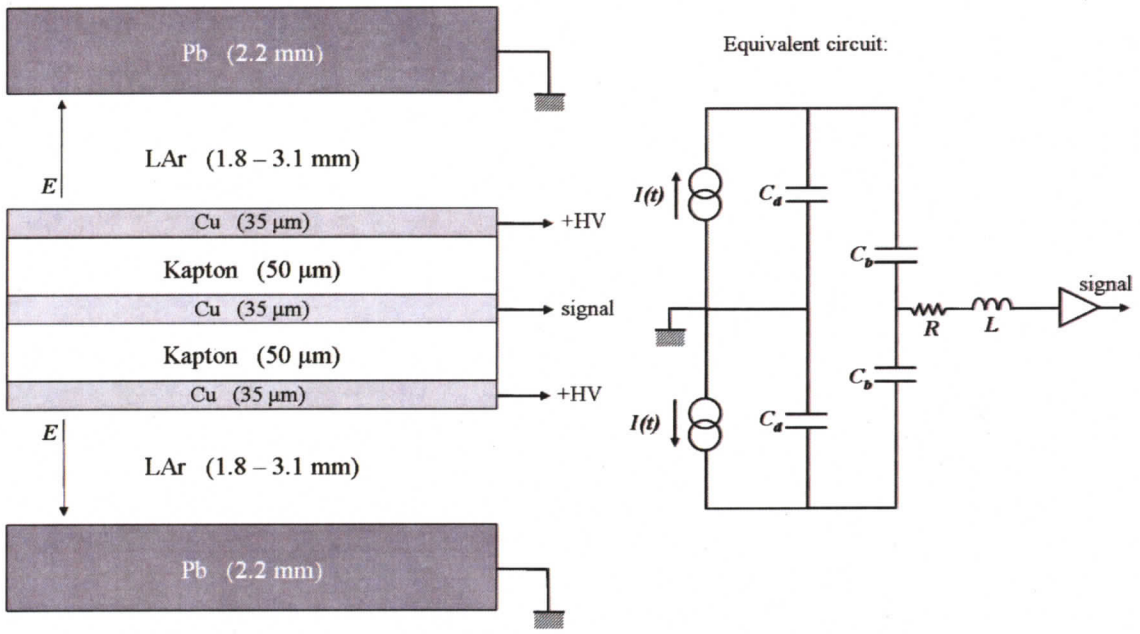

Figure 2.7: Illustration (left) of the EMEC inner wheel electrode structure between two lead absorber plates (not to scale); and the equivalent circuit (right) where $I(t)$ describes the motion of the ionization electrons in the LAr gap, C_d is the capacitance between the lead (Pb) absorber and the HV-carrying copper (Cu) electrode, C_b is the capacitive coupling between the HV-carrying Cu electrode and the signal readout line, and R and L describe the resistance and inductance of the readout line.

electrode structure is given in figure 2.7 where the readout electrode separates in half the LAr gap between two absorber plates. Honeycomb spacers are used to keep the electrode centered between the absorbers. The LAr gaps in the inner wheel vary between 1.8 mm at low radius to 3.1 mm at outer edge of the inner wheel. The outer wheel LAr gaps vary from 0.9 mm to 2.8 mm at the full EMEC radius [21]. The high voltage across the LAr gaps is varied with radius in order to keep the drift velocity of electrons approximately constant. See section 5.6 for further discussion on EMEC

high voltage issues.

The electrodes are flexible printed circuit boards made from copper coated Kapton[8] polyimide sheets, and are also bent into the same accordion shape as the lead absorbers. The outer two copper layers carry the positive high voltage (HV) that produce the electric field across the LAr gaps. The motion of the ionization electrons in the LAr gaps induces signals on the outer copper layers which are readout by capacitive coupling to the inner copper layer [21]. Not shown in this figure are the four thin thermosetting epoxy layers used to glue the copper and Kapton insulators together (adding 70 μm to the electrode thickness [22]), nor the steel skin and epoxy used to encase the lead (as mentioned above).

The EMEC electrodes are segmented into cells that are fully pointing in η and in ϕ, meaning they are oriented toward the ATLAS interaction point in the center of the detector. The EMEC inner wheel cell granularity ($\Delta\eta \times \Delta\phi$) is ($0.1 \times 0.1$). The cells are also segmented in z (distance from ATLAS center) giving different longitudinal layers, or *samplings*. A cross-section of the EMEC and HEC is given in figure 2.8 that shows the η segmentation and z samplings. The end-cap calorimeters are symmetric in ϕ. The region of interest for the 2004 testbeam is the high pseudorapidity region below the dashed cyan line with $|\eta| > 2.5$.

[8]Kapton is a trade mark of Dupont Corporation.

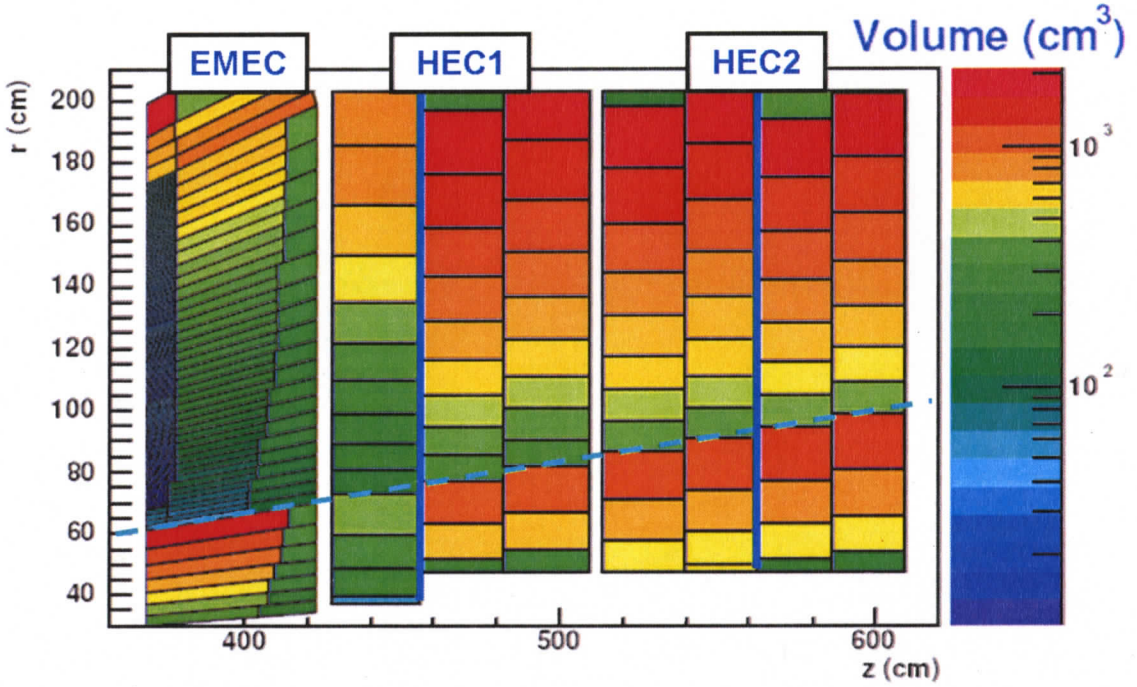

Figure 2.8: EMEC and HEC cell volumes and segmentation [18]. The colours indicate the volume of each cell, with the HEC cells being 10 times the value indicated. The EMEC is fully pointing in η whereas the HEC has a pseudo-pointing cell structure in η. The z coordinate measures the distance from the ATLAS interaction point. The z samplings in the EMEC are clearly visible. Each HEC wheel is segmented into two z samplings, indicated by the vertical blue lines. The dashed line is at $|\eta| = 2.5$.

2.3.2 HEC

In contrast to the EMEC's unique accordion geometry, the hadronic end-cap sampling calorimeter has a more traditional design with alternating parallel plate absorbers and electrodes oriented perpendicular to the beam direction. The HEC consists of two wheels structurally segmented into 32 ϕ modules each, with a 2 mm crack between the modules. The HEC cell granularity ($\Delta\eta \times \Delta\phi$) is equal to ($0.1 \times 0.1$) for $1.5 < |\eta| < 2.5$, and (0.2×0.2) for $2.5 < |\eta| < 3.2$. Figure 2.9 illustrates the alternating

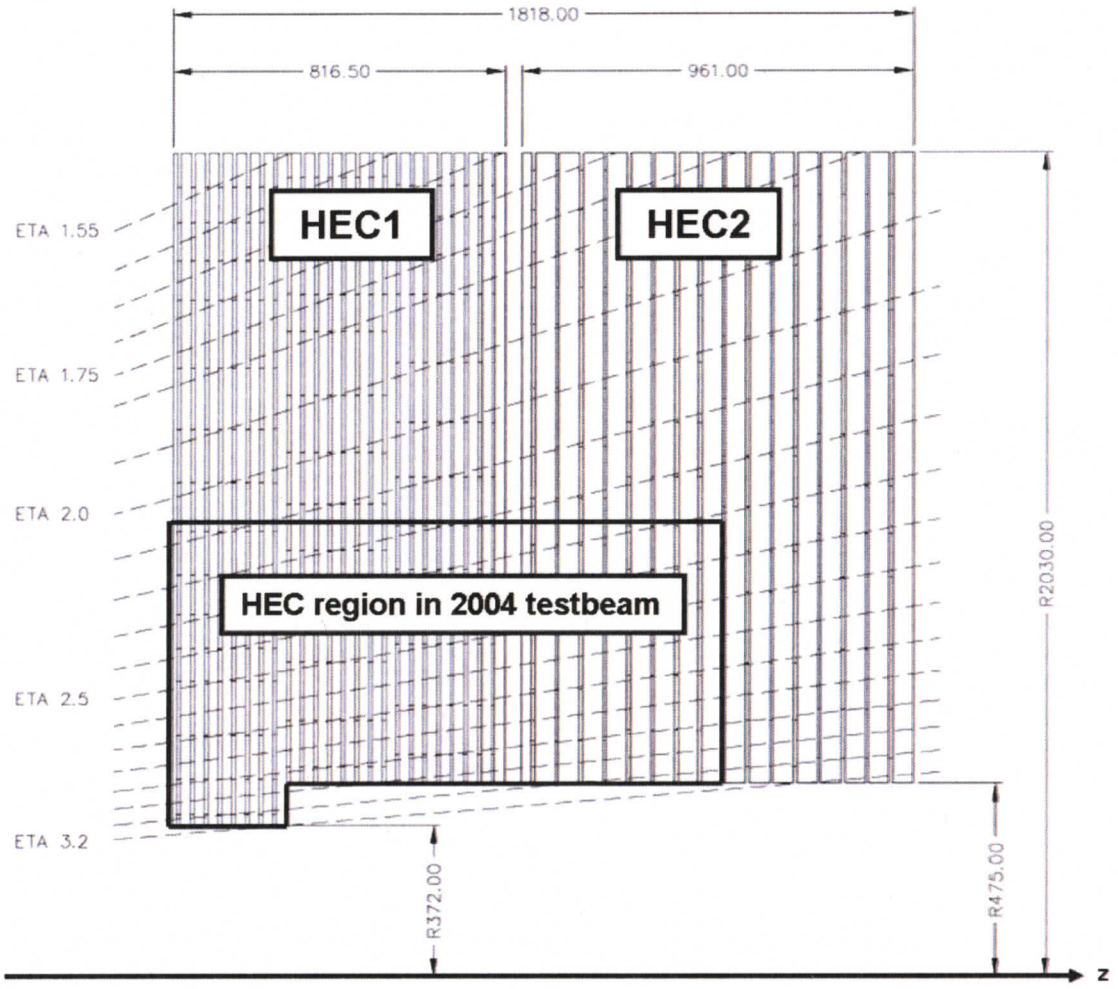

Figure 2.9: Schematic of the HEC illustrating the dimensions (in mm) of the two HEC wheels [14]. Lines of constant pseudorapidity are shown. The HEC region being used in the 2004 combined beam test is also indicated (see section 3.2 of this thesis for further details).

absorber layers and LAr gaps, and the dimensions of the two HEC wheels (HEC1 and HEC2) are given. HEC1 is located behind the EMEC and uses 25 mm thick copper absorber plates, and has a total LAr gap of 8.5 mm between the plates. The second HEC wheel (HEC2) also has LAr gaps of 8.5 mm, but uses 50 mm copper plates. HEC1 has two longitudinal samplings, separating the first 8 absorber-LAr layer pairs from the remaining 16 absorber-LAr layer pairs. HEC2 also has two layers, each consisting of 8 absorber-LAr layer pairs. The interaction lengths of the four HEC samplings are (from right to left): $1.41\lambda_{\text{int}}$, $2.82\lambda_{\text{int}}$, $2.74\lambda_{\text{int}}$, and $2.74\lambda_{\text{int}}$ [13].

The HEC electrode structure, shown in figure 2.10, is more complicated than in the EMEC. In each 8.5 mm LAr gap there are three parallel electrode boards and four honeycomb spacers, creating four equal drift volumes of $\sim$1.8 mm each. The central circuit board is the same as the EMEC: two outer copper layers connected to positive HV, separated (by Kapton) from the central copper readout electrode. The outer two boards are a Cu-Kapton-Cu sandwich, and are high voltage carriers. Without the outer two boards, the LAr gap would need two times more HV to produce the required electric field in the resulting gap [14].

2.3.3 FCAL

The third detector in the ATLAS end-cap is the Forward Calorimeter (FCAL). The FCAL surrounds the beam pipe and provides electromagnetic and hadronic calorimeter coverage in the pseudorapidity region between $3.1 < |\eta| < 4.9$. The FCAL consists

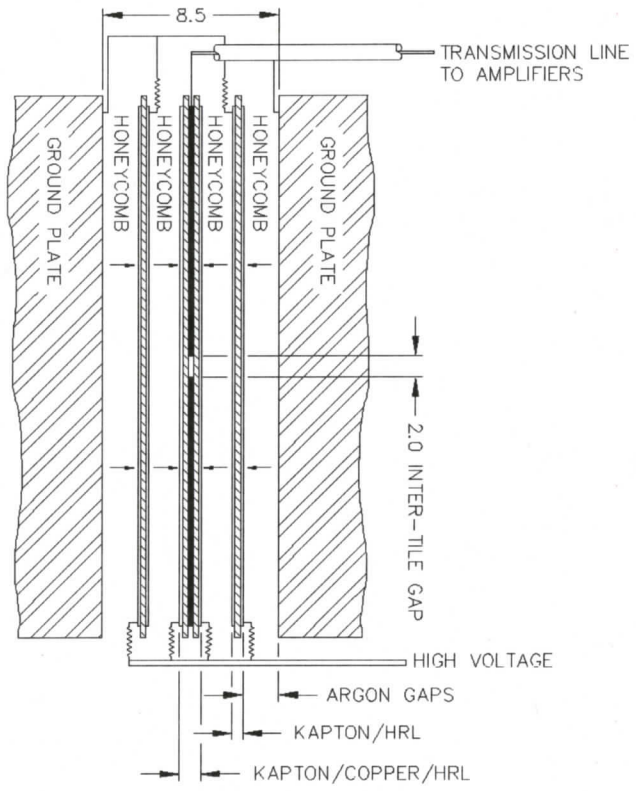

Figure 2.10: HEC electrode structure between two copper absorber plates [14].

of three cylindrical modules (which define the z samplings) with an outer radius of 455 mm and a longitudinal depth of 450 mm each (see figure 2.5). The FCAL is recessed 964 mm from the front of the EMEC [14].

Figure 2.11 shows a cross-section through the beam pipe and the FCAL. Each FCAL module consists of an absorber matrix with longitudinal tubes filled with a solid absorber rod. A cylindrical liquid argon gap of constant thickness is maintained by winding a polyimide-coated quartz fibre around the rod[9]. The electric field across

[9]The fibre has a diameter of 240 μm, and is wound around the rod in a helix with four turns per rod length [14].

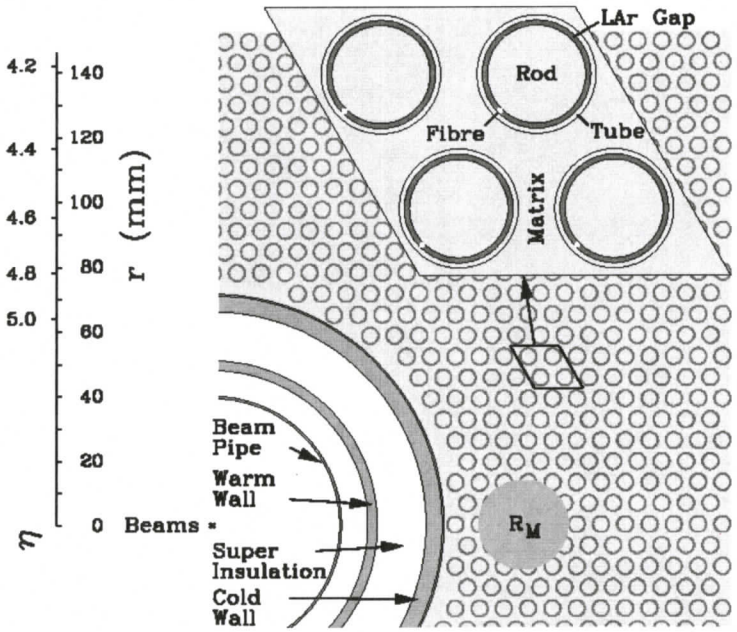

Figure 2.11: Diagram of the FCAL liquid argon gap structure [14]. The Molière radius is shown, along with the beam pipe and cryostat structure.

the LAr gap is produced by keeping the absorber rods at positive high voltage and the matrix grounded. The signal is readout directly from signal pins inserted in the ends of each rod.

The first FCAL layer, FCAL1, is the forward EM calorimeter which uses copper as the matrix/rod absorber material. The rod diameter is 4.75 mm and the LAr gap thickness is 0.250 mm. The FCAL1 module cell granularity ($\Delta\eta \times \Delta\phi$) is approximately ($0.1 \times 0.1$) formed by four channels (figure 2.11).

The remaining two layers, FCAL2 and FCAL3, constitute the forward hadronic calorimeter. Tungsten is used as the absorber material for both the matrix and the

rods, but the tube containing the LAr and rod is copper. Tungsten is used because it is dense and very radiation-hard [14]. FCAL2 has 4.75 mm thick rods and a LAr gap thickness of 0.375 mm. FCAL3 has 5.50 mm thick rods and 0.50 mm LAr gaps. The $(\Delta\eta \times \Delta\phi)$ granularity in the FCAL2 and FCAL3 is approximately (0.2×0.2) [23].

To summarize, this chapter has provided a general description of how energetic particles interact with matter in the context of ATLAS calorimetry. When collision products emerge from the ATLAS interaction point and impact the liquid argon detectors, electromagnetic showers and hadronic showers are created. The energy of all the shower particles is sampled by reading out the ionization current in the LAr gaps of the detectors. The initial energy of an incident particle can be reconstructed from the samples of the shower energy.

This chapter has also presented an overview of the properties of the ATLAS end-cap calorimeters. With this understanding of the design of the ATLAS calorimeters, and how particles will interact with them, attention can now be given to testing these detectors with beams of energetic particles.

Chapter 3

Experimental Setup for Particle Beam Tests

Different components of the ATLAS LAr end-cap calorimeters have been tested using particle beams between 1996 and 2003 [8, 9, 10]. These tests allow the detectors to be calibrated, performance to be evaluated, and problems to be identified and corrected.

This thesis focuses on the high pseudorapidity region ($|\eta| > 2.5$) of the ATLAS end-cap calorimeters which underwent beam testing during two periods in the summer and autumn of 2004. The first running period was from May 17 to July 7, and period 2 was from August 16 to October 11. During these periods, sections of the EMEC, HEC, and FCAL modules were tested with particle beams produced by CERN's Super Proton Synchrotron (SPS) and directed down the H6 beam line in the North Area at CERN [24]. This is the first time that the three different LAr calorimeters (EMEC, HEC, and FCAL) have been tested together.

The 2004 combined beam test of the end-cap calorimeters (CBT-EC2, or *testbeam* for short) enables the study of particle showers in the complicated "crack" region where all three of the LAr detectors meet geometrically. Understanding calorimeter performance, dead-material effects, and reconstruction methods in this interface region will be important in preparation for the ATLAS experiment. This chapter describes the general experimental setup of the 2004 testbeam.

3.1 Beam Detectors

Beams of electrons, positrons, charged pions, and muons, with energies ranging from 6 GeV to 200 GeV, are used to illuminate the calorimeter modules in the 2004 testbeam experiment [24]. During testbeam data acquisition, a *run* is defined as a collection of recorded interactions (*events*) from sequential incident beam particles with the same impact point on the calorimeter and the same beam energy. A typical run has approximately 20 000 events and lasts for approximately 25 minutes. In the first running period approximately 4.5 million events were taken. Approximately 19 million events were recorded in period 2.

A schematic of the setup of the testbeam experiment is shown in figure 3.1. The particle beams emerge into air from the vacuum of the H6 beam pipe, and travel from right to left in this figure. The end of the beam pipe is located approximately 31.4 m upstream of the cryostat housing the calorimeters. Positioned at the end of

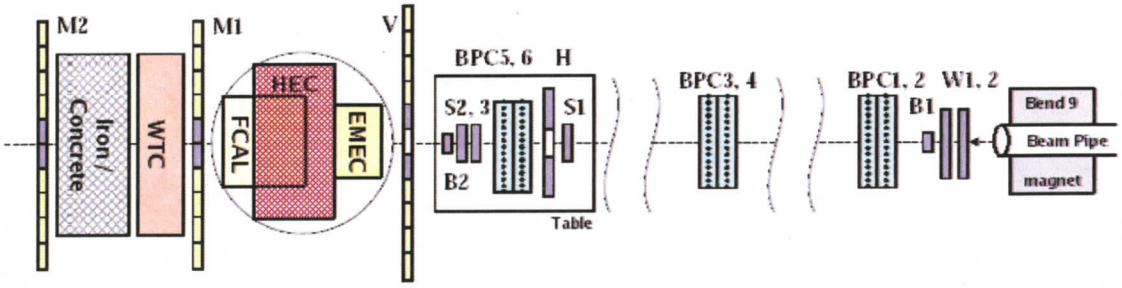

Figure 3.1: Layout of the testbeam setup as viewed from above. Beams of particles emerge from the end of the H6 beam pipe on the right and travel toward the left. The particles pass through various beam monitoring detectors before impacting the LAr calorimeter modules (EMEC, HEC, and FCAL) in the H6 cryostat. Any particles that emerge out the back of the calorimeters are detected with additional detectors: M1, M2, and the warm tail-catcher (WTC).

the beam pipe is the Bend 9 magnet which is used to deflect the beam vertically. A table holding several beam detectors also moves vertically (with 1 mm precision) to ensure that the deflected beam passes through the detectors. The limits on the vertical movement of the detector table are +245 mm to −187 mm with respect to the nominal beam position.

After exiting the beam pipe, the particle beams pass through six "beam" proportional chambers (BPC1-BPC6) [25] used to measure the particle beam position. From the position measurements, the incident particle trajectory can be derived offline. BPCs 1, 2, 5, and 6 have 1 mm wire spacing in the horizontal and vertical planes; BPCs 3 and 4 have 2 mm wire spacing.

Several scintillation counters (S1-S3, B1-B2, W1, and W2) are also placed in the beam line and can be used to detect beam particles, and to make a *trigger*

Beam Detector	ℓ_x **(cm)**	ℓ_y **(cm)**
S1	10	10
S2	10	10
S3	7	7
B1	3	3
B2	3	3
W1	15	15
W2	15	15

Table 3.1: Dimensions of several beam line scintillation counters.

(electronic event definition). They are aligned to select those beam particles that will hit the desired impact point. The area of each detector, as seen by the beam particles, is given in table 3.1. The observation of simultaneous signals in scintillation counters S1, S2, and S3 defines the event trigger. Using three counters in the beam path minimizes triggering on beam particles not on the desired trajectory, and also reduces false events due to noise in the scintillators. When a beam particle initiates an event trigger, the response of the calorimeter to the incident particle is recorded as an event in that run.

Other scintillation counters located along the beam direction (H, V, M1, and M2) are used offline to exclude undesirable particles from being included in the dataset. The Hole (H) and Veto (V) counters surround the beam line and are used to exclude beam halo particles which are outside the acceptable beam size. Counter H is a 35 cm×30 cm piece of scintillator with a circular hole (diameter = 6.5 cm) in it to allow the beam to pass through, whereas V includes four rectangular scintillators placed above, below, and to either side of the beam.

Behind the cryostat, the Warm Tail-Catcher[1] (WTC) and an iron/concrete beam stop are placed in between two muon detectors (labeled M1 and M2). Detectors M1 and M2 are hodoscopes, or walls, of scintillators. Each wall consists of an array of ten 20 cm×200 cm scintillators, overlapping by 1 cm. A coincidence signal from counters M1 and M2 indicates that a muon has passed through the experiment. See section 4.1 for details on the use of these detectors for event selection.

3.2 Calorimeter Module Setup

After the particle beams emerge from the end of the beam pipe and pass through the detectors in the beam, they impact the ATLAS end-cap calorimeters inside the H6 cryostat (see figure 3.1). Because the 2004 testbeam experiment is focusing on the high pseudorapidity region of the ATLAS end-cap calorimeters, modules of the EMEC, HEC, and FCAL calorimeters from the high η region of ATLAS are used in the experiment. The modules are nearly identical in design and function to the full ATLAS end-cap calorimeters (as discussed in section 2.3).

The cryostat available for use in the 2004 end-cap beam test is a stainless steel vertical cylinder with an inner radius of 2.5 m. Particle beams enter the side of the cryostat through a 60 cm diameter circular window of thickness 5.5 mm. The cryostat is filled with liquid argon to a height of 2.2 m, completely submerging the

[1]The WTC consists of walls of scintillation counter arrays placed in between slabs of 10 cm thick steel. The WTC data is not used in this analysis.

EMEC, HEC, and FCAL modules inside. The dimensions of the cryostat constrain the allowable size of the calorimeter modules in the testbeam experiment.

Figures 3.2 and 3.3 show two images of the 2004 testbeam calorimeter modules prior to the beginning of experiment. In figure 3.2 the testbeam calorimeter modules and support structure are being lowered into the cryostat, and figure 3.3 shows the modules inside the cryostat. A schematic diagram illustrating the side view of the modules in the cryostat is given in figure 3.4. The EMEC inner wheel (IW) module sits in front of the HEC, and below is the FCAL. Before the specifics of the calorimeter modules are given, some general observations are made: first, the detector modules are positioned such that the center of the EMEC is aligned with the center of the cryostat window. This occurs at $|\eta| = 2.8$, or in terms of testbeam coordinates[2], at $y = 0$ mm. Also note that the calorimeter modules are oriented at an angle with respect to the vertical. This reproduces the orientation of the end-cap calorimeters in ATLAS with respect to particles emanating from the interaction point with $|\eta| = 2.8$, thereby preserving the pointing nature of the readout cell segmentation[3]. For other values of η, the geometry is slightly off pointing because the bending magnet must deflect the beam slightly away from horizontal in order to probe different pseudorapidity values.

[2]A right-handed Cartesian coordinate system is defined for testbeam data analysis. The origin of the coordinate system is the center of the circular cryostat window. Using figure 3.4 as a reference, the x-axis points into the page, and the y-axis points upward. The z-axis increases to the right, implying that beam particles incident on the cryostat travel in the negative z direction.

[3]The response of the testbeam calorimeter modules to an incident beam particle at $|\eta| = 2.8$ models what will occur in ATLAS for collision products leaving the ATLAS interaction point and impacting the end-cap at the same pseudorapidity. See figures 1.3 and 2.8.

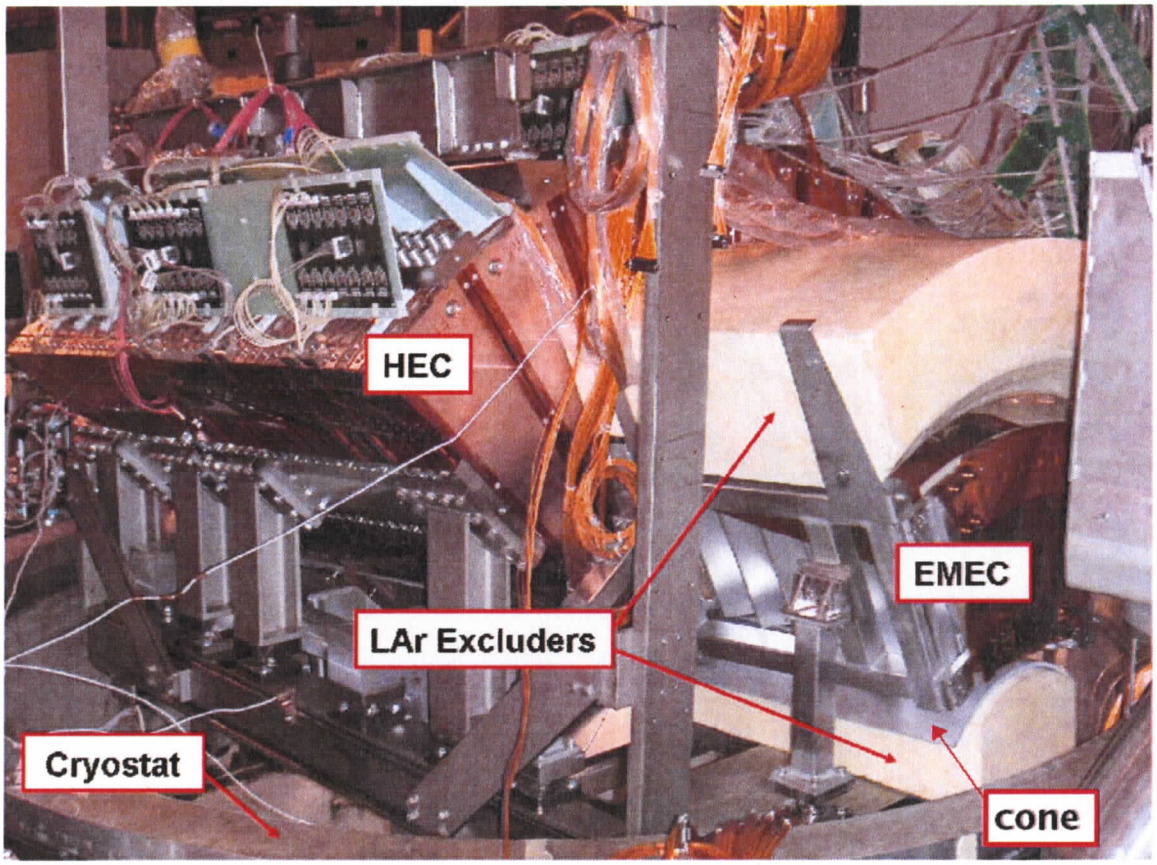

Figure 3.2: The end-cap calorimeter modules before being lowered into the cryostat. The EMEC module sits in front of the HEC, and the FCAL module (hidden in this view) is underneath the HEC. The particle beams come from the right. Above and below the EMEC are the LAr *excluders*: pieces of hard foam that prevent the liquid argon from filling the regions that are void of liquid argon in the ATLAS setup. The cone simulates the dead material introduced by the cryostat in ATLAS.

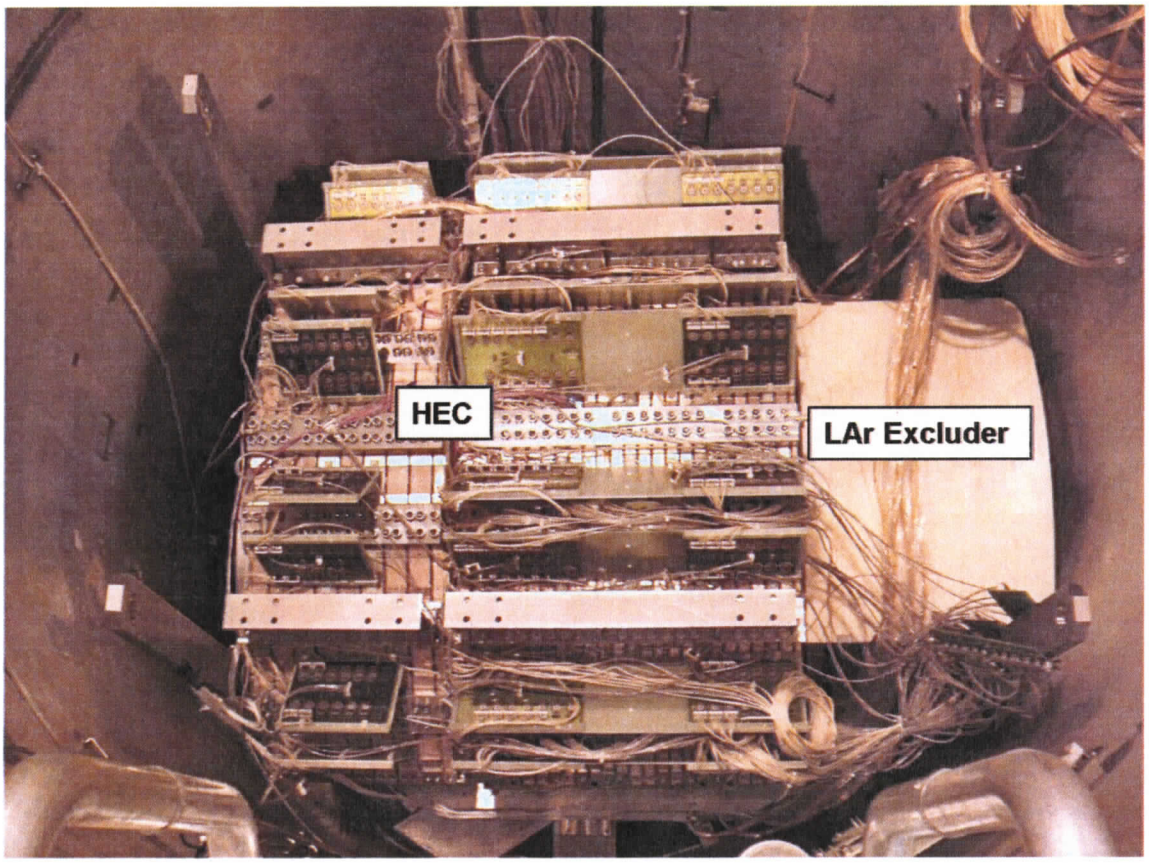

Figure 3.3: View of the calorimeter modules looking down into the cryostat. When the cryostat is closed and filled with liquid argon, the calorimeters are completely submerged. Particle beams enter from the right side.

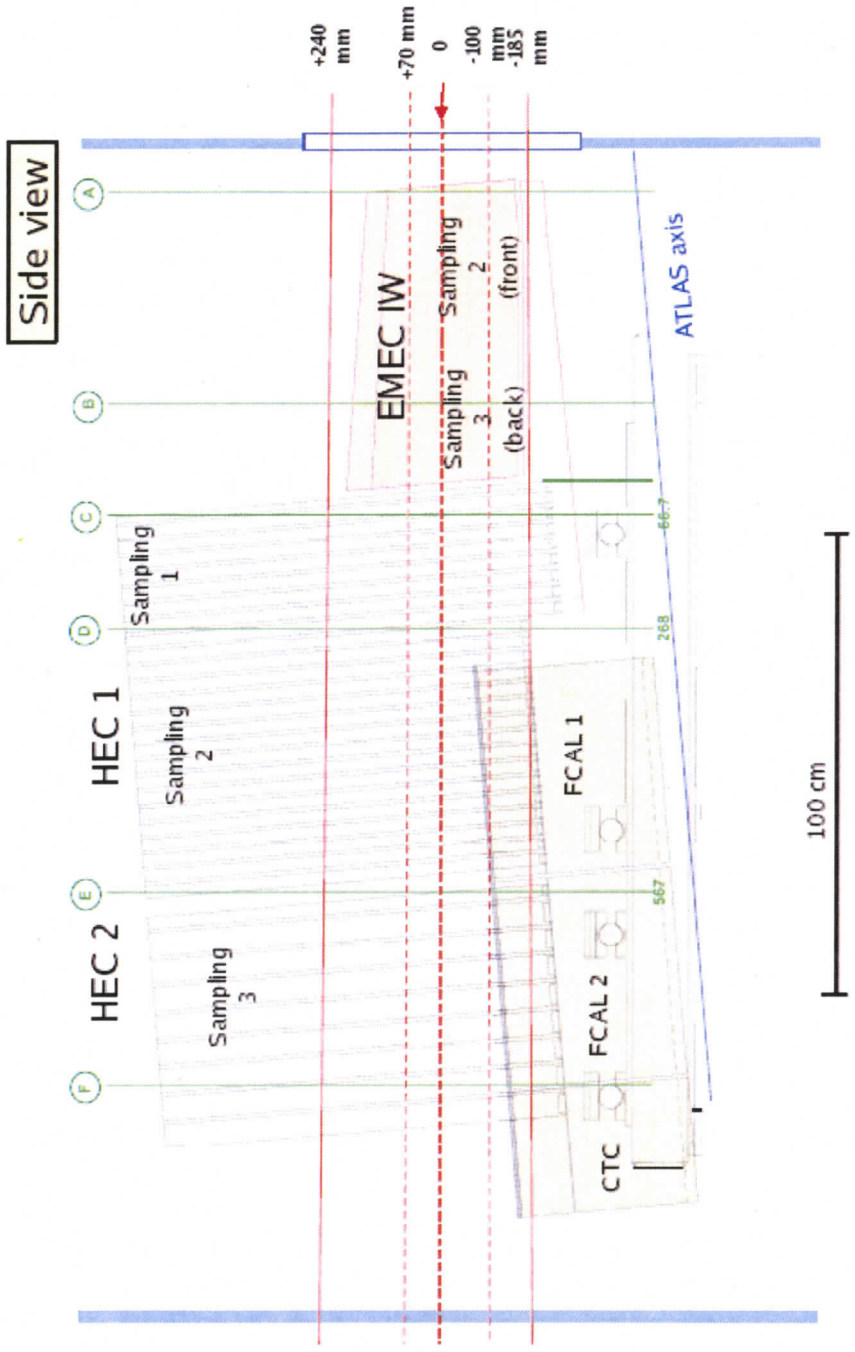

Figure 3.4: Side view of the EMEC, HEC, and FCAL testbeam modules in the cryostat (LAr excluders are not depicted). The particle beams enter the cryostat through the window on the right and travel toward the left. The eight different calorimeter samplings (layers) are labeled.

Recall that there were two running periods in this experiment. The cryostat was raised by 70 mm in between these two periods[4]. Thus, the nominal beam direction is effectively at $|\eta| \approx 2.95$ in period 2.

A head-on view of the calorimeter setup is given in figure 3.5. This schematic shows the front face of the three calorimeters, and also illustrates the $\eta - \phi$ segmented readout cell structure as discussed in section 2.3.

EMEC module

One ϕ module of the EMEC inner wheel (IW), which corresponds to 1/8 of the full ATLAS inner wheel, is used in the testbeam setup. The module is identical to the modules installed in the actual ATLAS end-caps. The ϕ range of this specific module is from $\phi = \frac{11\pi}{16}$ to $\frac{13\pi}{16}$, although this should not matter as the EMEC is symmetric in ϕ. The EMEC IW covers a pseudorapidity range from $|\eta| = 2.5$ to 3.2, and it is positioned such that the center of the EMEC module ($|\eta| = 2.8$, $\phi = \frac{3\pi}{4}$) is in line with the center of the cryostat window. This module, along with the HEC and FCAL modules, are oriented in the cryostat such that pseudorapidity (η) increases with cryostat depth (i.e. the negative y direction in testbeam coordinates).

Above the EMEC module is one of the LAr excluders (see figure 3.2), which is a hard piece of low density foam with a similar X_0 to that of air. It prevents liquid argon from filling the region occupied in ATLAS by the outer wheel of the EMEC.

[4]Details of the modified setup for the second running period are given in section 3.3.

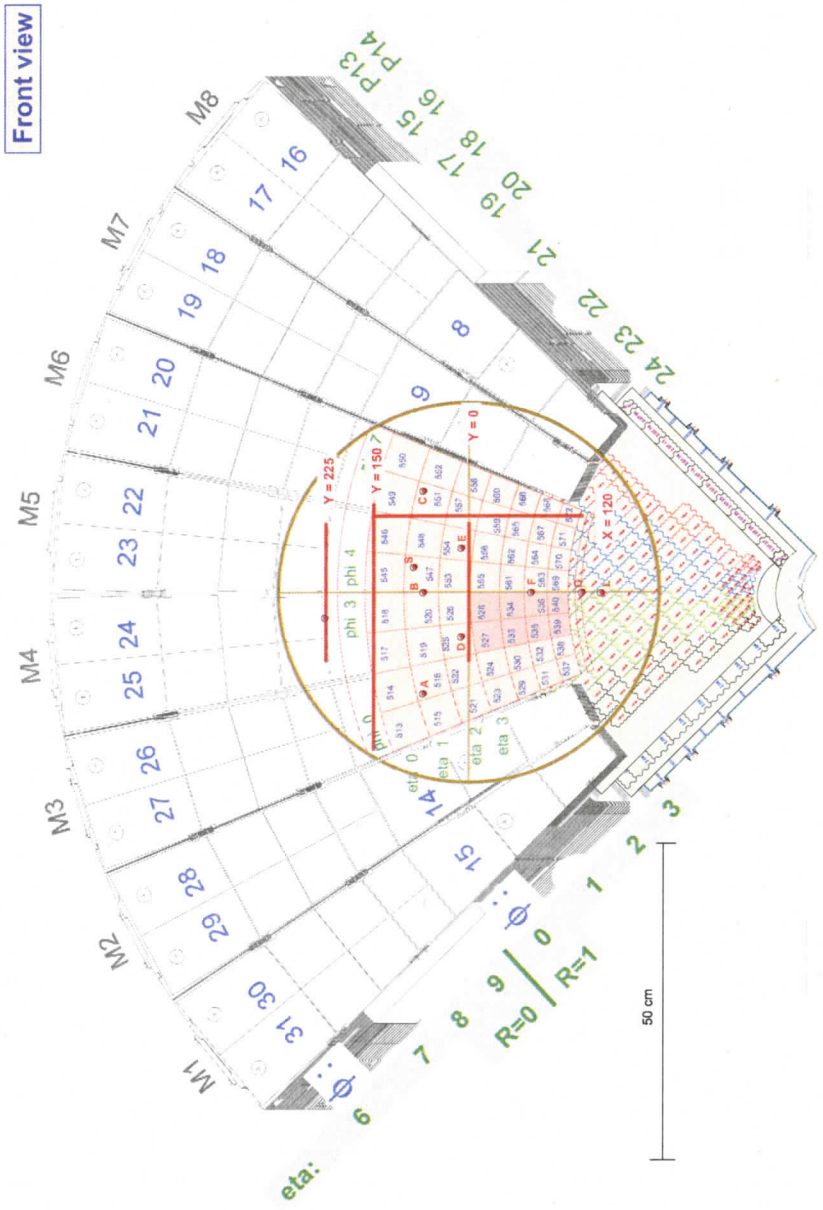

Figure 3.5: Front view of the EMEC, HEC, and FCAL testbeam modules. The circle with cross-hairs is the projection of the cryostat window and the x and y axes. Several standard impact points are labeled with letters. The red lines indicate (in mm) the x and y particle beam impact positions obtained during period 1.

Although the LAr excluder is present, it is not flush with the EMEC module, resulting in a region just above the EMEC that fills with LAr inside the cryostat. This will affect the response to particles impacting this region.

HEC modules

Eight of the 32 ϕ modules that make up the HEC are used in this testbeam. Due to the high η region being studied by this testbeam experiment and the orientation of the apparatus, eight full HEC modules would be too high and wide to fit in the cryostat. Furthermore, the full longitudinal thickness of the HEC2 wheel would not fit in the cryostat. Hence, special HEC1 and HEC2 "mini-modules" had to be constructed specifically for this testbeam. The mini-modules have identical specifications as full HEC modules except that they are shortened to cover only the inner half of the wheel. Thus, the HEC mini-modules cover a pseudorapidity range of approximately $2.1 < |\eta| < 3.2$. The full longitudinal extent of the HEC1 wheel (24 LAr gaps) is preserved in the mini-modules. The cryostat dimensions constrain the HEC2 wheel mini-modules to have only half the z depth (8 LAr gaps) as the full HEC2 wheel. Figure 2.9 illustrates the fraction of the full ATLAS HEC used in this testbeam.

FCAL modules

There are three forward calorimeter modules used in the combined beam test. The first and second FCAL modules in the testbeam setup have the same specifications as

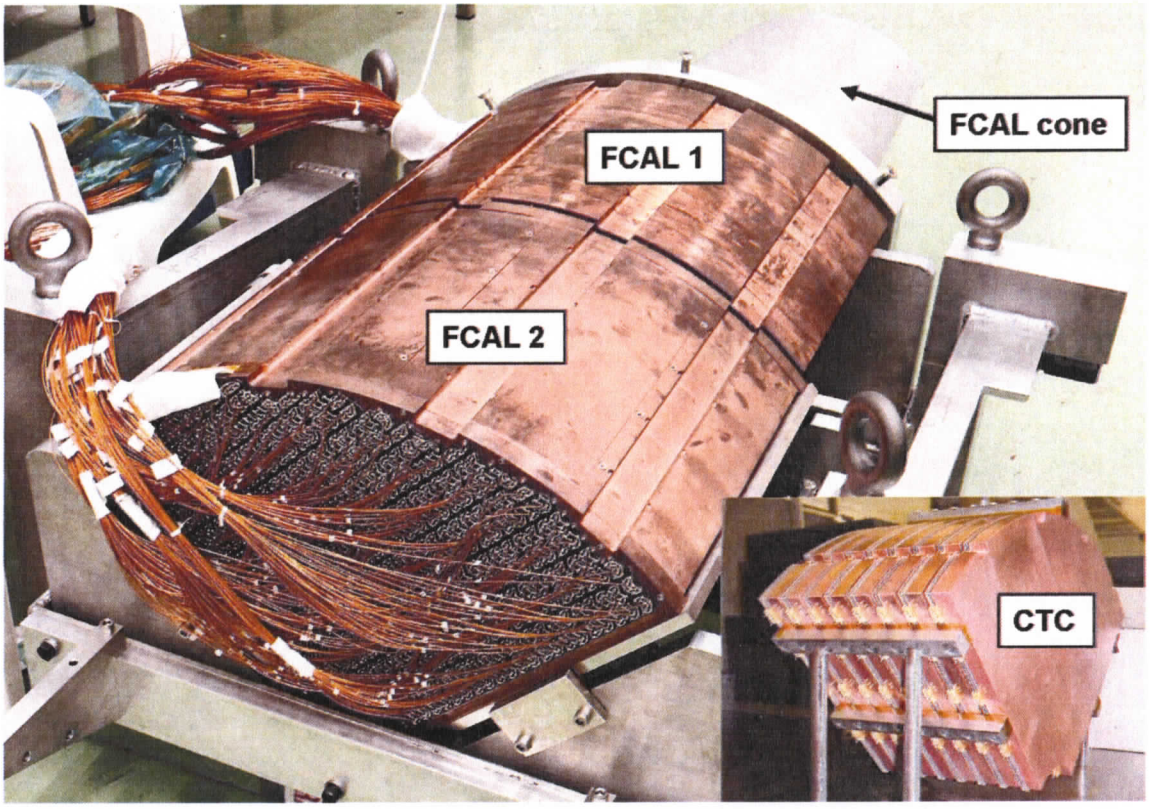

Figure 3.6: The 2004 testbeam FCAL1 and FCAL2 modules in their support structure, prior to assembly with the EMEC and HEC. The support structure includes the FCAL cone which is an extension of the FCAL tube, and provides structural support for the end-cap cryostat. The inset image is of the CTC during construction. The CTC sits directly behind the FCAL2 module in the testbeam apparatus setup.

the ATLAS FCAL1 and FCAL2 modules, but are only a 1/4 ϕ-wedge of the wheel. Figure 3.6 shows the FCAL1 and FCAL2 testbeam modules in their support structure prior to their assembly with the EMEC and HEC modules. In front of the FCAL1 module is the FCAL *cone*: the aluminum conical-shaped flange that extends out from the FCAL support tube (in ATLAS) and is structurally apart of the end-cap cryostat. The EMEC inner wheel module is positioned directly above the FCAL cone.

It is important to include the cone in the testbeam apparatus as it introduces some dead-material that will affect the response in this region of the end-cap.

In ATLAS, the region in front of the FCAL modules does not have any liquid argon. Therefore, a LAr excluder positioned in front of the FCAL is required in the testbeam setup, and can be seen in figure 3.2. This LAr excluder is flush with the cone and extends downward to prevent LAr from filling the region upstream of the FCAL1 module. However, a small separation between the EMEC and the cone can be seen, and this region will fill with LAr when the cryostat is filled.

In ATLAS, the FCAL2 module is followed by a second hadronic wheel (FCAL3) and an absorber plug. There was insufficient space in the testbeam cryostat for a FCAL3 module and an absorber plug. Instead, an instrumented absorber plug called the Cold Tail-Catcher (CTC) was used, and is shown as the inset image in figure 3.6. The CTC uses copper parallel plates, separated by LAr gaps and η and ϕ segmented readout electrode pads. It is the same size as the FCAL testbeam modules, and covers the same η-ϕ range. The inset image shows the CTC module alone during assembly, but in the testbeam experiment the CTC sits behind the FCAL2 module. Unfortunately, the CTC did not perform well in the beam tests. There was negligible change in the CTC energy response regardless of the impact point and beam energy, and at all times the response was very noisy. Therefore, the CTC is not used in this analysis.

3.3 Modified Setup for Period 2

Up to this point, the discussion of the geometry of the beam test setup has been for data acquisition period 1. It was discovered near the end of the first running period that one of the main beam test objectives, namely illuminating the transition region between the EMEC, HEC, and FCAL detectors with energetic particle beams, was not going to be adequately achieved with the existing geometry [26]. To understand the transition region a run program necessarily must start with a beam position that produces a fully contained shower in the EMEC and HEC, pass through the FCAL/HEC boundary and the EMEC/cone/FCAL boundary, and finish with a fully contained shower in the FCAL. Furthermore, one would want several runs of different energies up to and including the maximum beam energy of 200 GeV. It was realized that fully contained showers in the FCAL were not going to be possible. Recall that the table holding BPCs and counters (figure 3.1) is moved vertically with changing impact position in order to keep the beam passing through these detectors. It is the lower limit of the table movement that limits the exposure of the FCAL to particle beams. Furthermore, at beam energies above 150 GeV it is the bending power of the Bend 9 magnet that limits the vertical deflection: a beam with the maximum energy of 200 GeV can only be deflected to $y = -140$ mm. Referring back to figure 3.4, these two factors only allow the very top region of the FCAL to be exposed to particles, and do not allow for full FCAL containment of showers [26].

Period 2 Cryostat displacement
$\Delta x = +3$ mm
$\Delta y = +70$ mm
$\Delta z = +4$ mm

Table 3.2: Period 2 cryostat position with respect to the original testbeam coordinate system.

In order to achieve better FCAL exposure, especially with the higher energy beams, the collaboration decided to raise the cryostat by 70 mm and to install a second bending magnet at Bend 9. Before the cryostat could be moved the liquid argon was transferred to a storage vessel for weight and safety reasons. The cryostat was kept cold, raised the desired amount by inserting more spacer plates under the cryostat, and then refilled. These modifications were performed during the weeks between the two data acquisition periods. The final position of the cryostat with respect to the original coordinate system from period 1 is summarized in table 3.2. The small shift in x is corrected for in period 2 preserving the symmetry about $x = 0$. Figure 3.7 illustrates how the cryostat and the LAr detectors are now raised up with respect to the testbeam coordinate system: the center of the cryostat window and the EMEC module are now at a position of $y = +70$ mm. The limits that the beam detector table imposes on the vertical range are also given in the figure. Impact points A through G are the same as in period 1. Three new impact points are added for period 2: points I and J which sit on the x-axis, and point H which is lower into the FCAL. The green lines indicate the x and y position scans taken during period 2.

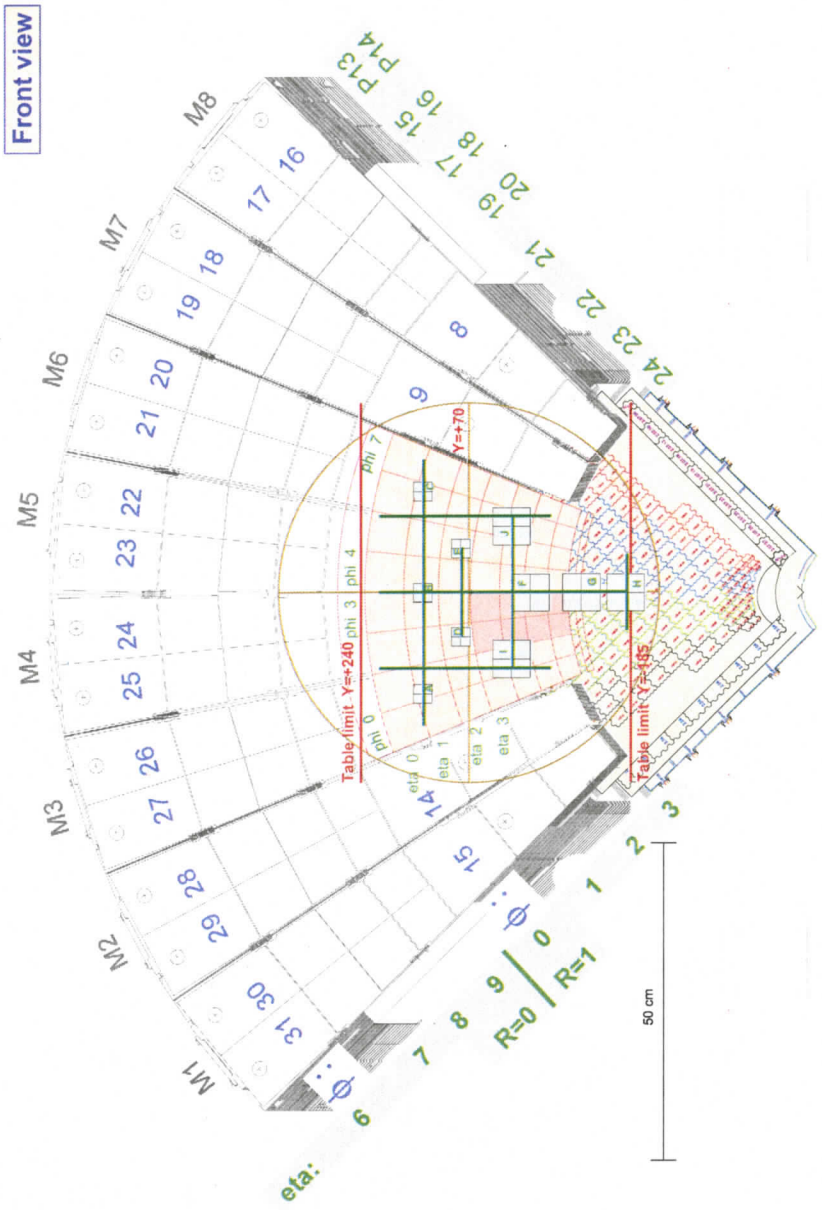

Figure 3.7: Front view of the EMEC, HEC, and FCAL testbeam modules during period 2, illustrating how the apparatus has been shifted vertically +70 mm compared to the first running period. It also shows three new standard points (I,J,H) and the paths of the beam position scans performed during period 2.

3.4 Impact Points and Detector Layers

Accessing the different η-ϕ regions (or in terms of testbeam coordinates, the x-y regions) of the detector is accomplished using a combination of beam deflection and cryostat movement. The table holding the cryostat moves ± 30 cm left and right allowing the incident beam to impact the different x positions. The bending magnet at the end of the beam pipe (Bend 9 magnet in figure 3.1) deflects the beam up and down in the y direction. The amount of vertical deflection depends on the beam momentum and the magnetic field, but it is approximately ± 25 cm at the cryostat.

The side view of the testbeam calorimeter modules (figure 3.4) illustrates that there are a total of eight samplings (z-layers) in the end-cap calorimeters (two in the EMEC, and three in each of HEC and the FCAL). Also depicted in that figure are six vertical planes labeled A through F, approximately corresponding to the front face of each of the different sampling layers. Figures 3.8 through 3.14 illustrate those planes as seen from the point of view of the incoming beam. They show the cell structure of each calorimeter sampling layer, and the projection of the nominal beam impact points and beam paths for running period 2 onto the sampling layer face. This allows for a clear indication of what regions of the different layers are being illuminated by a beam of particles for a given impact point. These figures are for the second data acquisition period because only data obtained during period 2 is used for the analysis given in subsequent chapters.

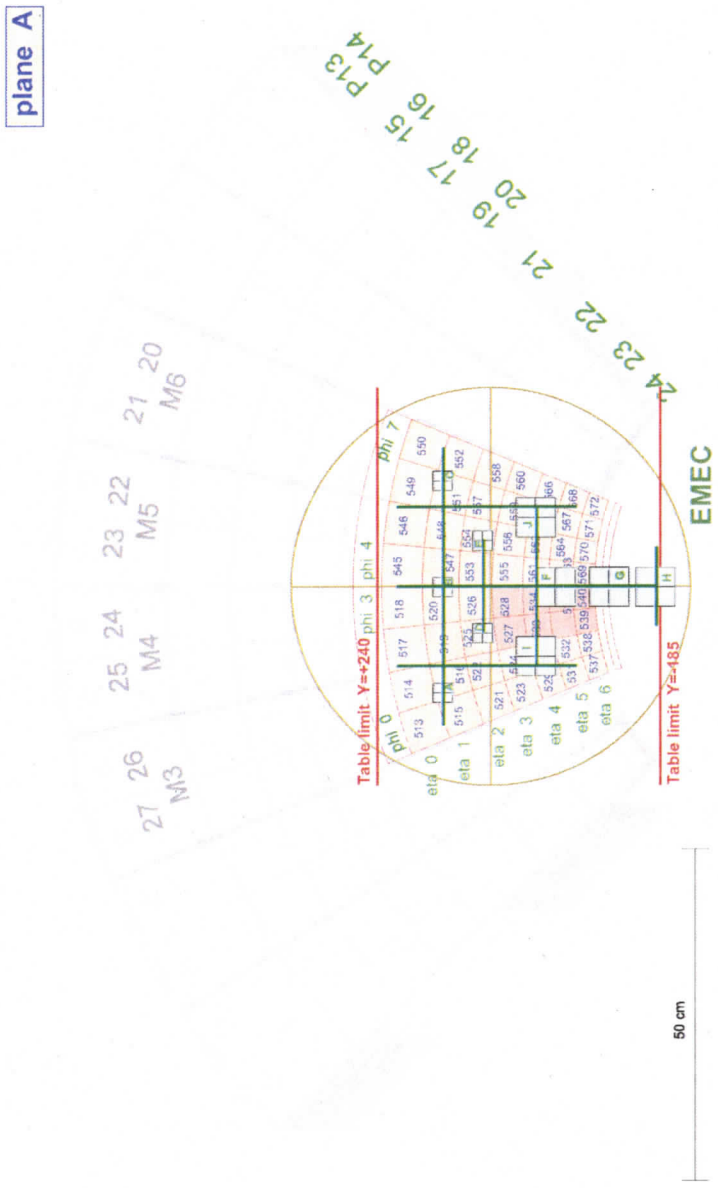

Figure 3.8: Schematic view of the front of the EMEC inner wheel front layer (sampling 2). The cryostat window and period 2 impact points are projected onto the $\eta - \phi$ segmented readout cells.

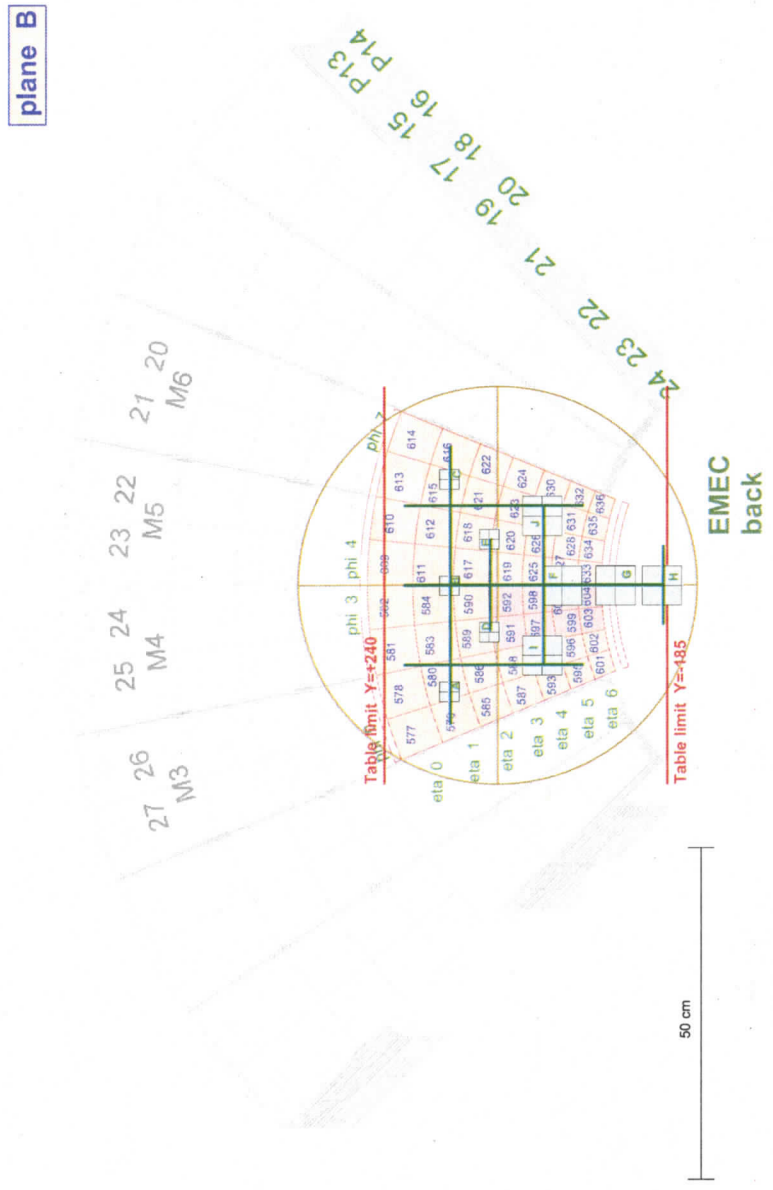

Figure 3.9: Schematic view of the front of the EMEC inner wheel back layer (sampling 3). The cryostat window and period 2 impact points are projected onto the $\eta - \phi$ segmented readout cells.

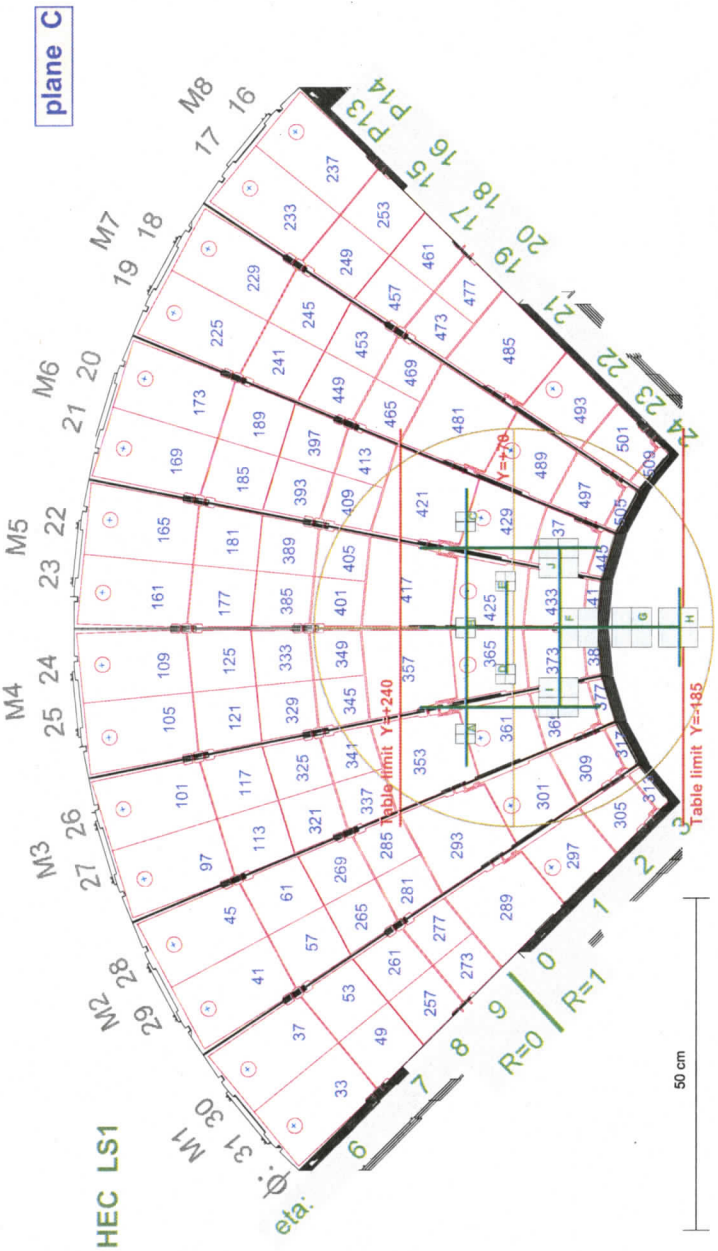

Figure 3.10: Schematic view of the front of the HEC1 wheel front layer (sampling 1). The cryostat window and period 2 impact points are projected onto the $\eta - \phi$ segmented readout cells.

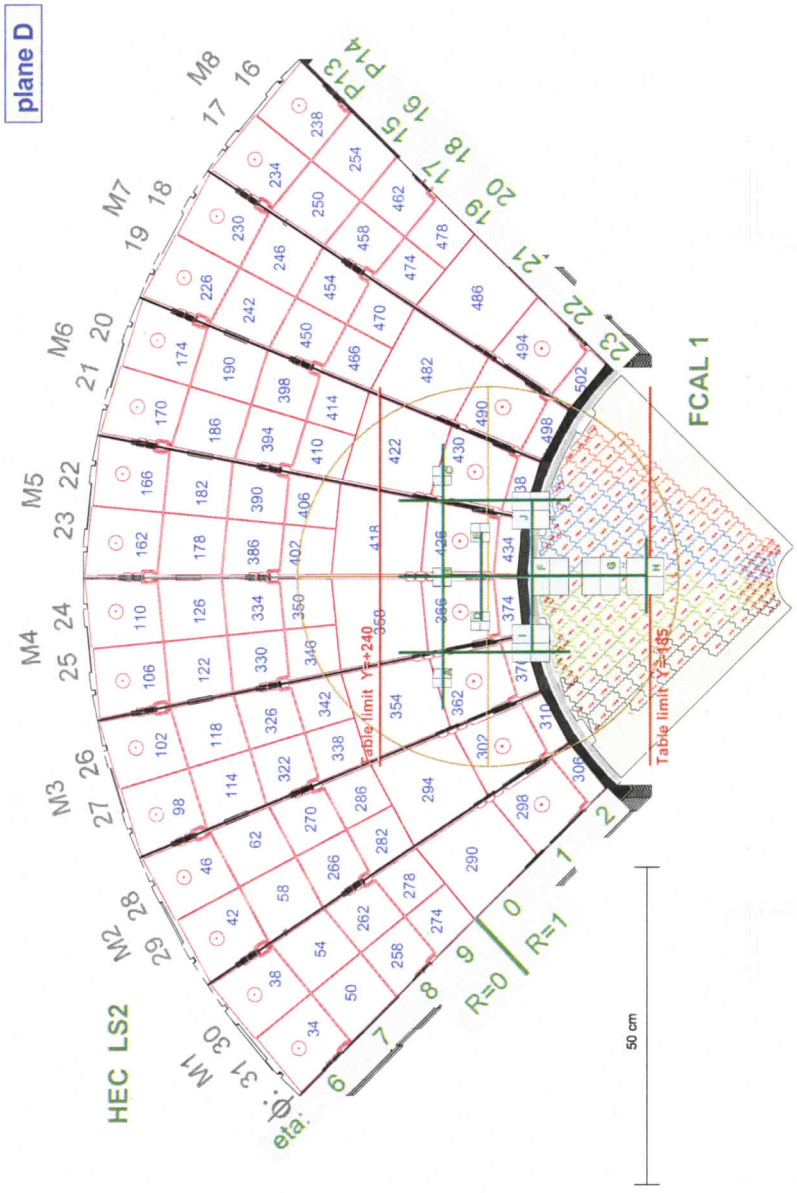

Figure 3.11: Schematic view of the front of the HEC 1 wheel back layer (sampling 2), and the front of the FCAL 1 module. The different coloured FCAL cell outlines indicates the four ϕ sections of the FCAL. The cryostat window and period 2 impact points are projected onto the $\eta - \phi$ segmented readout cells.

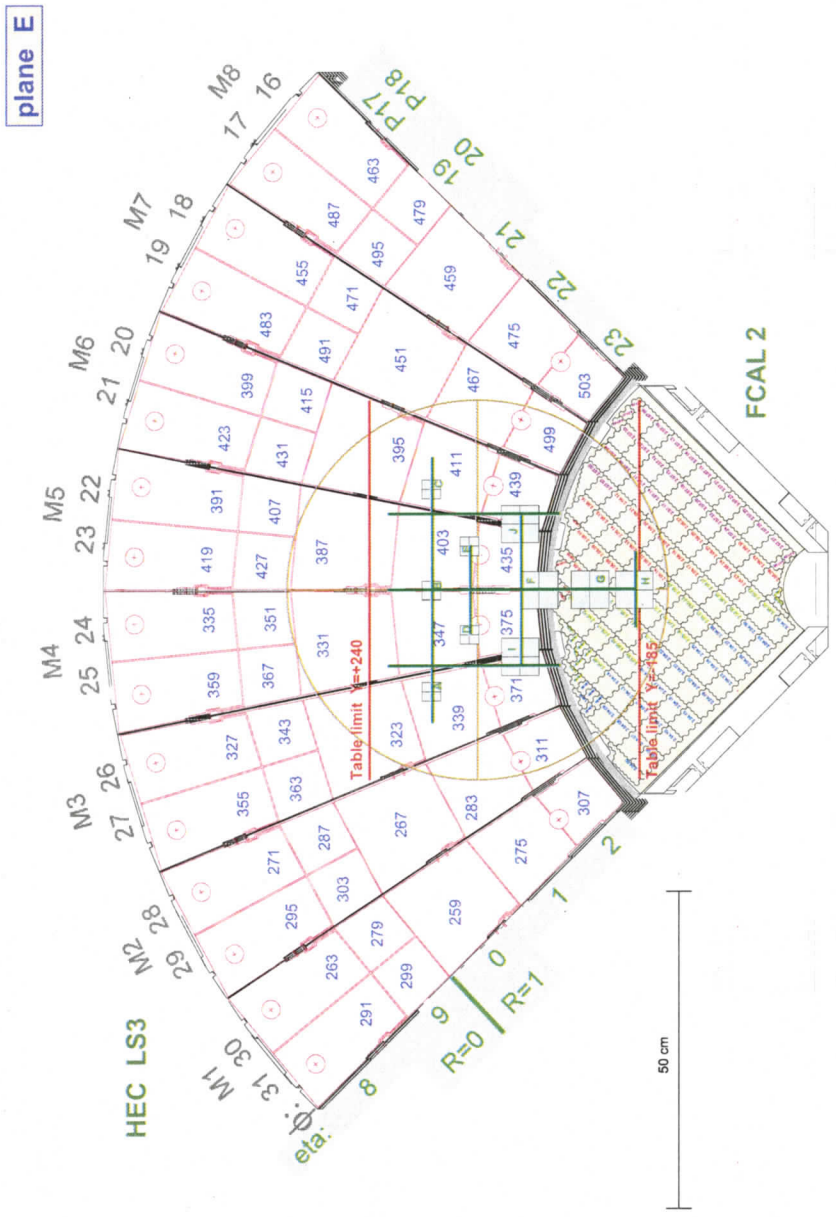

Figure 3.12: Schematic view of the front of the HEC2 wheel front layer (sampling 3), and the front of the FCAL 2 module.The different colours in the FCAL cells indicate the four ϕ sections of the FCAL. The cryostat window and period 2 impact points are projected onto the $\eta - \phi$ segmented readout cells.

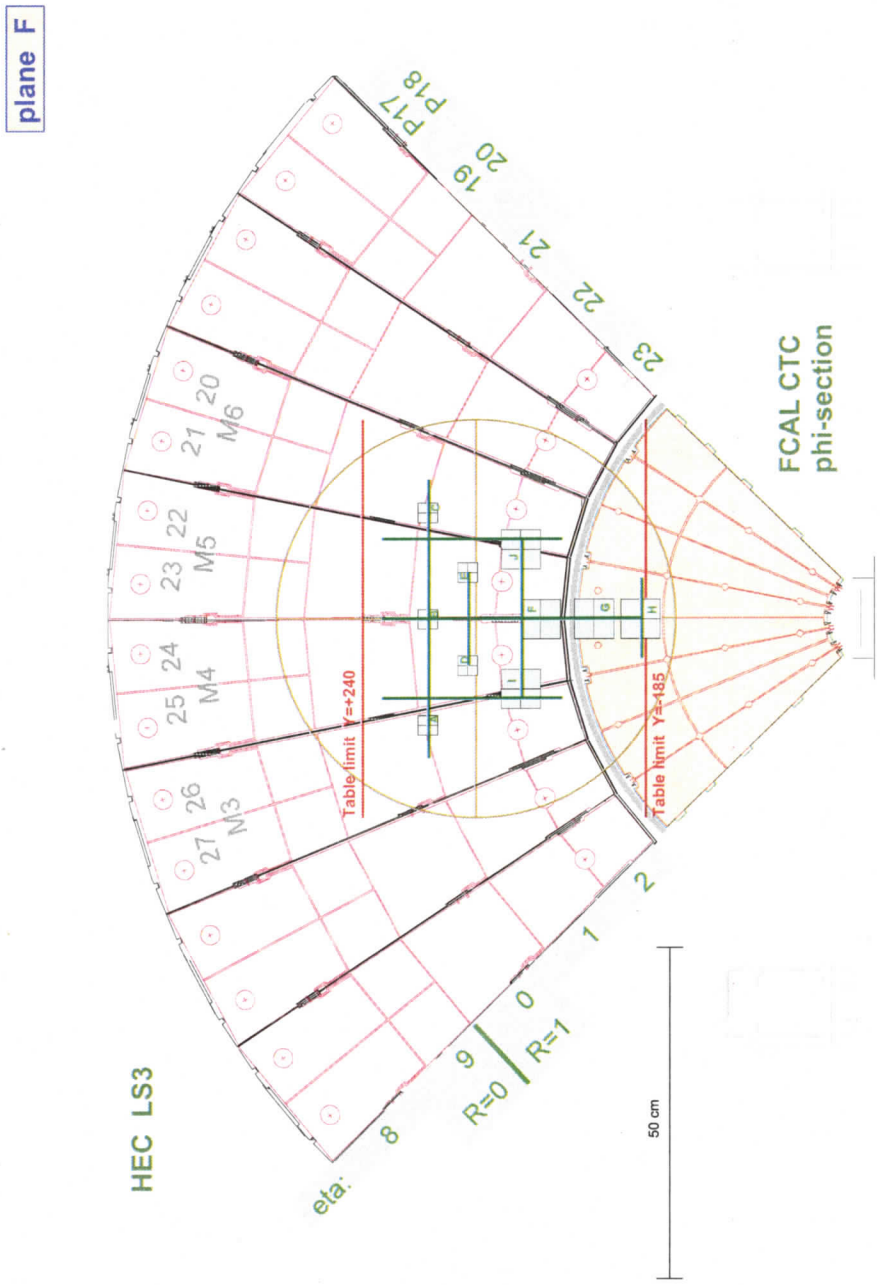

Figure 3.13: Schematic view of the front of the CTC ϕ-section. The cryostat window and period 2 impact points are projected onto the readout cells.

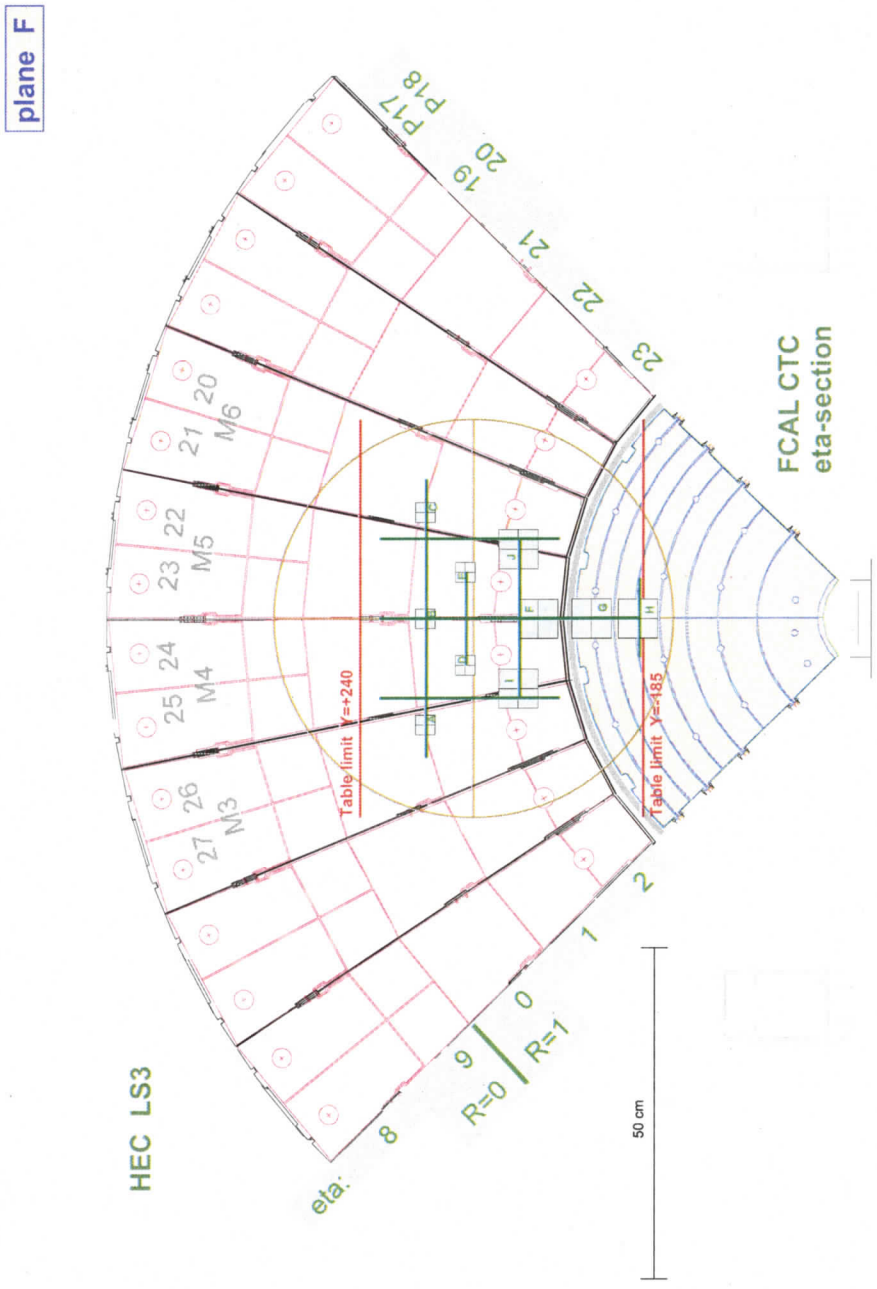

Figure 3.14: Schematic view of the front of the CTC η-section. The cryostat window and period 2 impact points are projected onto the readout cells.

Chapter 4

Signal Reconstruction

Particles passing through the calorimeters create electromagnetic and/or hadronic showers. The ionization produced in the LAr gaps by the charged shower particles is proportional to the energy of the incident particle that initiated the shower in the event. This chapter discusses the procedure by which the electrical signal is reconstructed.

4.1 Event Pre-selection

Prior to reconstructing the calorimeter signal, pre-selection cuts are performed in order to eliminate problematic events from a run. Recall the event trigger for initiating a testbeam event is the simultaneous observation of signals in the beamline detectors S1, S2, and S3 (see section 3.1). Using three scintillators for the event trigger ensures that the incident particle has the correct trajectory. However, some events scatter

away from the intended trajectory, or may just be halo particles on the very edge of the beam. These events are removed from the dataset offline by using the signals in the Hole (H) and Veto (V) counters (figure 3.1). In a typical run there are approximately 20000 events, and this cut removes up to ~70% of the events.

There are occasional events where multiple particles impact the detector at the same time, but are recorded as only one event. The source of these multiple-hit events could be beam particles lacking sufficient separation in time. Additionally, when a single beam particle passes through the beam detectors it may emit Bremsstrahlung photons in the forward direction that are accepted along with the beam particle [27]. These events need to be removed from the run because the energy deposited from these two or more particles would be incorrectly reconstructed as one event. An offline software tool [27], that uses signals from scintillators S2 and B2, removes these events from the run. Approximately 9% of the events in a run that survived the first pre-selection cut are removed due to multiple-hits.

When considering $e^{\pm}$ or $\pi^{\pm}$ runs, any other type of particle in the beam is considered to be beam contamination. Muons are identified using detectors M1 and M2, which are walls of scintillation counters placed on either side of the iron beam stop behind the cryostat. Muons have a low interaction cross section with matter and will typically pass through the entire detector setup, including the iron beam stop, and produce a coincidence of signals in detectors M1 and M2. An offline software tool [27] removes any such events, totaling approximately 6% of the remaining events.

Additional event selection is discussed in section 6.2.

4.2 Signal Shape and Digitization

The pre-selection cuts remove the undesirable events from the dataset. For the remaining events, the signal produced when the particle interacts with the calorimeters must be reconstructed. Although the EMEC, HEC, and FCAL detectors are constructed from different materials and have different geometries, the way the detectable signal in the LAr gaps is produced is the same. An applied high voltage creates an electric field across the LAr gap. When a charged particle (from the beam or the ensuing shower) crosses the LAr gap it ionizes the liquid argon along its trajectory. The ionization electrons move in the presence of the applied electric field producing a current. A uniform density of ionization in the LAr gap produces a triangular current pulse; see figure 4.1 for a normalized example. The induced current is initially a maximum (I_0) when all the ionization electrons are drifting, and it steadily decreases in time. When the electrons furthest from the anode have drifted across the LAr gap the current amplitude returns to zero.

The ionization signal in a LAr cell is amplified and shaped into the recorded pulse shape, shown as the curved pulse in figure 4.1. The shaper is designed to make the pulse peak quickly in time[1]. The amplitude of the pulse is proportional

[1]Fast pulses are required because of the bunch crossing time interval of 25 ns at the LHC. In the time interval of a singular triangular pulse, several events may occur. By shaping the pulses to have a fast response the pile up is reduced.

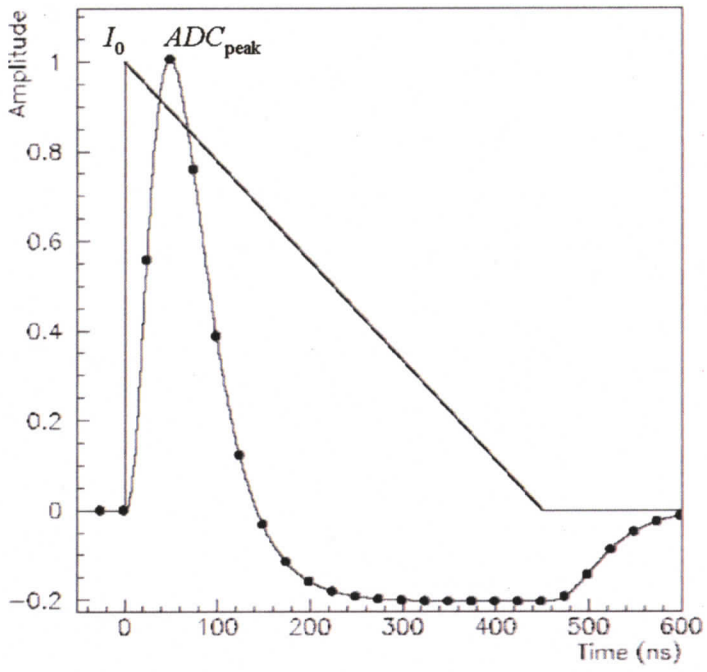

Figure 4.1: Typical signal shapes: the triangular ionization shape produced in the LAr gap, and the readout physics pulse shape with time samples (points) indicated [14].

to the initial current signal, and the bipolar pulse shape has equal areas above and below the baseline. An analogue-to-digital converter (ADC) digitizes the signal every 25 ns (shown as the black dots in the figure) using a 40 MHz clock. Therefore, the time samples have units of ADC counts. In the beam tests, calorimeter signals were sampled 16 times in the first running period and 7 times in period 2. Signal reconstruction methods aim to obtain the most precise and unbiased value for the peak amplitude (ADC_{peak}) from the discrete dataset obtained from digitization.

4.3 Gain mode

The peak amplitude of the physics pulse also depends on the gain of the electronics used during data acquisition. The gain specifies how much amplification is applied to the signal. The readout electronics have three different gains for each calorimeter channel signal: high, medium, and low gain (although low gain was never used during this testbeam). The detectors can each be operated in either a fixed gain mode or in *Autogain* mode. The Autogain mode selects the gain setting for data acquisition depending on the signal amplitude. If the signal is sufficiently high, the gain switches from high to medium so that the signal does not exceed the maximum amplitude of the ADC, and also remains in the linear range of the amplifiers. The gain modes used by the calorimeter modules during both running periods are presented in table 4.1 [28].

Calorimeter	**Period 1**	**Period 2**
EMEC	Medium gain	Autogain
HEC	Medium gain	Medium gain
FCAL	Autogain	Autogain

Table 4.1: Gain modes for the different calorimeters in the beam test.

4.4 Pedestals

The average electronic output of a channel when there is no signal present is called the pedestal, and it is typically an averaged non-zero value of ADC counts. Therefore, in a testbeam event the signal to be reconstructed is not the absolute amplitude, but the

peak amplitude above the pedestal. Pedestals need to be obtained for each channel at each gain. Different methods are available to obtain pedestal values. Dedicated pedestal runs can be taken where channels are readout without any incident particles present. The resulting average signals from the channels are the pedestal values. Alternatively, the pedestal for each channel can be obtained by averaging the first sample, called "sample 0", of the signal from each channel. The timing of the trigger that initiates an event is such that the first time sample occurs before the pulse starts. The pedestals used for data analysis in this thesis are obtained by averaging the "sample 0" values over an entire run for each channel at each gain. This method for obtaining the pedestals is advantageous because the baseline measurement is taken under the same experimental conditions as the signal being reconstructed.

4.5 Event Phase and Pulse Shape Accumulation

The digitization of the physics pulse shape, shown as the black data points in figure 4.1, is an ideal case for amplitude reconstruction because the fourth sample has recorded the exact signal amplitude. This is not the typical case in testbeam data acquisition because the time of an event trigger[2] is not synchronized with the 40 MHz digitization clock[3]. This implies that the exact peak of the pulse is not typically recorded, but must be reconstructed from the time samples surrounding the peak.

[2]The event trigger is discussed in section 3.1.

[3]In ATLAS the proton bunch crossings occur every 25 ns and will be synchronized with a 40 MHz event digitization clock.

The difference between the time of the event trigger and the time of the next cycle of the digitization clock is called the event phase, and it will be some number of nanoseconds between 0 and 25 [29]. The event phase is computed using information recorded by a time-to-digital converter[4] (TDC).

Because of the asynchronous nature of the arrival of the beam particle, the event phase varies from event to event. By accumulating sets of pedestal-subtracted time samples with different event phases, an overall pulse shape is obtained for each channel at each phase and each gain. A cubic polynomial interpolation of the pulse is then used to normalize the pulses. Pulse shapes for some channels are not possible due to insufficient signal strength above the pedestal, or because of insufficient data for some phases. For these channels, the average pulse shape over all channels in the same calorimeter layer is used. See reference [28] for further details.

4.6 Digital Filtering

Armed with the event phase and pedestal-subtracted pulse shapes for each channel at each gain, the peak amplitude of the channel signal can be reconstructed from the digitized time samples. The signal peak amplitude, ADC_{peak}, is computed using the optimal filtering method [30]. This method extracts the peak amplitude from the

[4]In fact, there were two TDCs used simultaneously during the data acquisition. An offline software tool assigns a quality factor to each TDC for the event, and the phase is computed using the TDC of highest quality. A selection cut is applied to remove events with low quality factors. Further details can be found in [29].

time samples, while minimizing the effect of noise, by forming linear combinations of appropriately weighted time samples. The weights applied are called optimal filtering coefficients (OFCs), and are obtained for each channel by using the event phase, the accumulated pulse shapes, and the samples' autocorrelation functions [31].

Thus, the peak amplitude is computed as follows:

$$ADC_{\text{peak}} = \sum_{i=0}^{4} a_i S_i \tag{4.1}$$

where a_i are the phase dependent OFCs applied to the S_i time samples. Note that only five OFCs and time samples are used in the calculation. In period 1, samples 6 through 10 (numbering begins with 0) are used. Samples 1 through 5 are used during period 2. The peak amplitude is then pedestal subtracted: $ADC_{\text{peak}} - ADC_{\text{ped}}$, and the result is the signal amplitude (in ADC counts) deposited in a calorimeter cell.

To summarize this chapter, charged particles passing through the calorimeters produce detectable signals in the form of electrical currents due to ionization in the LAr gaps. The current pulses are readout, amplified and shaped. The amplitude of the shaped pulse, which is proportional to the ionization, is sampled and reconstructed using optimal filtering. The next step in the reconstruction chain is to relate the total signal produced in the calorimeter to the total energy deposited in the calorimeter. This is called calibration, and is presented in the following chapter.

Chapter 5

EMEC Calibration

This chapter presents the details of the calibration procedure for the electromagnetic end-cap calorimeter, and presents a study of different methods of obtaining the calibration coefficients.

As indicated in the previous chapter, the amplitude of the calorimeter signal is proportional to the amount of energy deposited by an incident particle. The nature of this relationship is obtained by calibrating the detector with a known signal. A simple approach to calibration would be to relate the particle beam energy, which is a known quantity in beam tests, to the total calorimeter signal. Calibrating the detectors this way provides a relationship between the deposited energy (in GeV) and the calorimeter signal response (in terms of ADC counts). The physical observable is the current generated at the LAr gap level. The current produced in any given LAr gap depends on factors specific to that specific cell: the capacitance which changes

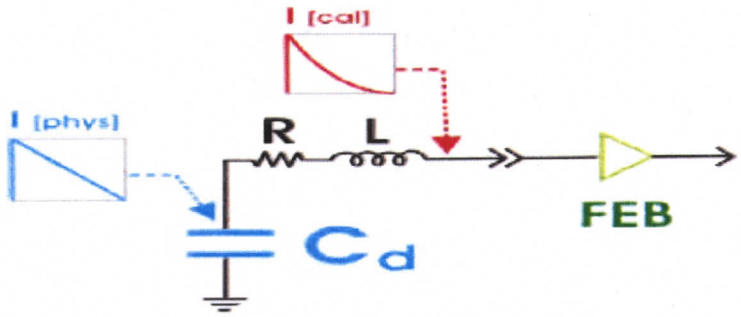

Figure 5.1: Illustration of an EMEC liquid argon cell circuit [32]. The triangular physics current pulse (I_{phys}) is produced at the detector LAr gap whereas the calibration pulse (I_{cal}) has an exponential fall and is injected at a later point in the circuit. The different pulse shape and injection point of the calibration pulse produces a slightly different response to physics and calibration signals, and will have to be corrected (see discussion in section 5.5).

with LAr gap thickness, and the applied high voltage. Thus, for the same amount of ionization, different calorimeter cells give different responses. Therefore, the simple approach is not sufficient because it does not take into account the cell-to-cell variation in response.

What is required is a calibration scheme that is performed on the cell level. The calorimeters are constructed with calibration circuits that inject a known current at the cell level. Figure 5.1 illustrates an EMEC LAr cell as a simple RLC circuit: the physics current pulse (I_{phys}) comes from the LAr gap in the detector and travels through the readout line to the amplifier and shaper on the front end board (FEB). The calibration circuit uses a Digital-to-Analogue converter (DAC) to inject a voltage pulse across the calibration circuit resistor network creating a current pulse (I_{cal}). Once the relationship between the injected current pulse and the response is known

for each cell, the known beam energy can be used to finally relate the calorimeter response in terms of observed current to the electromagnetic (EM) energy scale (refer to section 2.2.4). Thus, several factors contribute to cell-level calorimeter calibration. The following section in this chapter provides an overview of the calibration chain, and subsequent sections provide the details.

5.1 Calibration Coefficients Overview

A properly calibrated detector means that a relationship has been found, for each cell at each gain, that converts ADC counts recorded by the detector electronics to the EM energy scale (MeV) of the incident particle. The overall calibration coefficients converting from ADC to MeV have three contributing sub-factors. The first are the *ramp* calibration coefficients, P_1 (linear) and P_2 (quadratic), that define the relationship between the injected calibration pulse (DAC counts) and the resulting channel signal amplitude (ADC counts). The second sub-factor, $DAC2\mu A$, is an electronic parameter that relates the DAC counts from the pulser to the physical current (in μA) at the cell level. The final sub-factor is the electromagnetic scale factor, α_{EM}, which converts the current in a cell to the EM energy scale. The details of these three sub-factors are explained in the following sections of this chapter.

Thus, the overall calibration coefficients, c_i, for a cell are computed as:

$$c_1\left(\frac{\text{MeV}}{\text{ADC}}\right) = P_1\left(\frac{\text{DAC}}{\text{ADC}}\right) \times DAC2\mu A\left(\frac{\mu\text{A}}{\text{DAC}}\right) \times \alpha_{\text{EM}}\left(\frac{\text{MeV}}{\mu\text{A}}\right) \quad (5.1)$$

$$c_2\left(\frac{\text{MeV}}{\text{ADC}^2}\right) = P_2\left(\frac{\text{DAC}}{\text{ADC}^2}\right) \times DAC2\mu A\left(\frac{\mu\text{A}}{\text{DAC}}\right) \times \alpha_{\text{EM}}\left(\frac{\text{MeV}}{\mu\text{A}}\right). \quad (5.2)$$

These calibration coefficients are applied to the reconstructed signal amplitude for a given cell in order to obtain the cell energy on the EM scale. Recalling from chapter 4 that the reconstructed signal is the pedestal subtracted peak amplitude:

$$ADC_{\text{signal}} = ADC_{\text{peak}} - ADC_{\text{ped}}, \quad (5.3)$$

the energy on the EM scale of a liquid argon cell is therefore given by the following polynomial:

$$E_{\text{EM}}(\text{MeV}) = c_1 \cdot ADC_{\text{signal}} + c_2 \cdot (ADC_{\text{signal}})^2. \quad (5.4)$$

While the above equations are used for computing the calibration coefficients and energy of all end-cap calorimeter cells, only the EMEC calibration is studied in this thesis[1]. The following three sections of this chapter discuss each of the three calibration coefficient sub-factors sequentially. The remaining two sections of this chapter discuss some corrections to the reconstructed energy.

[1]Both the HEC and the FCAL are also calibrated. The HEC calibration follows the same approach as the EMEC. Further details of the HEC calibration can be found in reference [27]. The response of the FCAL, on the other hand, is sufficiently uniform with respect to the required precision that a cell-level calibration is not required. Instead, each testbeam module (FCAL1, FCAL2, CTC) has a constant ADC/MeV calibration coefficient [33].

5.2 EMEC Ramp Study

The ramp coefficients ($P1$ and $P2$) are obtained from specific calibration data taken during the beam tests called calibration runs. Three different methods of obtaining the ramp coefficients are studied and compared to the ramp coefficients from a previous EMEC inner wheel beam test.

5.2.1 Calibration Runs

For the EMEC, a calibration run consists of injecting electronic pulses of known amplitude, channel by channel, into the calorimeter and recording the resulting signals. In each case, the calibration pulse amplitude (in DAC counts) is set, and the corresponding observed signal is measured in ADC counts. As the run progresses, the calibration pulse amplitude is increased systematically[2]. The EMEC calibration board in this testbeam uses a 17 bit DAC with a 5 V full range, meaning the maximum amplitude of a calibration pulse (in units of DAC counts) corresponds to a voltage of 5 Volts. However, the absolute amplitude is never used, but rather the amplitude above a baseline (a non-zero signal at the lowest DAC setting). Thus, the relationship between DAC counts and voltage becomes: $5\text{V} = (2^{17} - 1)$ DAC counts.

The gain of the electronics is fixed during a calibration run, and data is collected for one-half of the full DAC range in a given run. Table 5.1 lists the calibration

[2]The term "ramp" is used to identify this stage in the calibration because the injected calibration pulse is increased systematically, or "ramped-up", and the response is strongly linear, therefore having a "ramp"-like appearance (see figure 5.2).

Period 1			**Period 2**		
Run Number	Gain	DAC Range	Run Number	Gain	DAC Range
80011	Medium	0 – 5000	80031	Medium	0 – 5000
80012	Medium	5500 – 12000	80032	Medium	5500 – 12000
80013	High	0 – 500	80033	High	0 – 500
80014	High	550 – 1200	80034	High	550 – 1200

Table 5.1: Calibration runs used for the EMEC ramp study.

runs used in this study to provide calibration data in both gain modes (High and Medium) for both running periods of the beam tests. Thus, two calibration files are needed for each gain in each period to cover the full DAC range available. Although different calibration runs were used in periods 1 and 2, no change in the resulting calibration coefficients is expected. Comparison between the two sets of calibration coefficients provides a systematic check of the calibration. All of the EMEC ramp calibration coefficients obtained in period 2 are within 2% of the period 1 ramps, and the average difference is 0.5%.

In addition to pulsing the calorimeter channels at different DAC settings over the full DAC range, a specific amount of delay time between when the calibration board injects a pulse and when the ADC begins sampling the resulting signal is set. In the EMEC calibration runs, 25 different delay settings spaced 1 ns apart are used. This corresponds to 0 through 24 ns delay time in the signal readout. Finely binned calibration pulse shapes (also called calibration waves, or *caliwaves*) can be constructed: (25 different delay settings) $\times$ (16 time samples per set) = 400 ns pulses with 1 ns bins. These calibration pulse shapes will be discussed further in the

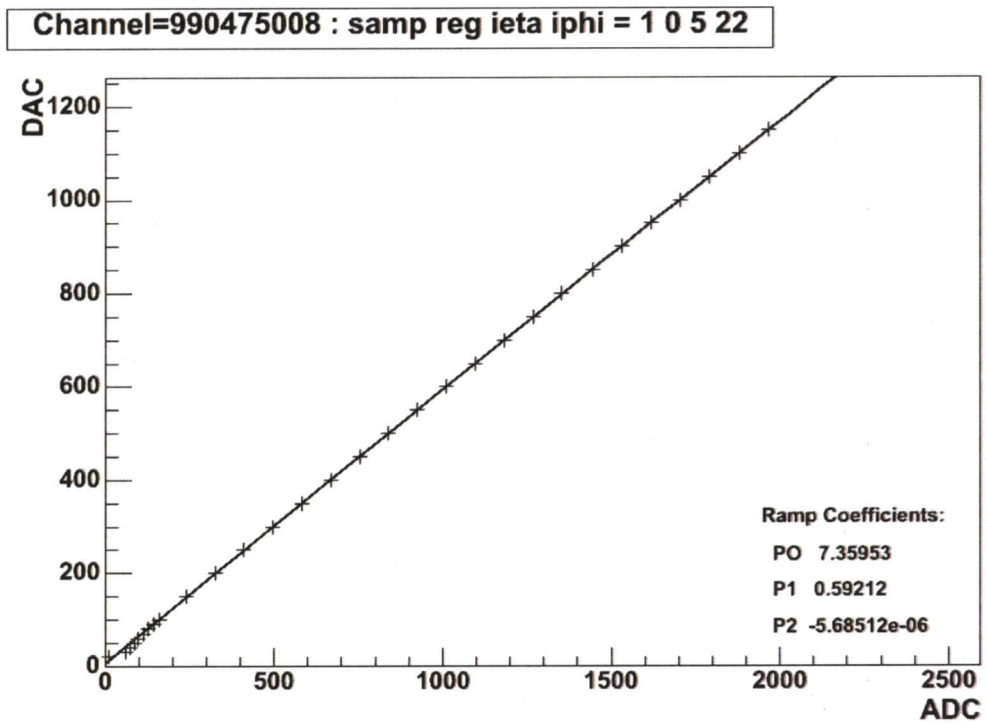

Figure 5.2: Typical EMEC channel ramp calibration graph for high gain mode. A quadratic function is fit to the data, and the coefficients of the fit, P_i, are called the ramp coefficients.

following sections.

During a calibration run the amplitude of the input pulse (in DAC counts) is systematically increased over the full DAC range available, and the peak (ADC_{peak}) of the resulting channel signal shape is reconstructed from 16 time samples (in ADC counts). A calibration graph plots the DAC versus the reconstructed ADC_{peak} for each channel at each gain. An example of one such graph is shown in figure 5.2 which shows the data from a calibration run for a typical channel in the EMEC front

layer at high gain. A second order polynomial[3] is fit to the curve resulting in three ramp coefficients (P_0, P_1, P_2), but it is just the linear and quadratic terms which are included in energy reconstruction (equation 5.4). The constant term P_0 is not used in reconstructing physics data because it reflects an offset only in the calibration system such that when the injected DAC setting is zero, the resulting signal is not.The lowest end of the DAC range (between 0 and 100 DAC counts) is excluded from the fit due to known non-linear behaviour of the calibration pulser. As the figure shows, the ramps are nearly linear, and all channels in both gains show the same linear behaviour. The non-linearity is adequately described by a quadratic term.

Different sets of ramp coefficients are obtained by trying different methods of $\mathrm{ADC_{peak}}$ reconstruction. Three methods of reconstructing the channel amplitude are studied giving rise to three different sets of ramp coefficients. These three methods are presented in the following sub-sections.

5.2.2 Ramp Calibration Methods and Comparison

Three methods of calculating ramps in the inner wheel are considered: the parabolic interpolation method, the multiple-DAC calibration pulse shape (caliwave) method, and lastly, the central-DAC caliwave method. Figures 5.3 and 5.4 show the linear and quadratic ramp coefficients, at high and medium gain, obtained for each of these three methods, along with the ramp coefficients used in a previous inner wheel testbeam.

[3]The use of a quadratic fit to the calibration data also matches what was done in the concurrent EM barrel calorimeter beam tests [34].

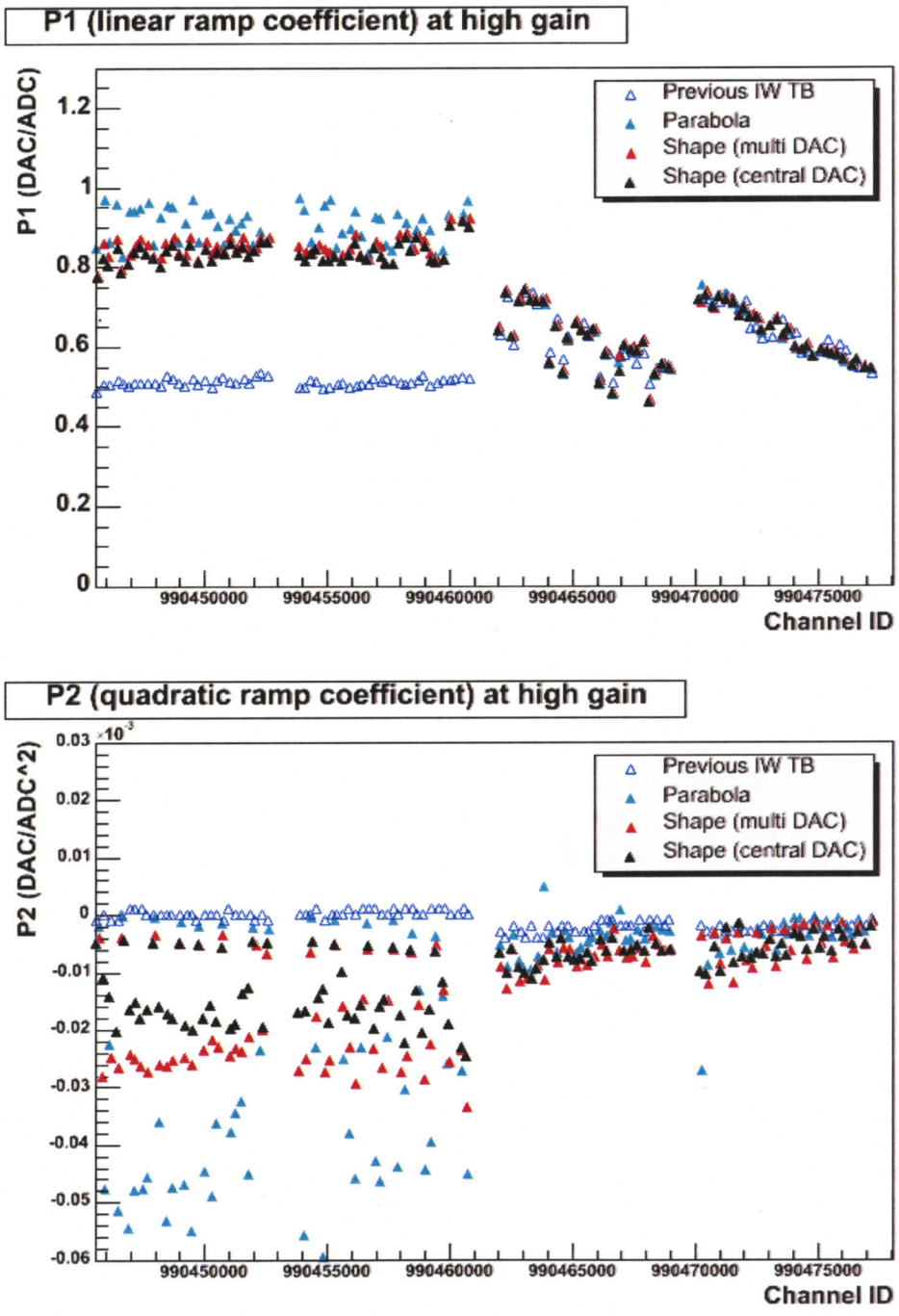

Figure 5.3: Linear (top) and quadratic (bottom) ramp calibration coefficients at high gain for the EMEC inner wheel. Channels in the front layer of the EMEC have IDs above 990461000.

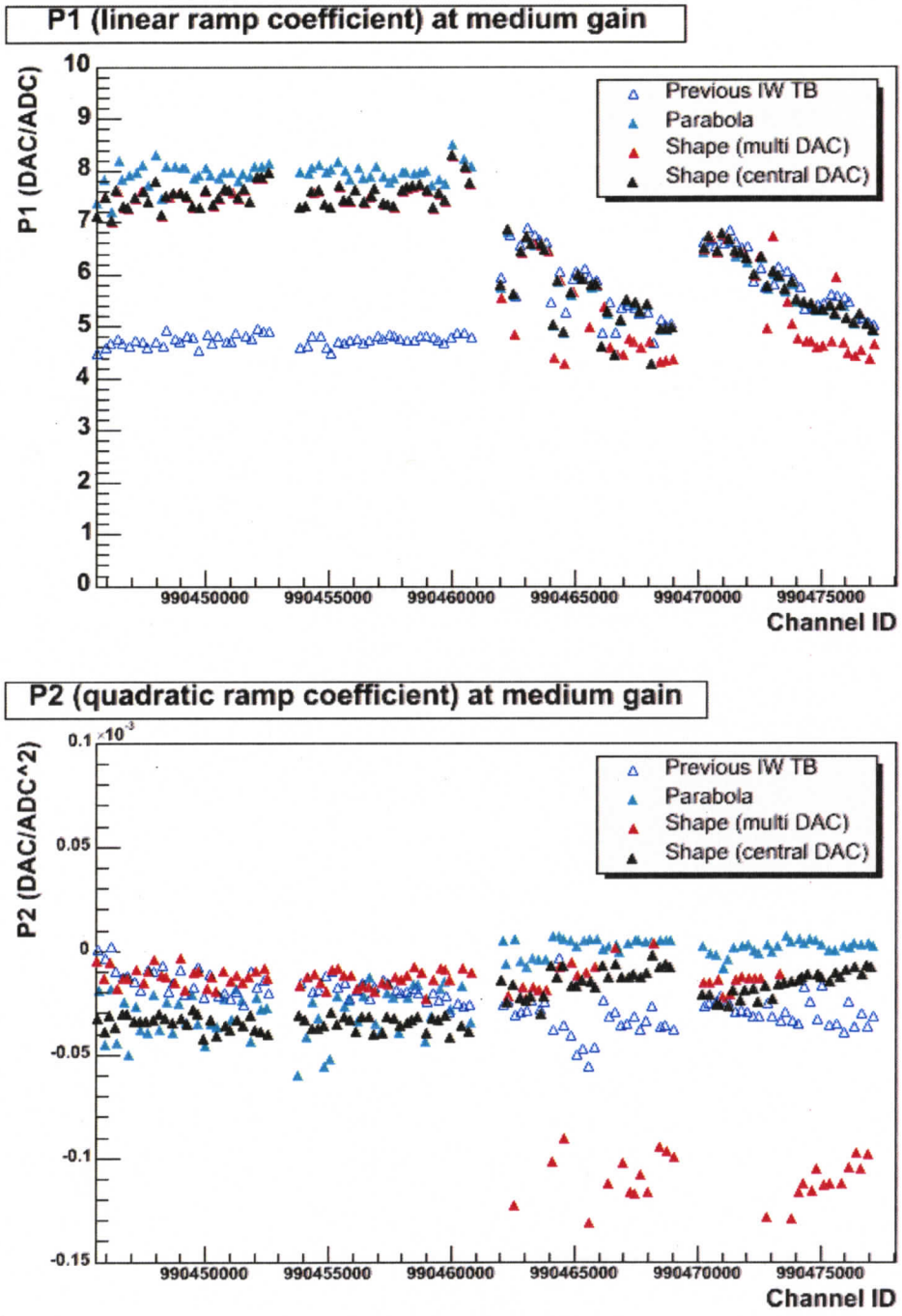

Figure 5.4: Linear (top) and quadratic (bottom) ramp calibration coefficients at medium gain for the EMEC inner wheel. Channels in the front layer of the EMEC have IDs above 990461000.

These factors are plotted as a function of the channel hardware identification number (HWID). There are 112 connected EMEC channels in the detector module in the testbeam setup, and the HWIDs for these channels range from 990445568 to 99077056 incrementing in steps of 256. The cyan, red, and black triangles are the ramps obtained from the parabolic interpolation, multiple-DAC caliwave, and central-DAC caliwave methods respectively. Channels that have IDs less than 990461000 belong to the back layer of the EMEC inner wheel. Channels with IDs above this belong to the front layer. The open blue triangles are the ramps from the previous EMEC IW beam tests [35] shown for comparison. The discrepancy in the back layer between the linear ramp coefficients from the previous testbeam and the present testbeam is discussed following the explanation of the three methods studied.

Parabolic Interpolation Method

The first of three methods for obtaining ramp coefficients is the parabolic interpolation method. The ramps obtained from this method are plotted as cyan triangles in figures 5.3 and 5.4. When the calibration system pulses a channel with some DAC value, the resulting signal is sampled 16 times (once every 25 ns) and pedestal subtracted. However, the actual peak of the signal shape most likely will not have been sampled. The parabolic interpolation method fits a parabola to the three highest pedestal subtracted samples for each channel. The ADC_{peak} for this channel is then equal to the maximum of the fit. Once all the (ADC_{peak},DAC) pairs are obtained

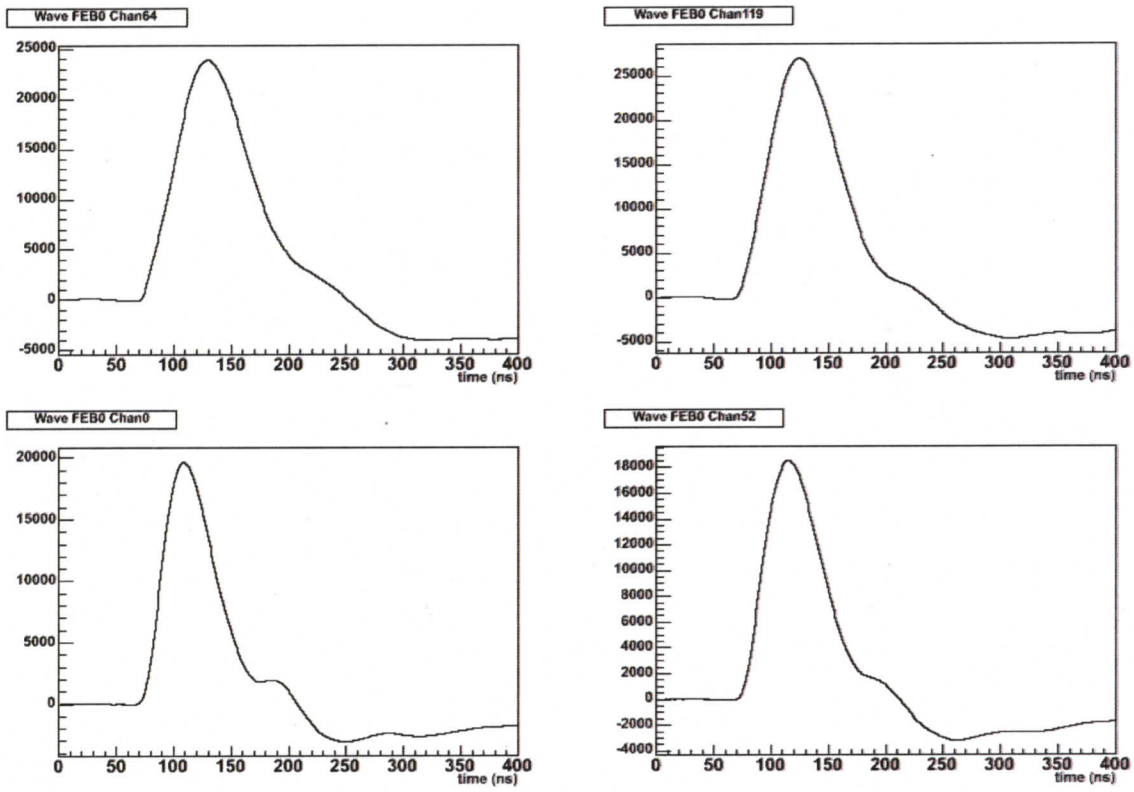

Figure 5.5: Examples of EMEC calibration pulse shapes, obtained from discrete samples taken every 1 ns, for two front layer channels (top) and two back layer channels (bottom).

from the ramp run and plotted on the calibration graph, the ramp coefficients are obtained from the quadratic fit, as outlined in the previous section.

This method is the fastest computationally because it is a simple interpolation and it only requires database access for the pedestal values for each channel. Unfortunately, it is a biased method because the actual signal pulse shape is not parabolic. This is evident in figure 5.5. which shows typical pulse shapes for four EMEC channels at high gain. The pulse shapes also are seen to vary within each layer

of the EMEC and between the front and back layers as well. This introduces a cell dependent bias from the parabolic interpolation of the peak. The fact that this bias exists has been known since early beam tests of the ATLAS EM calorimeter modules. Correction factors which reduce the effect of this bias have been determined for the EM barrel calorimeter, but not for the EMEC.

The calibration graphs are produced from the parabolic interpolation of the calibration data taken at one specific delay setting, but the choice of which delay setting to use is arbitrary. This leads to a 5% spread in the dominant (linear) ramp coefficient. This can be seen in figure 5.6 where the linear ramp coefficient $P1$ has been plotted against the delay value for four EMEC channels. Due to the presence of this bias, it was deemed necessary to investigate other methods of obtaining ramp coefficients.

Multiple-DAC Caliwave Method

The second method of obtaining ramp coefficients is the Multiple-DAC calibration pulse shape (caliwave) method [34]. The ramps obtained from this method are plotted as red triangles in figures 5.3 and 5.4. The advantage of this method over the parabola method is that it makes use of all the time samples at every delay setting. This method involves two steps: first, calibration pulse shapes, exactly like the ones in figure 5.5, are produced at each DAC setting for each channel. Recall these caliwaves are constructed from the 16 samples from all 25 delays to give a 400 ns pulse with 1 ns bins. Note that

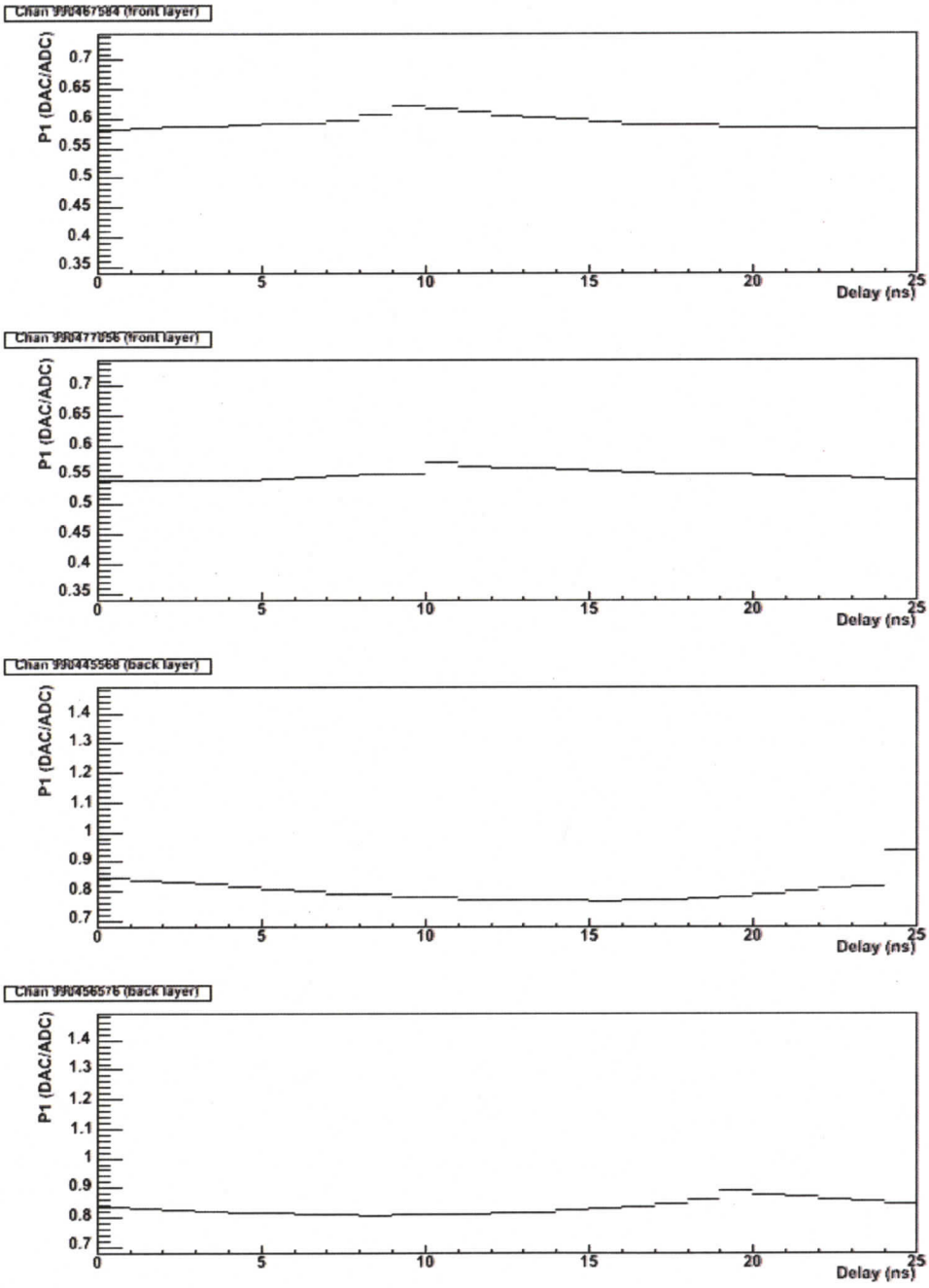

Figure 5.6: Linear ramp coefficient ($P1$) obtained from the parabolic interpolation method, plotted as a function of delay for four typical EMEC channels. The top (bottom) two plots are for channels in the front (back) layer of the EMEC. The parabolic method is shown to be biased because these curves are not flat.

when the calibration board pulses a channel at the lowest DAC setting, a measurement of the baseline signal is obtained. At each subsequent DAC setting, the samples have this small baseline signal subtracted off; the calibration equivalent of a pedestal subtraction. These caliwaves are then written into the database and are subsequently available to use in calibration signal reconstruction. Thus, every channel at each gain will have multiple caliwaves (one for each DAC) associated with it in the database, giving rise to this method's name.

The second step proceeds analogously to the parabolic method: for an injected calibration pulse in one channel at some gain and at some DAC, 16 samples (call them S_i) are taken of the resulting signal. However, rather than fitting a parabola to these 16 samples (with 25 ns spacing), the associated caliwave (with 1 ns bins) for this channel, gain, and DAC value is used to reconstruct the signal peak. The following statistic is computed for every delay setting:

$$\chi^2 = \sum_{i=0}^{4} (S_i - \lambda g_i)^2 \tag{5.5}$$

where S_i are the 5 largest consecutive samples (in ADC counts) of the 16 time samples of the calibration pulse, g_i are the corresponding 5 samples from one of the 25 sets of time samples that make up the caliwave, and λ is a scale factor to adjust the amplitude of the caliwave to match the amplitude of the time samples. Because this method uses the caliwave corresponding to the exact DAC setting of the injected pulse, no scaling

is required for the caliwave ($\lambda = 1$ for this method). By repeating this computation for all 25 delay settings (different g_i samples of the caliwave), the minimum χ^2 is found. This occurs when the g_i samples of the caliwave best match the S_i samples of the injected pulse. The peak of the calibration signal is found by using the caliwave (which has 1 ns resolution) rather than the original time samples of the signal which are 25 ns apart. By interpolating a parabolic fit to the three maximum samples of the caliwave, the maximum amplitude of the caliwave is obtained. Finally, the ADC_{peak} of the injected pulse is computed by multiplying the maximum amplitude[4] of the caliwave by λ. Repeating this method for all DACs in a calibration run, the calibration plot relating DAC to ADC is made for the channel and a quadratic fit yielding ramp coefficients is performed.

Using this method that makes use of all the delay settings of the caliwave to produce ramps eliminates the bias introduced by the choice of delay setting in the parabolic method. Figure 5.7 shows the same four EMEC channels as in figure 5.6. The spread in the ramp values across all the delays has been reduced to within 2%.

Although this method is an improvement over the parabolic method, it unfortunately has a problem with a few channels in medium gain. Referring back to the red, multi-DAC dataset in figure 5.4, several of the EMEC front layer channels (channel ID greater than 990461000) have ramps obtained from this method that deviate substantially from the trend set by all three of the other methods. It turns

[4]If the maximum of the parabolic interpolation of the caliwave peak and the maximum sample of the caliwave differ by more than 1 ADC count, the maximum sample is used as the peak amplitude.

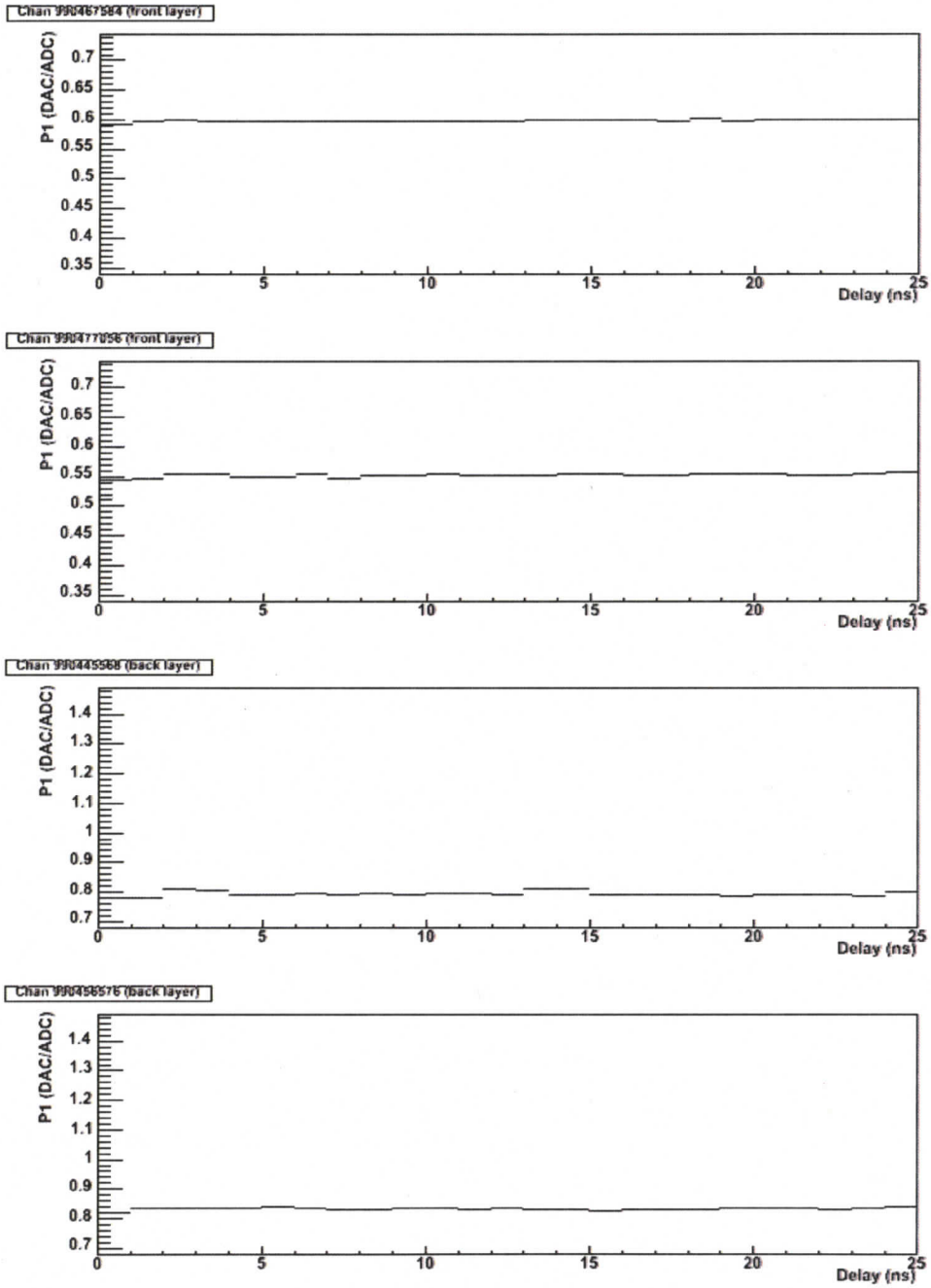

Figure 5.7: Linear ramp coefficient ($P1$) obtained from the calibration pulse shape method, plotted as a function of delay for four typical EMEC channels. The top (bottom) two plots are for channels in the front (back) layer of the EMEC.

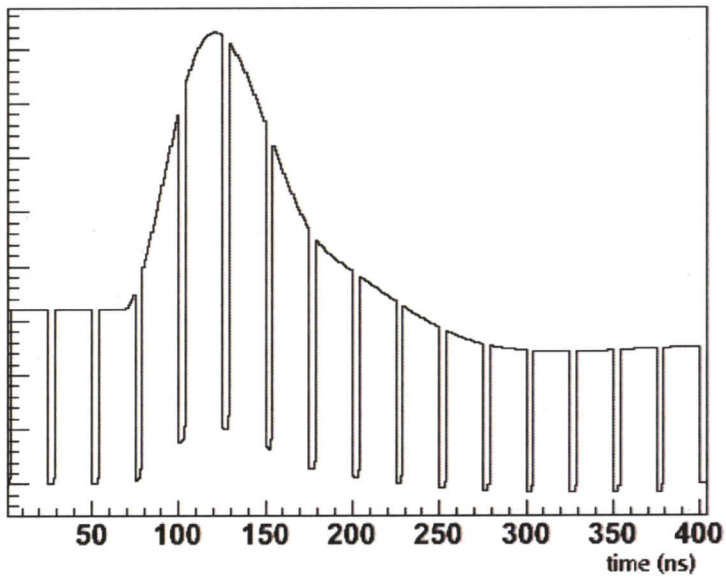

Figure 5.8: A sample calibration pulse shape for an EMEC channel at medium gain that is missing delay data.

out that the the calibration file is missing 3 to 4 different delay settings for half of the DAC range. Therefore, some of the calibration pulse shapes are missing some of the bins resulting in comb-like caliwaves. An example is given in figure 5.8. Using pulse shapes such as this in the peak reconstruction of the calibration data in turn affects the ramp fit to the calibration graph. Thus, the deviation from the trend in figure 5.4 for some of the EMEC channels is a result of using these incomplete pulse shapes. Therefore, a third method of producing ramp coefficients is needed.

Central-DAC Caliwave Method

The final method of obtaining ramp coefficients investigated is the central-DAC calibration pulse shape (caliwave) method. The ramps obtained from this method are

plotted as black triangles in figures 5.3 and 5.4. This method is very similar to the multiple-DAC caliwave method described above. The essential difference is that rather than using a different calibration pulse shape at each new DAC setting, only one calibration pulse shape (for each channel at each gain) is used for all DAC settings during the calibration run. The χ^2 statistic (equation 5.5) is still minimized, but in the central-DAC method λ is not equal to 1 in principle because the one caliwave used must be scaled to match the different amplitudes of the injected pulses in the calibration run. To obtain the formula for λ, the equation for the χ^2 (equation 5.5) is differentiated and set equal to zero for the delay setting that produces the minimum χ^2 value:

$$\frac{d\chi^2}{d\lambda} = 0 = \sum_{i=0}^{4}(-2S_i g_i + 2\lambda g_i^2). \tag{5.6}$$

Solving for λ gives:

$$\lambda = \frac{\sum_{i=0}^{4} S_i g_i}{\sum_{i=0}^{4} g_i^2}. \tag{5.7}$$

Notice that this equation reduces to $\lambda = 1$ in the case that the samples are for the same DAC setting as the caliwave used ($S_i = g_i$).

Thus, rather than requiring a caliwave for each channel at each gain for each DAC value in each running period, only one caliwave needs to be stored in the database for each channel at each gain in each running period. Furthermore, the caliwave selected is obtained for a DAC value near the center of the DAC range (avoiding the non-linear low end and any possible saturation occurring at the high

end), thus giving this method its name. Referring back to figure 5.2 we see the DAC range in high gain mode is from 0 to 1200 counts. For medium gain, the range is from 0 to 12000 counts. At high gain, the caliwave obtained at a DAC value of 550 is selected as the "master" caliwave to use for calibration pulse shape fitting. For medium gain it is the caliwave at 4500 DAC counts that is used.

The first advantage of this method is that it corrects the problem encountered in the multiple-DAC method at medium gain, where some DAC values did not have data for all the delay settings producing comb-like caliwaves. Comparing the ramps obtained with this method (black data points) to the ones from the multiple-DAC method (red) in figure 5.4, we see the erratic behaviour of the ramps in the front layer has been eliminated.

The second advantage of this method is that only one caliwave per channel per gain needs to be stored in the database. Memory consumption is not much of an issue during beam tests when there are only hundreds of channels; it will be an issue in ATLAS when there are hundreds of thousands of channels. Recording only one central-DAC caliwave in the database will reduce memory consumption compared to the multiple-DAC method.

Based on the above discussion, the ramp coefficients obtained from the central-DAC caliwave method are judged to be the best ramps for the 2004 testbeam, and are subsequently used in testbeam data reconstruction. The linear and quadratic ramp coefficients ($P1$ and $P2$) are the coefficients that are used in equations 5.1 and 5.2

for cell energy reconstruction.

Comparison With Previous Testbeam Ramps

The ramp coefficients used in the previous inner wheel testbeam are shown in figures 5.3 and 5.4 as open blue triangles. Considering the linear ramp coefficient $P1$ shown in the top plots in these figures, the sets of ramps (in both medium and high gain) agree well in the front layer of the EMEC IW. However, in the back layer channels, the previous EMEC IW linear ramp coefficients have values which are approximately 65% lower than the three sets of ramps computed during this testbeam. Because all channels are handled the same way by the software, the fact that the back layer channels disagree, but the front channels are in agreement, leads to the suspicion that the cause of the difference must be due to some difference in the experimental setup. The only known difference is that in the 2004 testbeam setup the EMEC uses slightly different motherboards than in the previous inner wheel testbeam experiments. According to the EMEC electrical experts this would cause small differences in capacitances, grounding schemes, and inductances, but nothing that would account for this 65% difference only in the back layer channels [36].

The quadratic ramp coefficients also show some differences in the back layer channels. The fact that the $P2$ coefficients in the 2004 testbeam are negative make up for some of the difference in the linear ramp coefficients (refer to equation 5.4). However, the linear ramps are so dominant that the quadratic terms only account for

a few percent of the difference.

Therefore, the source of the difference between the linear ramps is, at the time of writing, still unknown. Perhaps some unknown difference exists between the experimental setups that has not been taken into account. Any effect that this has on the response of the EMEC will be very difficult to observe because the back layer of the EMEC only sees approximately 5% of the energy of an electromagnetic shower; the majority of the energy is deposited in the front layer of the EMEC inner wheel. This is apparent in the response plots presented in the following chapter.

5.3 DAC to μA Conversion

The second sub-factor that is used in the computation of the cell energy is $DAC2\mu A$ shown in equations 5.1 and 5.2. It converts from DAC counts to electric current, and it is a constant factor for all channels in a given detector layer at all gains.

A schematic of the calibration and readout chain for one channel is given in figure 5.9. The calibration circuit for a channel consists of a calibration board which injects a voltage pulse down the calibration line, through the feedthrough (FT), and across a network of injection resistors on the motherboard in the cryostat. A single LAr detector channel is also shown in the schematic as a simple *RLC* circuit. The triangular ionization signal generated at the LAr gap level for any given channel follows the same readout chain as an exponential calibration signal down the readout

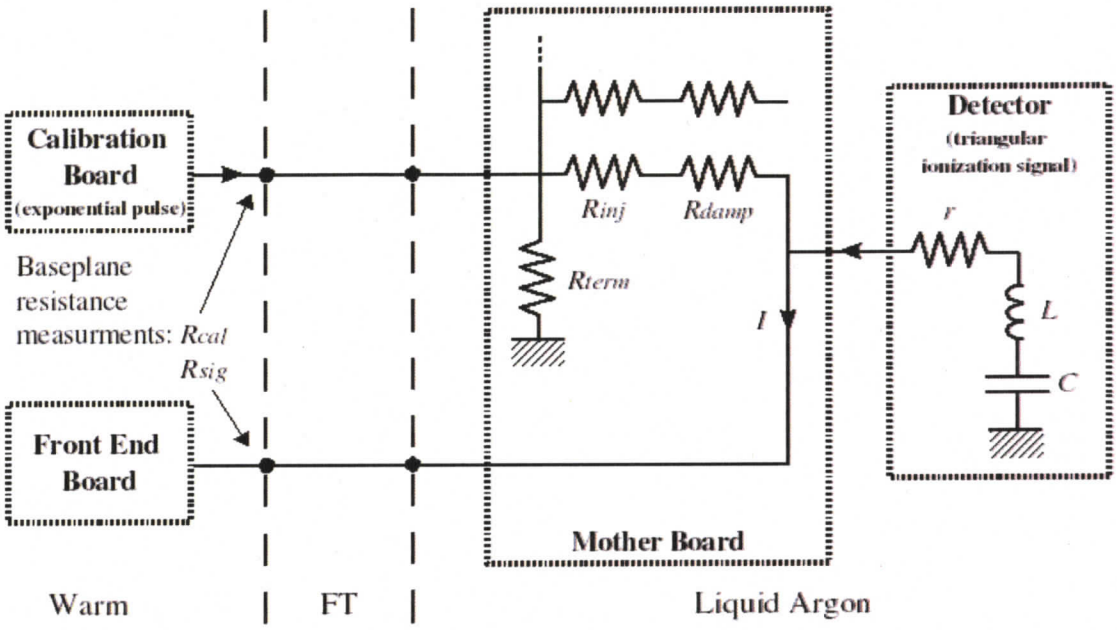

Figure 5.9: Schematic diagram of the calibration and readout chain. The calibration line is seen to pulse multiple channels. A single LAr detector channel is also shown. Both the exponential calibration pulse injected by the calibration board and an ionization signal from the LAr gap follow the same readout chain.

line to the front end board (FEB).

Each calibration line pulses eight channels, each with a resistance of $R_{\text{inj}} + R_{\text{damp}}$. Using Ohm's law ($I = V/R$), the $DAC2\mu A$ conversion factor in equations 5.1 and 5.2 that relates the injected pulse (in DAC counts) to current (in μA) is:

$$DAC2\mu A = \frac{5\text{V}}{(2^{17}-1)} \times \frac{1}{(R_{\text{inj}} + R_{\text{damp}})\Omega} \times \frac{10^6 \mu A}{1A}. \tag{5.8}$$

The nominal values for these resistors are given in [20] to be: $R_{\text{damp}} = 50\ \Omega$, and $R_{\text{inj}} = 450\ \Omega$ (945 Ω) for the front layer (back layer) of the EMEC inner wheel.

The values given are *cold* values, meaning the resistances quoted are at LAr temperature. It is also shown in this same reference that the cold resistor values are 2% larger than *warm* (room temperature) values. In previous IW beam tests that used the same calibration boards, the warm values are given to be: $R_{\text{inj}} + R_{\text{damp}} = 508.2\ \Omega$ ($1015.8\ \Omega$) for the front layer (back layer) [37]. Measurements of the resistors are expected to agree with these values.

The resistance values are extracted from two measurements [20]. The resistance measured at the front-end-crate (FEC) baseplane signal line output is:

$$R_{\text{sig}} = R_{\text{inj}} + R_{\text{damp}} + R_{\text{term}}, \tag{5.9}$$

(see figure 5.9). The resistance measured at the calibration line input pins with respect to ground when the FEB is disconnected is:

$$R_{\text{cal}} = R_{\text{term}}. \tag{5.10}$$

Based on these measured resistances we see that:

$$R_{\text{inj}} + R_{\text{damp}} = R_{\text{sig}} - R_{\text{cal}}. \tag{5.11}$$

The average channel resistances obtained from these measurements at room temperature are: $R_{\text{inj}} + R_{\text{damp}} = 507 \pm 1\ \Omega$ ($1015 \pm 0.5\ \Omega$) for the front layer (back layer) [32]. Shifting these numbers to cold values gives $517\ \Omega$ ($1035\ \Omega$), which are the values used

in the EMEC calibration for this study. Table 5.2 summarizes these different sets of

$(R_{\mathbf{inj}} + R_{\mathbf{damp}})$	Nominal (cold)	Previous IW testbeam	CBT-EC2 measured	CBT-EC2 (cold)
Front layer	500	508.2	507±1	517±1
Back layer	995	1015.8	1015±0.5	1035±0.5

Table 5.2: EMEC inner wheel calibration resistances (in Ω). All values are at room temperature unless indicated as cold—implying LAr temperature.

resistor values. Using the CBT-EC2 (cold) resistances in equation 5.8 gives

$$DAC2\mu A = 0.0738\ (0.0369)\ \mu\text{A/DAC} \tag{5.12}$$

for the front layer (back layer) of the EMEC inner wheel.

5.4 μA to MeV Conversion

The third contribution to the calibration coefficient (equations 5.1 and 5.2) is the electromagnetic scale factor (α_{EM}) that converts the current to the EM energy scale. It has units of MeV/μA, and is a constant factor for all EMEC cells at all gains. In the previous IW testbeam a value of $\alpha_{\text{EM}} = 526$ MeV/μA was used [37].

In the current testbeam, this parameter is determined from an analysis of the beam test data. A study is performed where cells illuminated by an electron beam are reconstructed and analyzed in units of μA as opposed to being converted to the EM scale. The ratio of the known beam energy (in MeV) to the response (in

μA) of an electromagnetic shower contained in the EMEC is α_{EM}. This procedure is discussed in the following chapter in section 6.4.1. The calculation performed is only preliminary because the current testbeam data still require a high voltage dependent correction to be applied (see section 5.6). Therefore, the calculation is performed with the intention of verifying the value obtained from the previous testbeam. The results presented in section 6.4.1 support using $\alpha_{\mathrm{EM}} = 526$ MeV/μA in this testbeam.

5.5 Calibration Signal to Physics Signal correction

Ideally, one would want the calibration pulse to be identical to the physics pulse, and be injected at the actual readout electrode (pad). This would ensure that the calibration pulse goes through the same circuitry as an ionization (physics) signal and would create an equivalent signal. The accordion geometry in the EMEC, which allows for full ϕ hermetic coverage, prevents the calibration pulse from being injected right at the readout pad. Moreover, the EMEC calibration board injects an exponential pulse. Thus, there are two factors that cause a difference between the calibration signal and a physics signal: the calibration pulse injected to the EMEC by the calibration board is not at the LAr gap level, and the injected pulse is exponential which is slightly different than the triangular physics ionization signal (see figure 5.1) that comes from the LAr gap level. Figure 5.10 illustrates the effect of this difference: the response to the triangular ionization current will be slightly higher than the response to an

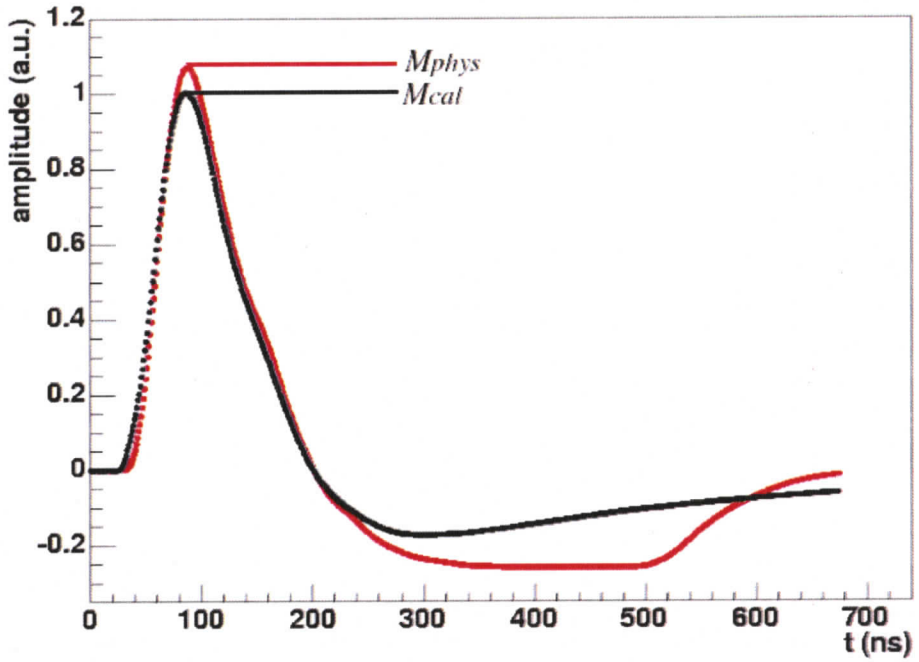

Figure 5.10: Pulse shape response of the EM calorimeter to a physics signal (red line) and a calibration signal (black line) of the same initial current [34].

exponential calibration pulse of the same initial current amplitude. The ratio of the pulse shape amplitudes, $M_{\text{phys}}/M_{\text{cal}}$, is a needed correction factor. It is the inverse of this factor which is applied, channel by channel, to correct the ramp coefficients (the first terms in equations 5.1 and 5.2), that were obtained with calibration signals, to the appropriate scale of a physics signal.

For the back layer of the EMEC inner wheel the average value of $M_{\text{phys}}/M_{\text{cal}}$ is 1.06 with roughly $\pm 2\%$ variation across the channels, and in the front layer the value is 1.17 with roughly $\pm 3.5\%$ variation across the channels [38].

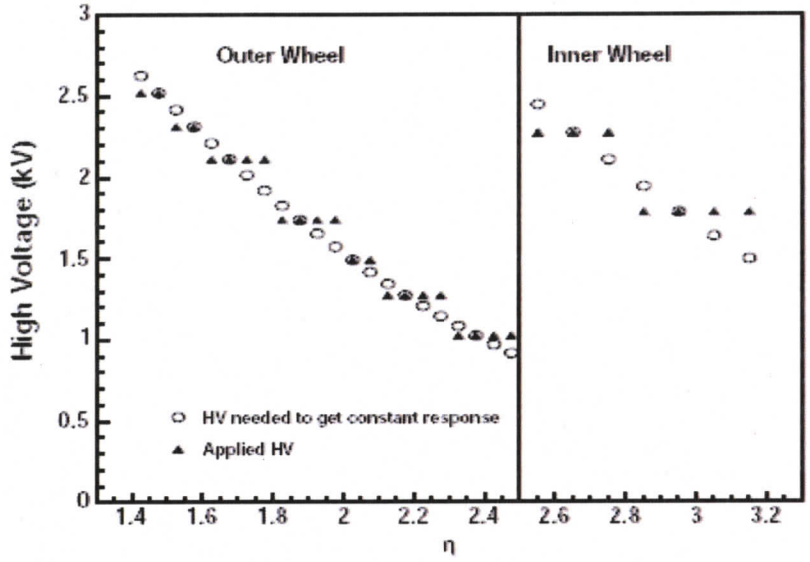

Figure 5.11: High voltage variation along η in the EMEC [39]. The open circles are the voltages producing a uniform response, and the solid triangles are the actual applied voltages.

5.6 EMEC HV-dependent correction

As discussed earlier, the accordion geometry of the ATLAS electromagnetic calorimeters is unique. It is fully symmetric in ϕ and doesn't have any cracks between modules as in a more traditional sampling calorimeter geometry, such as the HEC. Based on this geometry, the LAr gap smoothly increases as you move outward from the center line (decreasing η) of the EMEC. In order to keep a uniform detector response and electron drift time, the HV across the gap must also increase with decreasing η. However, for technical reasons [20] the applied HV only changes in steps. This can be seen in figure 5.11 where the solid triangles show the step-wise nature of the applied voltage, whereas the open circles show what the HV would be for a uniform calorimeter

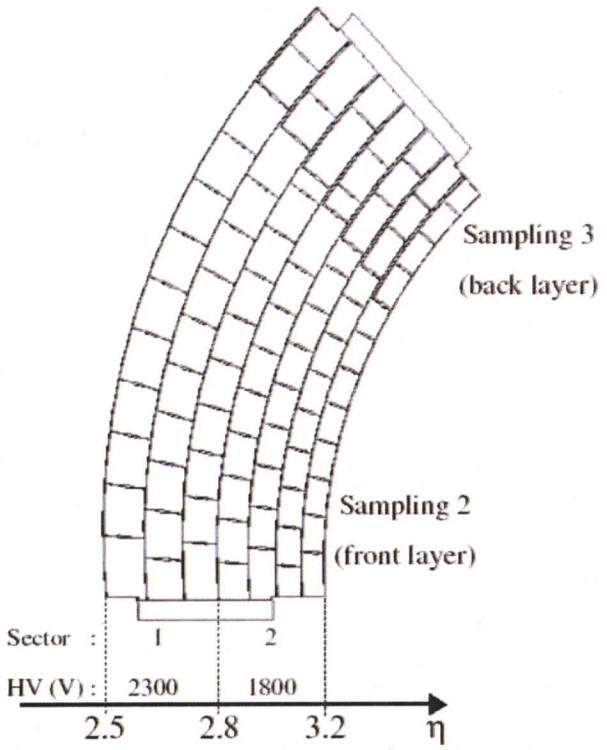

Figure 5.12: Schematic view of a flat inner wheel electrode showing the two HV sectors.

response. This leads to a residual η-dependent effect in the actual detector response which requires a correction factor.

In the inner wheel there are only two HV sectors, as shown in figures 5.11 and 5.12. The first HV sector is from η= 2.5 to 2.8, and the second is from η=2.8 to 3.2. The correction will have to be applied cell by cell, and it will be different for each HV sector in the detector. The following η-dependent weights are applied to the

energy of each cell in each high voltage sector:

$$w_{1,2}(\eta_{\text{cell}}) = \beta_{1,2}(1 + \alpha_{1,2}(\eta_{\text{cell}} - \eta_{1,2})) \tag{5.13}$$

where $\eta_{1,2}$ are the η positions of the center of the two HV sectors in the EMEC inner wheel, and η_{cell} is the location of the middle of the cell.

The determination of these factors is beyond the scope of this thesis. At the time of writing, these factors have not yet been determined from the testbeam data by the CBT-EC2 collaboration. However, it is known from previous beam tests in the inner wheel that this correction is non-negligible: before the corrections are applied, the variation of detector response within a single HV sector is approximately 12% [40]. Applying the corrections brings the response within a few percent across both HV sectors. Further details of this correction can be found in references [39, 40, 41].

In summary, this chapter demonstrated the need for a cell level calibration of the LAr calorimeters, specifically the EMEC, and explained how the calibration coefficients are used in the calorimeter cell energy computation (equation 5.4). Each coefficient was discussed in turn, along with the two additional corrections that are needed. In the discussion of the ramp coefficients, a study comparing three methods for obtaining the ramps was given. The Central-DAC calibration pulse shape method was seen to be the most reliable method for obtaining the ramp coefficients for the EMEC.

Chapter 6

Calorimeter Energy Response

One of the main objectives of the 2004 beam tests of the end-cap calorimeters is to study the energy reconstruction across the transition region between the different calorimeter modules. This chapter presents the response and resolution of the calorimeter modules exposed to particle beams.

6.1 Clustering Algorithms

When an incident beam particle ($e^{\pm}, \pi^{\pm}$) impacts the detector, energy is deposited in the calorimeter cells via electromagnetic and hadronic showers. Once the signal in each calorimeter cell is obtained (chapter 4) and is converted to the EM energy scale (chapter 5), the overall event energy can be reconstructed. One approach would be to add up the energy contained in every calorimeter cell yielding the maximum amount of signal for an event. Only energy that has leaked out the sides or back of the

calorimeter would be missed in this approach. However, the signal from each cell will have electronic noise even if no energy is deposited in the cell. By including all cells, the reconstructed event energy contains the maximum amount of electronic noise which therefore degrades the resolution[1]. When dealing with thousands of cells in ATLAS, as opposed to the 698 cells in this testbeam, this approach is also impractical for computational reasons.

Ideally, only cells that contain deposited energy would be used to reconstruct the event energy. In practice, various schemes are used to select cells where energy is expected to be deposited. The selected cells are known collectively as *clusters*. This approach reduces the amount of noise included in the energy reconstruction, improving the resolution, but at risk of biasing the energy measurement by possibly missing some small amount of signal that is legitimately deposited in cells not included in the cluster. An established clustering algorithm in ATLAS for LAr cells is a topological clustering method [18] where clusters are built out of cells following a nearest neighbour approach. Cells are grouped into clusters based on the comparison of a given cell's signal-to-noise ratio ($|E|/\sigma_{\text{noise}}$) to three different signal over noise thresholds: "seed" threshold, "neighbour" threshold, and "other" threshold. The values of these three thresholds can be changed in order to produce different sized clusters.

[1]The resolution is a measure of the uncertainty in the energy reconstruction. A run with thousands of events will result in a Gaussian distribution of event energies. The resolution is the ratio of the width (σ) to the mean reconstructed energy (E_{reco}) of a Gaussian fit to the energy distribution.

In this analysis, clusters are initiated by cells that have $|E|/\sigma_{\text{noise}} > 4$, and are called "seed" cells. Any seed cells topologically connected to another seed cell (i.e. touching through cell faces, corners, or edges) are merged into a single cluster.

The second threshold is the "neighbour" threshold. Any cells that are topologically connected to the initial seed cells and have a ratio $|E|/\sigma_{\text{noise}} > 2$ are called "neighbour" cells and are added to the cluster. This is an iterative process where any cells that pass the neighbour threshold, and are topologically connected to the neighbour cells added in the previous iteration, are also included in the cluster. This continues until no new neighbour cells are added. If two or more clusters share a neighbour cell the clusters are merged [13].

Finally, the "other" threshold adds a layer of cells around a cluster. "Other" cells are included in the cluster if they are topologically connected to the cluster and have a ratio $|E|/\sigma_{\text{noise}} > 0$. This threshold, in other words, pads the cluster by adding a one-cell halo around the cluster where possible. Thus, in this thesis, the seed, neighbour, and other clustering thresholds are 4, 2, and 0 respectively. This level of clustering is conveniently referred to as "T420", indicating that the clustering is topological (T) with the three required thresholds indicated.

The topological clustering method also provides three possible levels of cluster growth by allowing clusters to form only within one calorimeter layer, within entire calorimeters, or across different calorimeters. The established approach in ATLAS is to allow cluster growth across the different calorimeters (called "super3D" clustering).

This choice is in line with the goal of studying energy reconstruction in the crack regions between the EMEC, HEC, and FCAL end-cap calorimeters where shower energy is naturally deposited in all three calorimeters.

6.2 Event Selection

The energy clustering is computed for each event in a run, and recall that each run consists of several thousand events. As mentioned in section 4.1, an analysis of the signals from beam detectors is used to reduce undesirable events. This includes halo beam particles outside the nominal beam trajectory, multiple particle events, and muons contaminating the electron, positron, and pion beams used in this study.

Electron and positron beams contain some residual muon and pion contamination. Electrons and positrons deposit their energy through EM showers which are fully contained in the electromagnetic calorimeters (EMEC, FCAL1). Pions deposit their energy through hadronic showers resulting in responses that have a larger fraction of their energy deposited in the hadronic calorimeters (HEC, FCAL2). Muons pass through the calorimeters depositing only a small fraction of their energy before exiting out the back of the modules. Thus, the energy response in the calorimeters depends on the particle type.

For electron beams, the following selection cut based on the location of de-

posited energy is applied: the event is accepted if

$$\frac{|E_{\text{hadronic}}|}{|E_{\text{em}}|} < 0.07, \tag{6.1}$$

where E_{hadronic} is the cluster energy in the HEC and FCAL2 and E_{em} is the cluster energy in the EMEC and FCAL1. The effect of this cut can be seen in figures 6.1 and 6.2 where the data before the cut are shown in black, and the data surviving after the cut are green. Figure 6.1 shows a scatter plot (top) illustrating how the cluster energy is shared between the electromagnetic and hadronic calorimeters, along with the total cluster energy distribution (bottom) to a 120 GeV positron run at impact point B in the EMEC. Figure 6.2 shows same two plots for a 120 GeV positron run at impact point H in the FCAL. The three types of particles (e^+, π^+, μ^+) are evident in the energy response of the calorimeters (black data). These figures indicate that the muon and pion contamination in a run is approximately 25%, of which less than 0.5% on average are muons[2]. This ratio cut clearly reduces[3] the beam contamination, and is used for all $e^\pm$ runs. The events that survive this cut (green data) are then used for further analysis.

In pion runs, the contaminating particles are leptons ($\mu^\pm$ and $e^\pm$). A ratio cut based on hadronic and EM energy cannot be used for pions because hadronic

[2]Recall that muons have already been eliminated by using the muon scintillators located behind the cryostat.

[3]Some pion contamination remains underneath the electron peak. A study performed on a previous testbeam estimates the remaining pion contamination to be ≈0.1% [12].

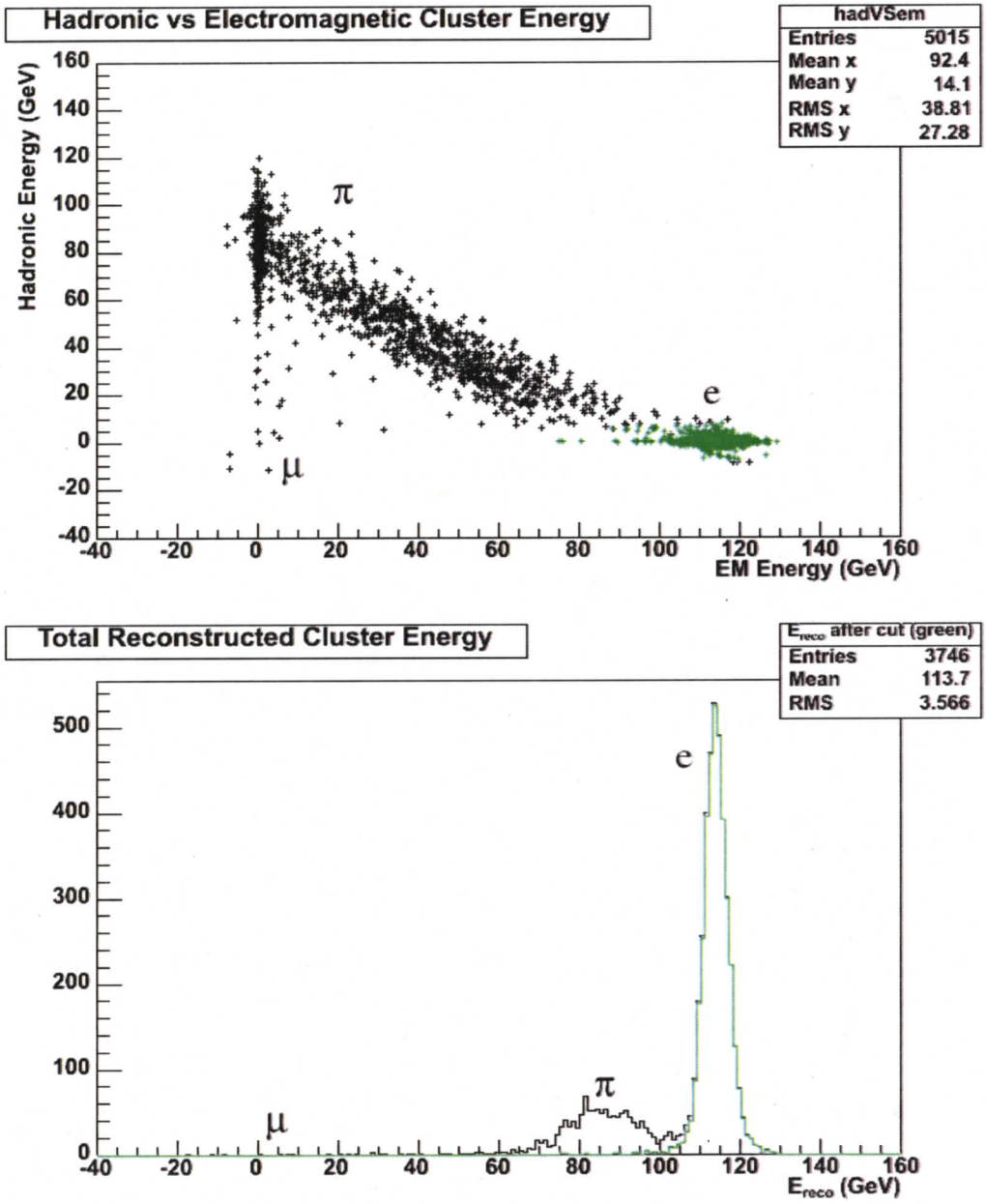

Figure 6.1: Histograms of the energy response of the calorimeters to a 120 GeV e^+ beam at impact point B in the EMEC. The top two dimensional histogram shows cluster energy in the hadronic calorimeters (HEC, FCAL2) plotted against the cluster energy in the EM calorimeters (EMEC, FCAL1). The bottom plot is a histogram of the total cluster energy. Both plots show the data before the cut (equation 6.1) in black, and the remaining data after the cut in green.

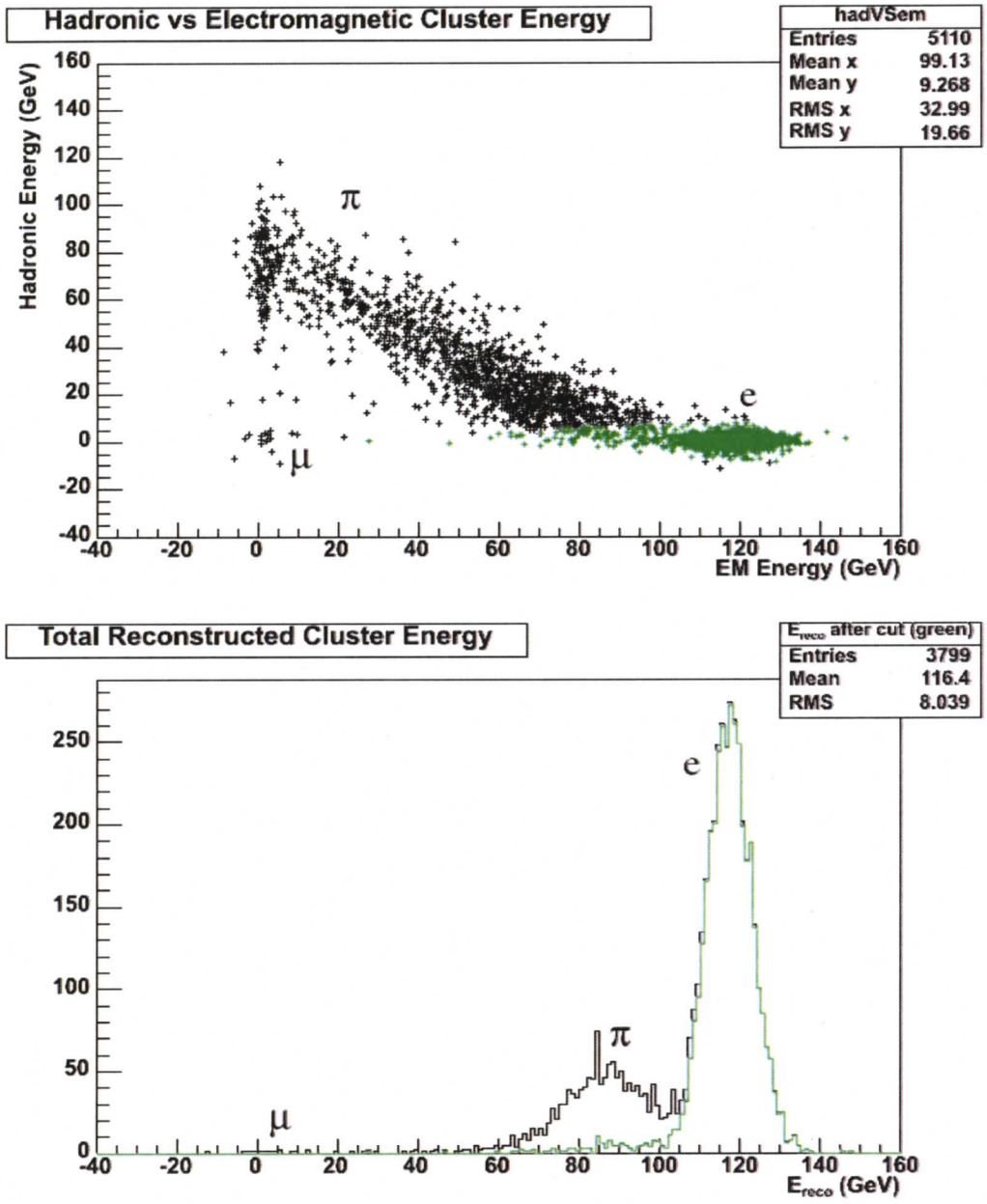

Figure 6.2: Histograms of the energy response of the calorimeters to a 120 GeV e^+ beam at impact point H in the FCAL. The top two dimensional histogram shows cluster energy in the hadronic calorimeters (HEC, FCAL2) plotted against the cluster energy in the EM calorimeters (EMEC, FCAL1). The bottom plot is a histogram of the total cluster energy. Both plots show the data before the cut (equation 6.1) in black, and the remaining data after the cut in green.

showers naturally have an electromagnetic component. While the amount of the EM component will fluctuate event by event, any cut based on EM energy attempting to remove the electrons/positrons will remove legitimate pion events also. Therefore, the only cut applied for pion runs is one to remove muon contamination. Events are accepted if the total reconstructed cluster energy is greater than 20 GeV. This removes less than 1% of the events in the pion runs.

6.3 Calorimeter y-Scans

A data run is a collection of thousands of events of one particle type and energy at one impact point. A *y-scan* is a collection of runs with impact positions incremented systematically to different y values for a fixed x position. The calorimeters are exposed to particle beams of different beam energies and particle types. The response of the electromagnetic calorimeters (EMEC and FCAL1) can be probed with electrons and positrons, and pions are used to probe all calorimeters. Figure 6.3 is an enlarged version of the central region of figure 3.7 showing the front face of the testbeam calorimeter modules during period 2, and the red lines are the projection of the vertical y-scans studied here[4]. The central y-scan occurs at $x = 0$ mm, and the vertical scan to the left of it occurs at $x = -120$ mm. Both beam paths start at the top of the EMEC at a nominal position of $y = 210$ mm ($|\eta| \simeq 2.55$), cross the

[4]Some x-scans were also taken during data acquisition (see figure 6.3). Horizontal position scans are useful for studying response within individual detectors because the response on either side of $x = 0$ mm should be symmetric. No x-scans were performed in the transition region around $\eta = 3.2$.

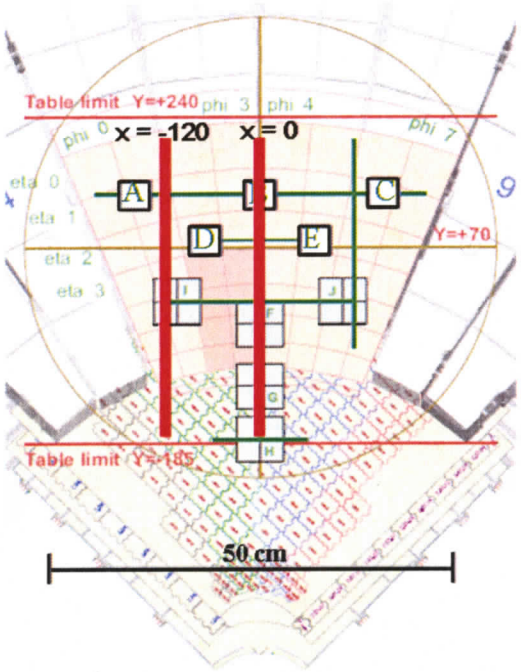

Figure 6.3: Front view of the central region of the testbeam modules during period 2, illustrating the standard impact points and the x and y beam paths. The red vertical lines at $x = 0$ mm and $x = -120$ mm are the y-scan paths used in this study.

transition region between the calorimeters, and extend into the FCAL finishing at $y = -184$ mm ($|\eta| \simeq 3.9$). The impact points along the y-scan paths have a nominal separation of $\Delta y = 30$ mm. Additional runs are added to the y-scan if they are of the same particle type and energy, and impact the detector at a position between planned positions. Electron, positron, and pion beams with energies ranging from 60 GeV to 200 GeV are used. Tables 6.1 and 6.2 summarize the particle type, energy, position, and run numbers of the data used. When possible, multiple runs at one impact point are used together in order to improve statistical precision. As mentioned in section 3.3, all runs used in the y-scans are from the second running period.

Vertical Scans with Electron/Positron Beams				
	y-scans at $x = 0$ mm			y-scan at $x = -120$ mm
y position (mm)	193 GeV e^- Runs	120 GeV e^+ Runs	60 GeV e^+ Runs	60 GeV e^+ Runs
210	2460–2462	1375–1376	2852–2853 2855	2851
180	2457–2459	1373	2854 2856–2857	2849
150	2454–2456	1371	2858–2859	2847
140	n/a	4007–4008	4289–4290	n/a
120	2451–2453	1369	2860–2861	2844–2845
90	2448–2450	1367	2862–2863	2842–2843
60	2445–2447	1365	2864–2865	2840–2841
30	2441–2443	1363	2866–2867	2839
0	2438–2439	1361	2868–2869	2836–2837
-30	2434–2436	1359 4009–4010	2870–2871 4291–4292	2834–2835
-60	2430–2432	1357	2873–2874	2833
-90	2427–2429	1355	2876–2877	2829
-110	2414–2416	4011–4012	4294–4295	n/a
-120	2424–2426	1353	2878–2879	2827
-150	2421–2423	1351	2880	2826
-180	2417–2419	4014–4015	2882–2883 4297–4298	2825
-184	n/a	1349	n/a	n/a
Runs	44	23	37	19
Events	182956	55016	232446	120416

Table 6.1: Data run numbers used in $e^{\pm}$ particle beam y-scans for studying the response of the three end-cap calorimeters. The bottom two rows give the total number of runs and events per y-scan.

Vertical Scans with Pion Beams			
	y-scans at $x = 0$ mm		
y position (mm)	200 GeV π^- Runs	120 GeV π^- Runs	60 GeV π^+ Runs
210	1458–1462	2116–2120	2720–2724
180	1452–1456	2110–2111 2113–2115	2715–2719
150	1446 1448–1450	2105–2109	2710–2714
140	3790–3794	2035–2039	n/a
120	1445	2100–2104	2705–2709
90	1434–1435	2095–2099	2700–2704
80	n/a	n/a	3446–3447 3450
60	1429–1433	2089–2093	2669–2673
30	1424–1428	2083–2087	2664–2668
0	1419–1420 1422–1423	2029–2033	2659–2663 3364–3368
-30	1414–1418 3796–3802	2023–2027 2068–2072	2654–2658 3359–3362
-60	1409 1411–1413	2017–2021	2649–2653
-90	1404–1408	2011–2015	2639–2643
-110	3806–3810	2073–2077	2644–2647 3537–3541
-120	1399–1403	2005–2007 2009	2636–2638
-150	1394–1398	1999–2003	2629–2635
-180	3812–3813 3815 3817	1992–1996	2624–2626 3487–3491
-184	1388–1391 1393	n/a	n/a
Runs	79	84	95
Events	804187	967717	940409

Table 6.2: Data run numbers used in $\pi^{\pm}$ particle beam y-scans for studying the response of the three end-cap calorimeters. The bottom two rows give the total number of runs and events per y-scan.

6.4 Electron/Positron y-Scan Results

As table 6.1 indicates, four y-scans with electron/positron beams are considered. The first three y-scans are all at the same position ($x = 0$ mm), but with energies of 193 GeV, 120 GeV, and 60 GeV. This allows for calorimeter response at different energies to be studied. The fourth y-scan is also at 60 GeV, but is at a position of $x = -120$ mm. Comparison between the two 60 GeV y-scans at different positions provides an opportunity to study the effect of position on calorimeter energy response.

These position scans are made up of runs taken at up to 17 different impact positions. At each position, a histogram of the reconstructed event energies is obtained (after the event selections have been performed). An example of such a histogram has already been shown as the green data in the bottom plot of figure 6.1. The mean reconstructed cluster energy for a run is obtained by iteratively fitting a Gaussian function to the energy distribution. This is a two step procedure: in the initial step, a Gaussian function is fitted to the distribution over a limited energy range of $E_0 \pm 30$ GeV, where E_0 is the energy of the bin with the maximum number of events. The initial fit returns the average (E_1) and the width (σ_1). The second step fits a Gaussian in the range $E_1 \pm 2\sigma_1$. The mean value of the second fit is called E_{reco} and represents the average reconstructed event energy. The calorimeter response is the ratio of E_{reco} over the nominal beam energy E_{beam}. Using the width of the second fit (σ), the resolution is calculated as σ/E_{reco}, and is a measure of the uncertainty in

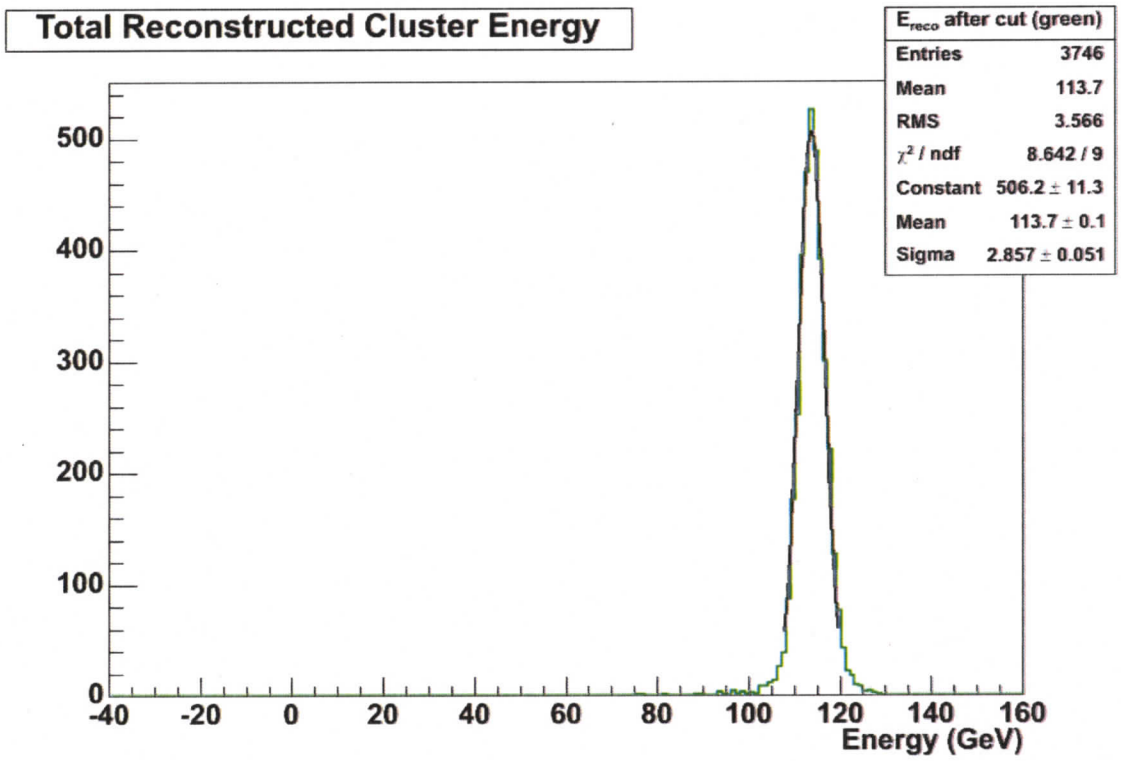

Figure 6.4: Gaussian fit to the reconstructed cluster energy distribution (after all event selection cuts are made) of a 120 GeV e^+ beam at impact point B in the EMEC.

the energy reconstruction. Using the same data as in figure 6.1, figure 6.4 shows the resulting Gaussian fit to the energy distribution. This iterative fitting procedure is used for all runs in the y-scans.

The iterative approach is somewhat redundant in such a clean example as figure 6.4 where the impact point is well within the EMEC and far from any module edges; a single Gaussian fit would be sufficient. However, the iterative procedure is more precise for runs impacting the transition region between the EMEC and FCAL where energy is deposited in the different calorimeters as well as in the dead

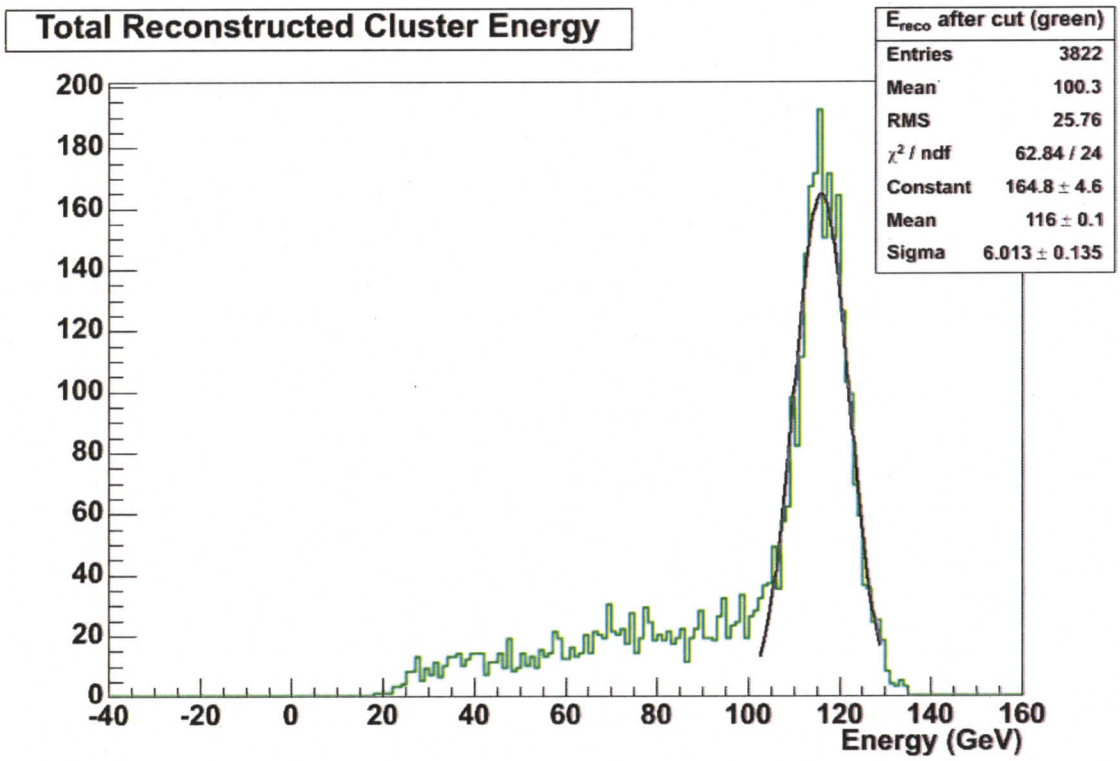

Figure 6.5: Gaussian fit to the reconstructed cluster energy distribution (after all event selection cuts are made) of a 120 GeV e^+ beam at impact point G (near the EMEC/cone/FCAL transition region).

material. As an example, the reconstructed cluster energy distribution for a 120 GeV e^+ run at impact point G ($|\eta| \approx 3.55$) is given in figure 6.5. The large peak near the nominal beam energy represents events that passed through the LAr excluder in front of the FCAL and showered predominately in the FCAL. The low energy tail of this distribution is made up of events that interacted with the dead material (cone and the LAr layer between the EMEC and the FCAL) reducing the shower energy measured in the FCAL. The mean energy of the distribution is therefore lower than the peak of the distribution. Thus, the iterative approach described above minimizes the effect

of the dead material on the resolution of the entire y-scan, but it underestimates the resolution near the transition region ($3.1 < |\eta| < 3.6$).

In order to study the response and resolution of the calorimeters, a position coordinate is needed. Using the nominal y-position coordinate is not sufficient because there are event-by-event variations in the impact position of the particles due to the finite beam size. Alternatively, the beam detectors could be used to compute a particle track and, therefore, an event specific y-position can be extrapolated. Unfortunately, software data objects needed for this approach are unavailable at the time of writing in the analysis framework used.

Although impact positions can be obtained by using beam detectors in test-beam experiments, ATLAS does not have any tracking capabilities at this pseudo-rapidity region. Therefore, any in situ calibration of ATLAS requiring position information in this η region will only have the calorimeters to use [42]. The analysis approach in this thesis uses the pseudorapidity of the energy clusters as an event-by-event y-position. The topological clustering method computes the center of the cluster, in terms of η and ϕ, using the energy-weighted average of the cell centers.

For each y-scan, the calorimeter response ($E_{\text{reco}}/E_{\text{beam}}$) and resolution ($\sigma/E_{\text{reco}}$) are plotted as a function of mean cluster pseudorapidity in figure 6.6. Recall that the y-scans start near the top of the EMEC at $|\eta| \approx 2.5$, continue downward through the transition (crack) region at $|\eta| = 3.2$, and finish in the FCAL near $|\eta| \approx 3.7$ (see figure 6.3). These different regions are evident in the response and resolution plots.

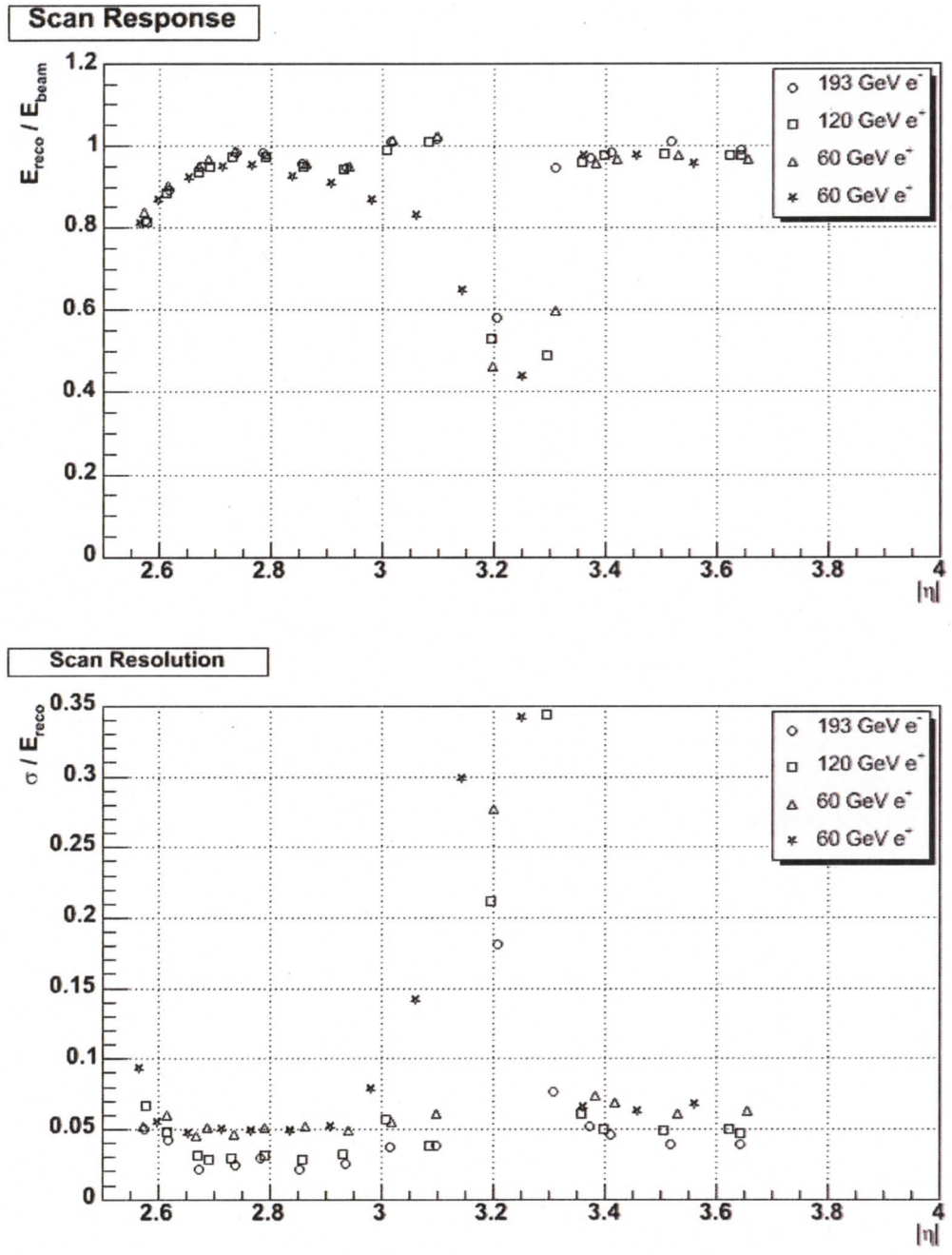

Figure 6.6: Calorimeter response (top) and resolution (bottom) as a function of cluster pseudorapidity to electron and positron beam vertical scans. The first three y-scans all occur at $x = 0$ mm. The fourth y-scan (star) occurs at $x = -120$ mm. The EMEC module extends from $2.5 < |\eta| < 3.2$, and the FCAL extends from $3.1 < |\eta| < 4.9$.

Response

Because all EM shower energy is in principle observable, the ideal response of the calorimeters to electron and positron beam y-scans is unity ($E_{\text{reco}}/E_{\text{beam}} = 1$) across the full pseudorapidity range. The response in the FCAL region is indeed flat in pseudorapidity and within a few percent of unity. Furthermore, the response is constant across the energy range considered (60 GeV to 193 GeV).

The response of the EMEC region ($2.5 < |\eta| < 3.2$) is more complex. Recall the discussion in section 5.6 regarding the need for a high voltage correction to be applied to the EMEC cells. Although the EMEC LAr gap is smoothly changing with pseudorapidity, there are only two fixed HV sectors (separated at $|\eta| = 2.8$) providing the electric fields across the LAr gaps. As previously mentioned, this cell-level correction is not currently known or implemented in the analysis of testbeam data, and the response in this η region in figure 6.6 reflects the fact that the EMEC HV correction has not been applied. The response varies by ~15% in the first HV sector ($2.5 < |\eta| < 2.8$), and by ~10% in the second HV sector ($2.8 < |\eta| < 3.2$). This is in agreement with the expected response variation within a single HV sector of approximately 12% noted earlier [40]. In spite of this variation of response with pseudorapidity, the response is consistent across the energy range of the y-scans. The only deviation from this trend is the 60 GeV positron y-scan at $x = -120$ mm, where the response drops off between $|\eta| = 2.8$ and 3.2. Two possible sources for

the declining response with η are leakage out the side of the module (which is then missed in the topological clustering), and increased dead-material (such as the EMEC support structure) near the edges of the module.

The response in the transition region at $|\eta| \approx 3.2$ is seen to be substantially reduced[5]. The 40-55% drop in response in this region requires further investigation, preferably by a method that allows for a more continuous picture of the calorimeter response rather than such a discrete view (where one or two data points per y-scan are available in this region). Furthermore, viewing the calorimeter cluster energy response of the different detector samplings (layers) illustrates where the energy is being deposited in the calorimeters. The pseudorapidity range $2.5 < |\eta| < 4.0$ is divided into 200 equal bins, and the events in the y-scan (regardless of what run they are in) are binned according to the event cluster pseudorapidity. This provides a more finely-binned picture of the y-scan. The response is then computed as the mean reconstructed energy of the events in each bin divided by the nominal beam energy.

The continuous energy response distributions are given in figures 6.7 and 6.8, where the discrete data points (same data as in figure 6.6) are over-plotted for a reference[6]. The average total cluster energy is shown as the green line in the plots,

[5]Recall that this is not a smooth transition from one detector to another because of presence of the FCAL cone and a layer of uninstrumented LAr between the EMEC and the cone (see figure 3.2).

[6]Note that the discrete data points are in good agreement with the continuous response (green line) away from the transition region. Specifically, near $|\eta| \approx 3.3$ to 3.4 the response differs by $\sim$10% in all y-scans. This is understood by recalling that the discrete data points represent the response for all runs at a given impact point, and the value is obtain by iteratively fitting a Gaussian to the energy distribution. The continuous plot, on the other hand, is the mean energy of the events within each η bin. A clear illustration of this difference was given in figure 6.5 where the mean of the distribution is 13.5% lower than the mean of the fit.

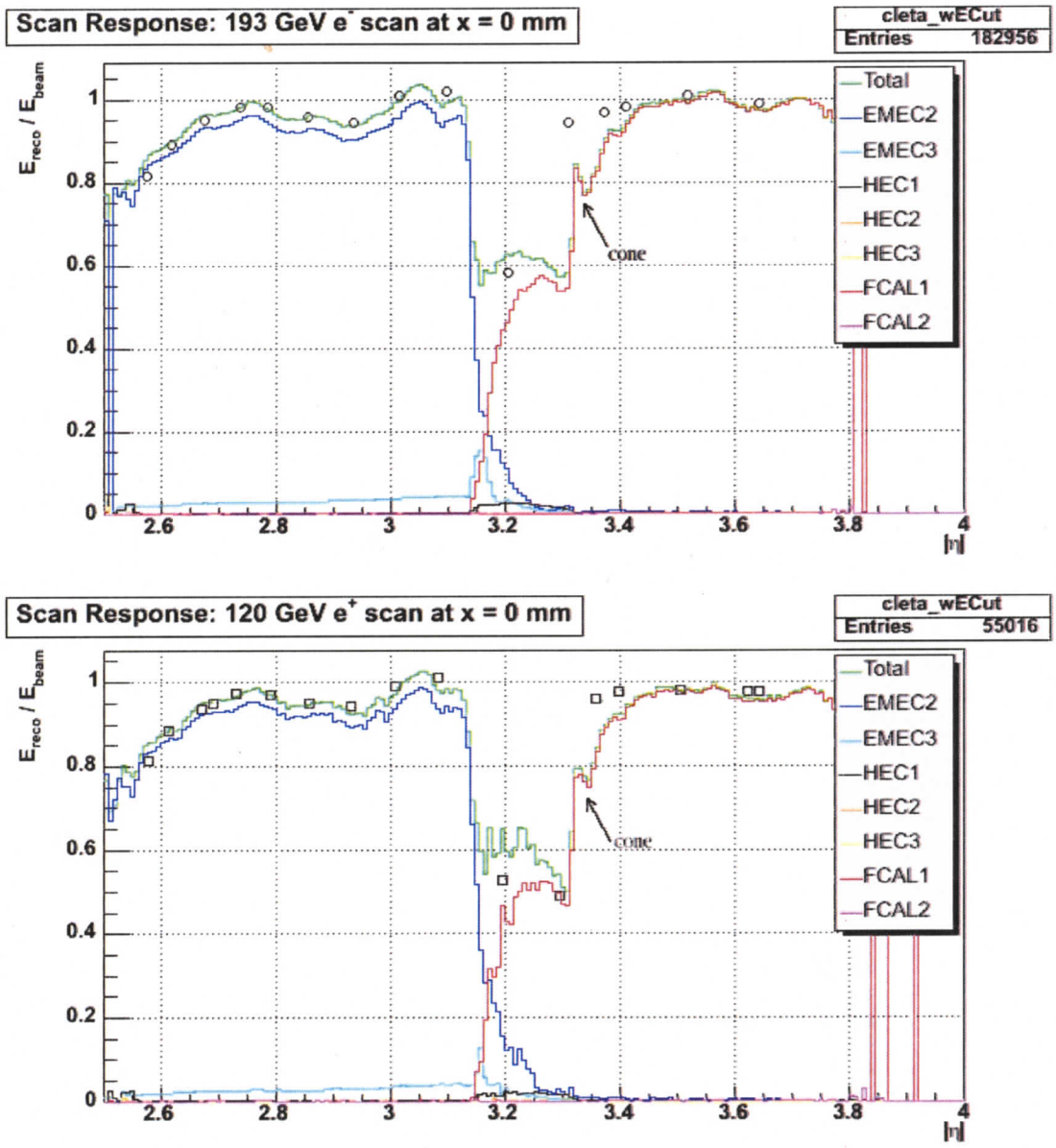

Figure 6.7: Calorimeter response to the 193 GeV electron y-scan (top) and the 120 GeV positron y-scan (bottom) as a function of mean cluster pseudorapidity. The total cluster energy is shown (green), along with the cluster energy in each sampling layer. The data points are the energy response at the impact points.

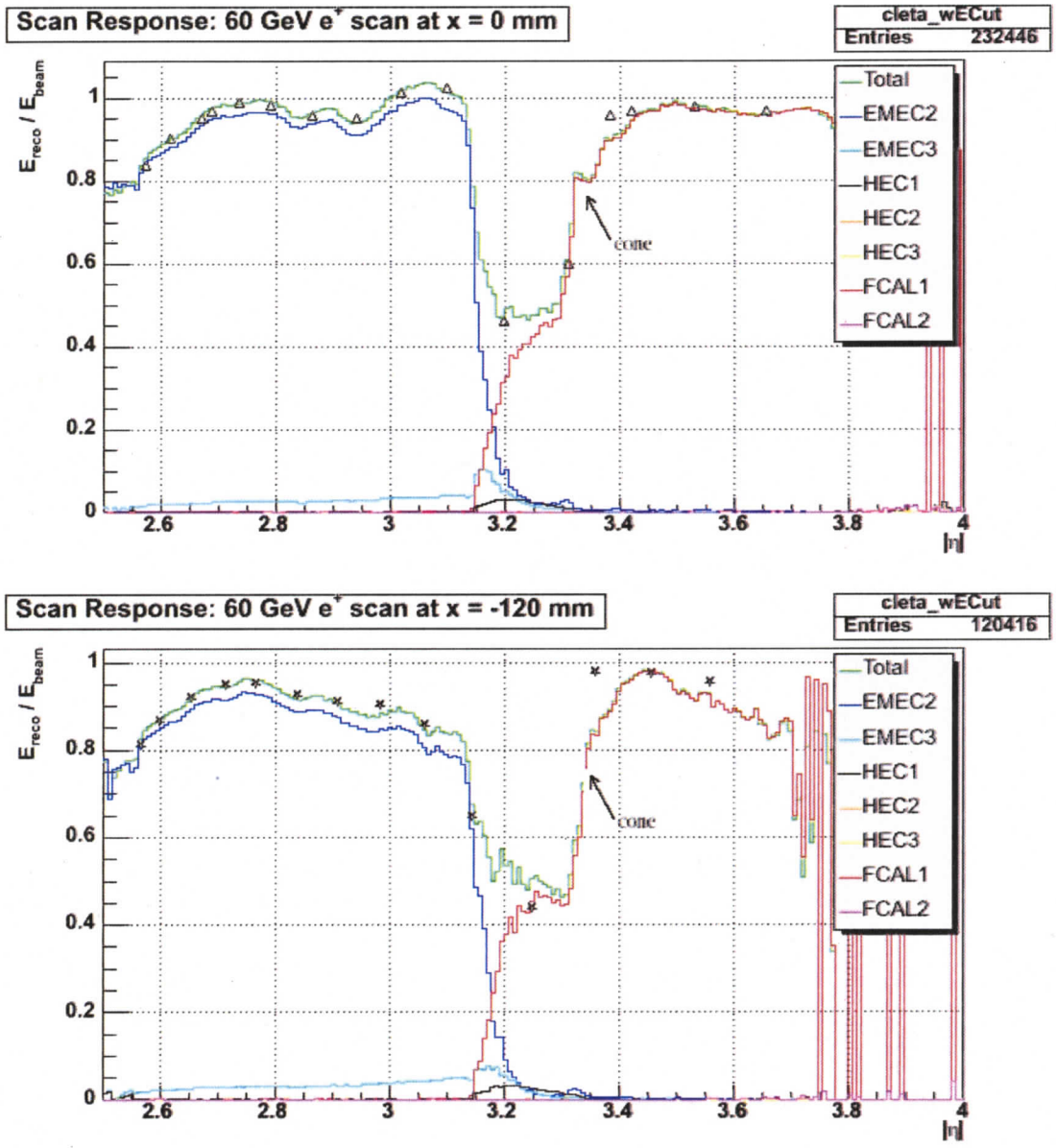

Figure 6.8: Calorimeter response to the 60 GeV positron y-scan at $x = 0$ mm (top) and the 60 GeV positron y-scan at $x = -120$ mm (bottom) as a function of mean cluster pseudorapidity. The total cluster energy is shown (green), along with the cluster energy in each sampling layer. The data points are the energy response at the impact points.

and the other coloured lines indicate the amount of the cluster energy in each of the calorimeter samplings. The total energy is dominated by energy depositions in the front layer of the EMEC and the FCAL. The "super3D" nature of the topological clustering is evident in the transition regions as energy is shared across all three end-cap calorimeters. Again, the three y-scans at $x = 0$ mm with different beam energies all show the same response. The 60 GeV y-scan at $x = -120$ mm clearly shows the response fall-off in the EMEC, and it also shows the same behaviour in the FCAL. This is presumably due to energy leakage out the side of the FCAL modules.

With these more finely-binned response plots, the extent of the 40-55% drop in response in the transition region is more evident. Recall that there exists a small separation between the bottom of the EMEC and the cone that is filled with liquid argon in the testbeam setup. Beam particles interacting within this region are depositing energy in the LAr filling this region, but that energy is not sampled. Hence, a large drop in the response is seen. Also note that the cone clearly shows up as the small dip at $|\eta| \approx 3.3$. On the high-η side of the cone there is a liquid argon excluder preventing this region from being filled with liquid argon, and so the energy of events in this region is mainly deposited in the FCAL1 module.

Resolution

Returning to the bottom plot of figure 6.6, the resolution computed for each data point in the four $e^{\pm}$ y-scans are plotted as a function of pseudorapidity. The resolution in

the central regions of the EMEC and the FCAL is flat in η. The FCAL1 resolution obtained for the 193 GeV y-scan is approximately 4%, which is in good agreement with a previous FCAL stand-alone testbeam where a resolution between 4% and 5% is seen in FCAL1 for the same beam energy [43]. The topological clustering approach used in the current testbeam, where the clustering thresholds are seed = 4, neighbour = 2, and other = 0 (i.e. *T420* clustering), was also used in the FCAL stand-alone testbeam.

In the central region of the EMEC, the resolution obtained with the highest beam energy is approximately 2.5%. A previous EMEC inner wheel testbeam experiment [40] achieved an average resolution of $\sigma/E = 1.29\%$. The discrepancy can be attributed to differences in clustering[7]. Also, the missing HV-dependent correction for the EMEC (see section 5.6) is presumably a factor as well.

At the top of the EMEC IW the resolution is a few percent worse due to the inclusion of more HEC cells in the topological clustering. Including more cells adds more noise which increases the spread in the energy reconstruction. The energy resolution in the transition region ($|\eta| \sim 3.2$) is significantly degraded, with values ranging from 18% to 35%.

[7]The energy reconstruction in previous EMEC IW testbeam is tailored for EM showers in just one detector, whereas the approach taken for the 2004 testbeam uses topological clustering (super3D T420) for energy reconstruction across multiple detectors. The EMEC resolution can be improved by tuning the clustering thresholds from T420 clustering to T633, and by clustering in the EMEC layers only ("all3D" as opposed to "super3D" clustering). This ensures clusters are seeded by cells with higher energy density, and it reduces the number of other cells added to the cluster. The EMEC resolution in the current testbeam improves from 2.5% to 1.8% with this level of clustering.

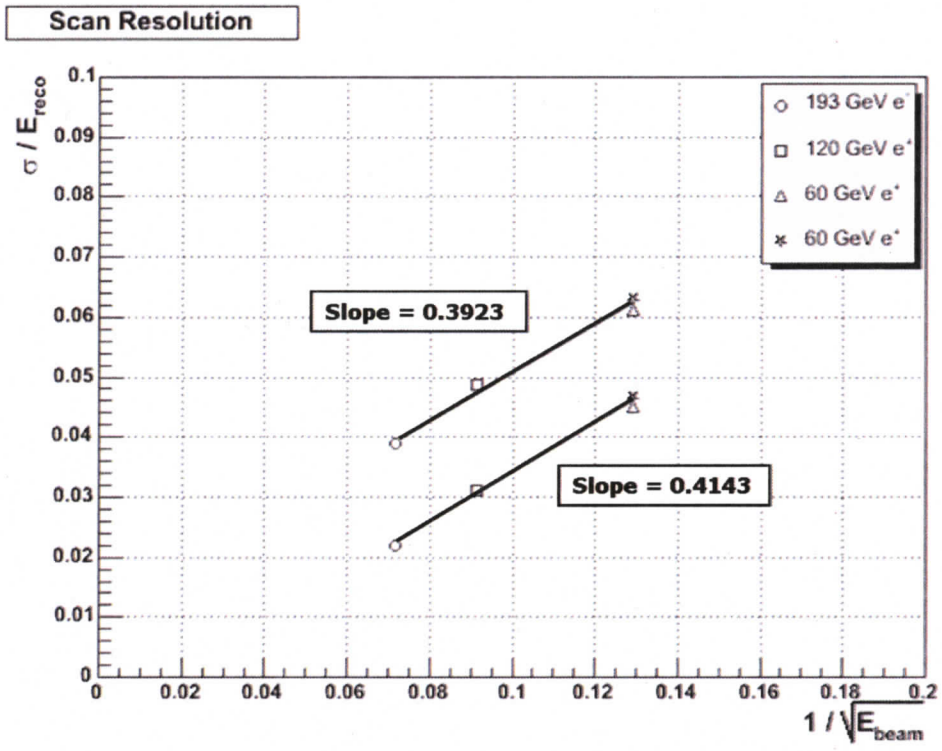

Figure 6.9: Calorimeter resolution as a function of beam energy for two of the y-scan impact points. The top data points at each energy correspond to the impact point at $y = -150$ mm ($|\eta| = 3.5$) in the FCAL1 module, and the bottom data points are for the runs at $y = 150$ mm ($|\eta| = 2.65$) impacting the EMEC.

The resolution improves with beam energy[8], as is expected with sampling calorimeters. By plotting the resolution as a function of $1/\sqrt{E_{\text{beam}}}$ in figure 6.9, a linear dependence (to first order) is observed in both the FCAL (top data points)

[8]The resolution of calorimeters is typically parameterized as

$$\frac{\sigma}{E} = \frac{a}{\sqrt{E}} \oplus \frac{b}{E} \oplus c, \tag{6.2}$$

where the first term is called the sampling or stochastic term, the second term is the noise term, and the third is the constant term. The sampling term is typically the most important limitation to the energy resolution of sampling calorimeters at low energy [15]. Therefore, the resolution of the calorimeters in these studies is expected to be proportional to $1/\sqrt{E}$.

and the EMEC (bottom data points). Although the plots are linear, the values of the slopes are larger than found in previous stand-alone beam tests of the EMEC and FCAL1 [23]. This is expected because of the clustering approach used here: by allowing clusters to cross calorimeter boundaries ("super3D" T420 clustering), a few large HEC cells with low signal to noise values are often included in the clusters. This degrades the resolution as compared to the values obtained in stand-alone beam tests where the reconstruction is tailored for EM calorimeters.

6.4.1 Calculation of α_{EM} for the EMEC

The electromagnetic scale factor α_{EM} is one of the sub-factors that is used in calculating the reconstructed energy of a cell. As section 5.4 described, this factor is a constant for all EMEC inner wheel channels, and it relates the current produced at a LAr gap to the electromagnetic energy scale. The value that was used in previous EMEC inner wheel testbeams was $\alpha_{\mathrm{EM}} = 526$ MeV/μA. The analysis of data from the present testbeam, discussed above, also uses this value in the calculation of E_{reco}. A calculation of α_{EM} for the EMEC IW is now performed in order to verify and cross-check the value being used. Because the EMEC still requires a correction to be applied to account for the residual η-dependence arising from the HV sectors (see discussion in section 5.6), this calculation is only preliminary; a more rigorous calculation could be made once all the corrections to the EMEC response have been implemented.

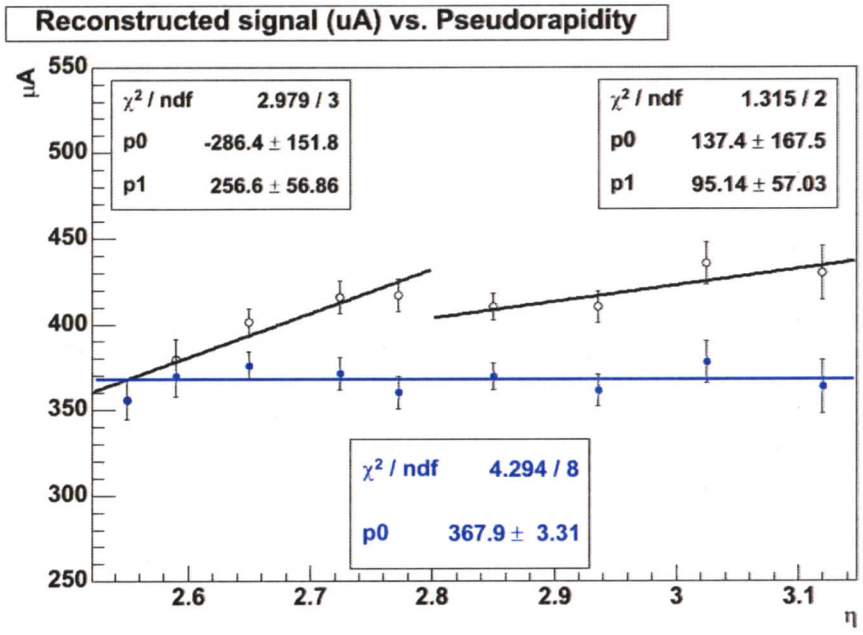

Figure 6.10: The reconstructed signal (in μA) plotted as a function of pseudorapidity for a 193 GeV electron y-scan of the EMEC inner wheel. The data points (open circles) in the two HV sectors are fit with a linear polynomials, which are subsequently subtracted from the data points to remove the η-dependence of the EMEC response. The residual data (solid blue circles) are then averaged to obtain the mean reconstructed signal.

The EM scale factor α_{EM} is obtained from the 2004 testbeam data by relating the current produced in an event to the known beam energy of the incident particle that triggered the event. Therefore, the analysis procedure discussed up to this point in this chapter is used, but rather than converting to the EM scale, the reconstructed signal is left in units of current (μA). Consider the y-scan for the 193 GeV electron beam shown in figures 6.6 and 6.7 as open circles. This same y-scan is shown in figure 6.10 except that the reconstructed signal is kept as current rather than being converted to $E_{\mathrm{reco}}/E_{\mathrm{beam}}$. The η-dependent response due to the two HV sectors

(above and below $|\eta| = 2.8$) needs to be removed in order to have a uniform response. A linear polynomial is fit to the data points in each of the two HV sectors. By subtracting these fits from the data points and scaling the result to the lowest η point (a somewhat arbitrary choice), a new set of data (blue circles) is obtained that has a uniform response. The data are then averaged in order to obtain the mean reconstructed signal $E_{\mu\mathrm{A}}$, which has a value of:

$$E_{\mu\mathrm{A}} = 367.9 \pm 3.31\ \mu\mathrm{A} = 367.9\mu\mathrm{A} \pm 0.9\%. \tag{6.3}$$

The EM scale factor for the EMEC inner wheel is thus computed by relating the reconstructed signal to the nominal beam energy:

$$\alpha_{\mathrm{EM}} = E_{\mathrm{beam}}/E_{\mu\mathrm{A}} = 524.6\mathrm{MeV}/\mu\mathrm{A} \pm 0.9\%. \tag{6.4}$$

Therefore, this preliminary calculation of the EM scale factor for the EMEC IW is in agreement with the value obtained from the previous testbeam experiment. Thus, the use of $\alpha_{\mathrm{EM}} = 526\mathrm{MeV}/\mu\mathrm{A}$ in the analysis of the 2004 testbeam data is justified.

6.5 Pion y-Scan Results

Three pion beams of differing energies are used to perform y-scans of the calorimeters using the same analysis approach as outlined for the electron and positron y-scans. As table 6.2 indicates, the three y-scans under consideration are: a 200 GeV π^- y-scan,

a 120 GeV π^- y-scan, and a 60 GeV π^+ y-scan. All three vertical scans are probing the centers of the calorimeter modules at $x = 0$ mm. Each pion y-scan consists of up to 17 runs impacting at different y-positions, and multiple runs at an impact point are combined together and treated as one large run.

The calorimeter response and the resolution obtained from the pion y-scans are given in figure 6.11. Again, the analysis procedure used in the electron/positron y-scans is also used here: the response is the mean of a Gaussian fit to the energy distribution (divided by the nominal beam energy) of the runs at a given impact point, and the resolution is the width of the fit divided by the mean energy.

Response

From the response plot in figure 6.11, the average response to the pion beam over the entire pseudorapidity range varies from 63.7% for the 60 GeV scan to 70.4% in the 200 GeV case. This reduced response, when compared to $e^{\pm}$ y-scans, is expected because the calorimeters are non-compensating, and the incident pions induce hadronic showers in which some energy is undetectable (section 2.2).

The response to pion y-scans is also not flat across the entire pseudorapidity range. However, the response at $|\eta| < 2.8$ and in the FCAL at $|\eta| > 3.4$ is nearly flat. The response in the transition region is better than in the electron and positron cases because pions have a larger interaction length, and therefore can punch through the dead material to deposit some energy behind it in the HEC. Also, pion showers

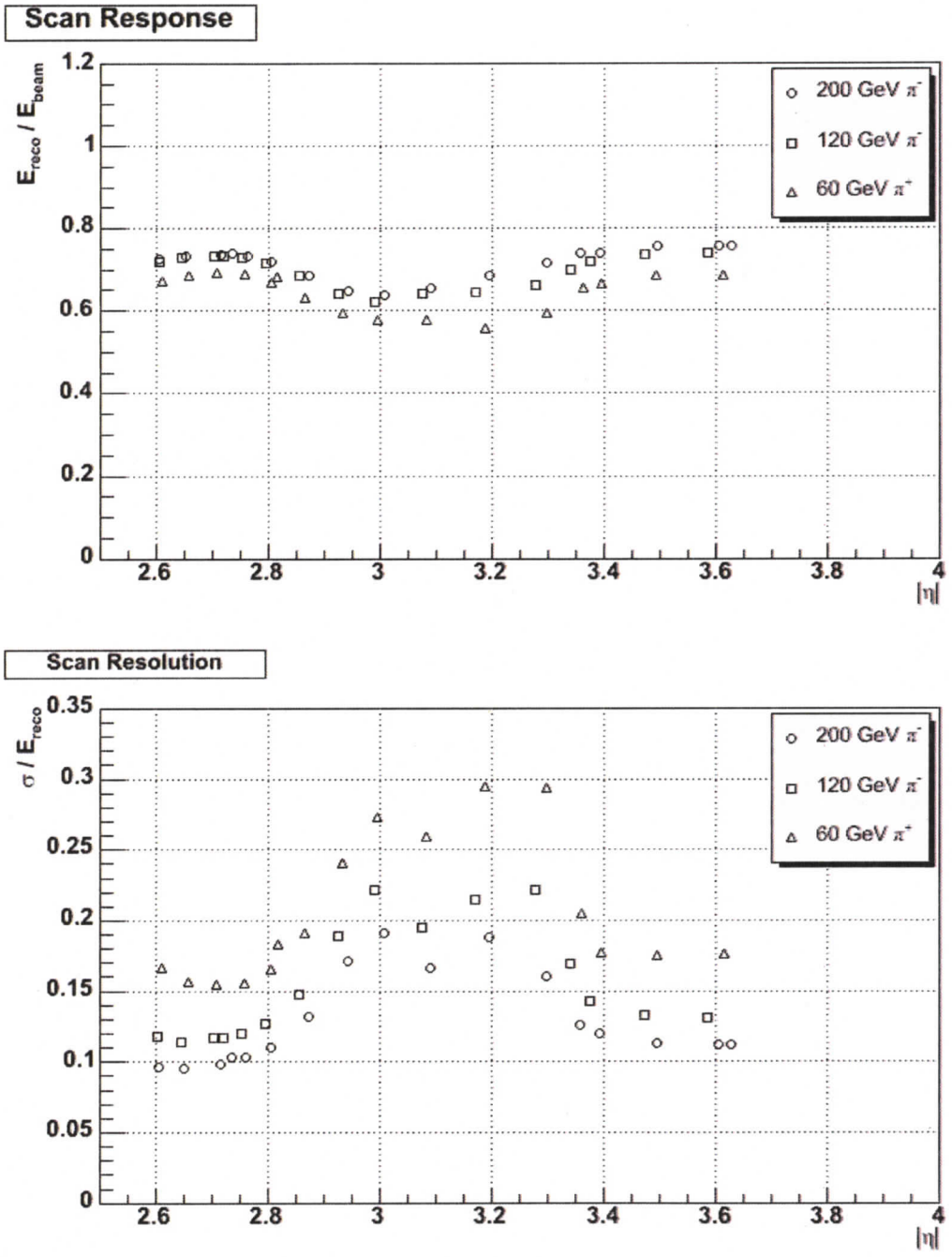

Figure 6.11: Calorimeter response (top) and resolution (bottom) as a function of cluster pseudorapidity to pion vertical scans. All pion scans occur at $x = 0$ mm.

are hadronic which have a larger radial shower spread. Therefore, an incident pion impacting the dead material in the crack region will deposit energy in the cells above and below the crack.

The response in the range $2.8 < |\eta| < 3.2$, for all energies, is the lowest over the full pseudorapidity range. This corresponds to the inner section of the EMEC IW and to the innermost cells of the HEC. In order to more fully understand where the energy of the events is being deposited, continuous energy resolution distributions for each pion y-scan are shown in figure 6.12, where the green line is the average cluster energy and the other coloured lines indicate the amount of cluster energy in each calorimeter layer. (The large bin-to-bin variation at the lowest and highest pseudorapidity is due to lack of statistics in those regions). The first observation is that all calorimeter layers are involved in the reconstruction of hadronic events[9]. However, more striking is the oscillatory nature of the response in the calorimeter layers, which is more prominent at higher energy. According to these y-scans, it appears the electromagnetic component of the hadronic shower is η-dependent. Notice also the anti-correlation between the EM layers and the hadronic layers such that the total cluster response is (relatively) flat. While it is known that the EM fraction of a hadronic shower does fluctuate event-by-event, there is no reason to expect such systematic fluctuations with pseudorapidity. Furthermore, there is no evidence that any of the data runs themselves are in any way different from the other data runs in

[9]The EMEC cells still show η variation (although it is less obvious in the pion plots) in the two HV sectors separated at $|\eta| = 2.8$ because the HV correction is not yet applied.

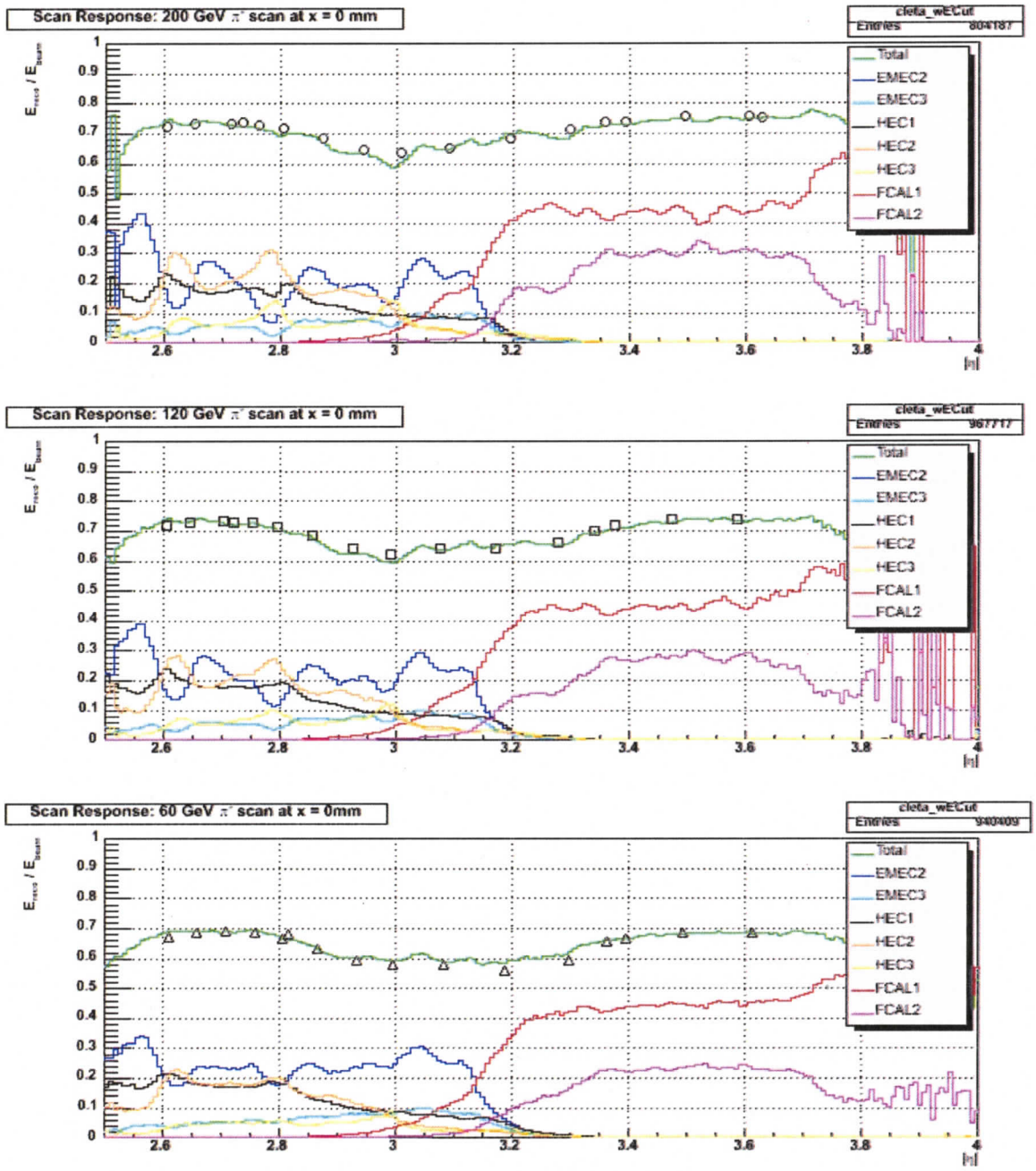

Figure 6.12: Calorimeter response to the 200 GeV π^- y-scan (top), the 120 GeV π^- y-scan (middle), and the 60 GeV π^+ y-scan (bottom) as a function of mean cluster pseudorapidity. The total cluster energy is shown (green), along with the cluster energy in each sampling layer. The data points are the energy response at the impact points.

the y-scan; viewed on their own the individual run data all appear consistent.

Based on these observations, the oscillatory η-dependence of the electromagnetic fraction of the shower is thought to be a binning effect due to the use of the course-grained calorimeter cells used to determine η, and complicated by the slight non-pointing nature of the setup at positions away from the nominal beamline ($|\eta| = 2.95$ in period 2). This hypothesis is supported by response plots of similar position scans performed by CBT-EC2 collaborators that use the beam impact y-position (obtained from the extrapolation of beam chamber position measurements) as the independent variable rather than cluster mean pseudorapidity. Such plots have the same overall total cluster energy, but do not show any η-dependence in the calorimeter sampling layers [27].

Resolution

The resolution obtained for the pion y-scans is given in the bottom plot of figure 6.11. This plot is similar to the $e^{\pm}$ resolution plot in that there are two flat regions with the best resolution (in the EMEC/HEC and in the FCAL), and the transition region shows degraded resolution. At the highest energy, the resolution in the EMEC/HEC is approximately $\sigma/E_{\text{reco}} = 10\%$, and in the FCAL it is 11.5%.

The resolution improves with beam energy, as expected. Figure 6.13 gives the resolution of the three y-scans as a function of $1/\sqrt{E_{\text{beam}}}$ for two of the impact points. As with the $e^{\pm}$ case, the resolution of the pion y-scans in the FCAL (top

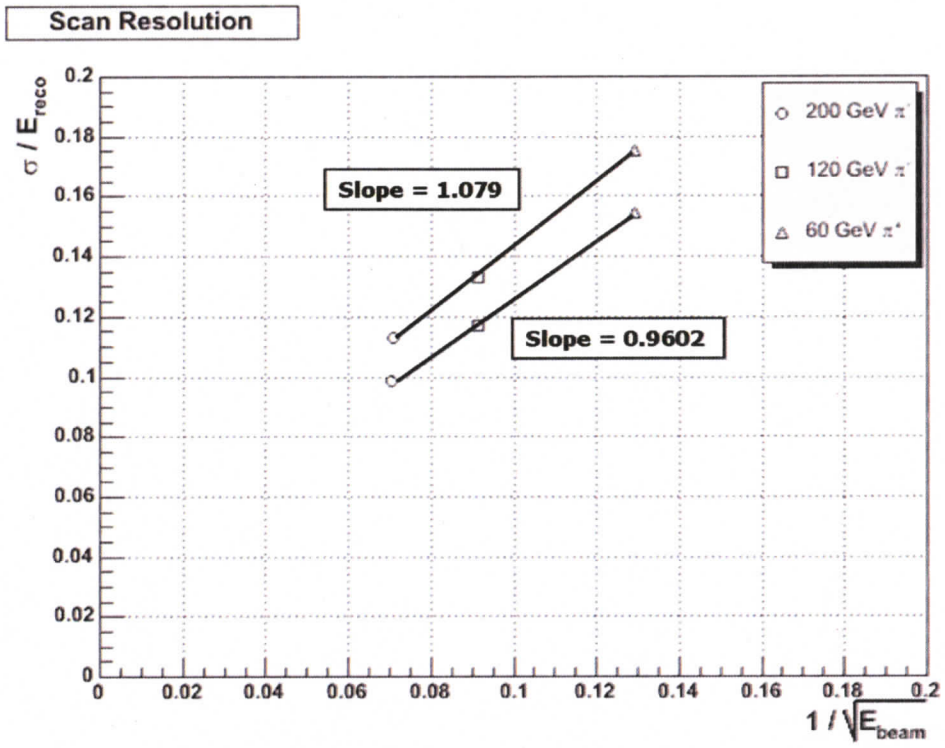

Figure 6.13: Calorimeter resolution as a function of pion beam energy for two of the y-scan impact points. The top data points at each energy correspond to the impact point at $y = -150$ mm ($|\eta| \approx 3.5$) in the FCAL, and the bottom data points are for the pion runs at $y = 150$ mm ($|\eta| \approx 2.7$) impacting the EMEC.

data points) and in the EMEC/HEC (bottom data points) shows a linear behaviour with $1/\sqrt{E_{\text{beam}}}$. The slopes obtained for the sampling term (in equation 6.2) are not as small as in previous testbeams [23]. This is thought to be due to energy leakage, especially out the back of the calorimeters, but it will require further investigation beyond the scope of this thesis.

Chapter 7

Conclusions and Outlook

Beam tests of ATLAS calorimeters have played an important role in preparation for the ATLAS experiment at the LHC. The three end-cap calorimeters, the EMEC, HEC, and FCAL, were simultaneously exposed to particle beams for the first time during the combined beam test (CBT-EC2) at CERN during the summer of 2004. Modules of the three calorimeters, nearly identical in design and function to ATLAS production modules, were exposed to beams of electrons, positrons, pions, and muons with energies ranging from 6 GeV to 200 GeV. These beam tests provide the first opportunity to study the response and performance of the ATLAS end-cap calorimeters in the high pseudorapidity range of $|\eta| > 2.5$, focusing on the transition region between the calorimeters at $|\eta| \sim 3.2$.

This thesis focuses on the calibration and energy response of the end-cap calorimeters. Three different methods of obtaining the ramp calibration coefficients

for the EMEC were tested and evaluated. The central-DAC caliwave method, where a single calibration pulse shape per channel per gain is used to reconstruct the calibration signal peak, was determined as the best method for obtaining ramp coefficients. This method eliminates the bias problem inherent in the parabolic method, and avoids excessive memory consumption required by the multiple-DAC caliwave method.

A calculation of the electromagnetic scale factor (α_{EM}) in the EMEC inner wheel was also performed. This calculation is only preliminary because the reconstructed data still require a correction to account for the residual η-dependent response in the EMEC. The EM scale factor computed is in agreement with the value obtained from a previous stand-alone beam test of the EMEC inner wheel.

Once an accurate calibration was in place, energy reconstruction of data obtained from y-scans was performed. The response ($E_{\mathrm{reco}}/E_{\mathrm{beam}}$) of the detectors to electron and positron y-scans was uniform, very near unity, and was beam-energy independent. The resolution (σ/E_{reco}) obtained for the EMEC and FCAL is slightly worse than previous stand-alone beam tests of those modules (due to clustering differences), but does improve with beam energy and is linear in $1/\sqrt{E_{\mathrm{beam}}}$. The response to pion y-scans was also uniform and beam-energy independent, and the resolution also improves with beam energy and is linear in $1/\sqrt{E_{\mathrm{beam}}}$. For all vertical scans, however, the transition region near $|\eta| \sim 3.2$ degraded the response and resolution, especially in electron and positron y-scans. The sources of dead material responsible for reducing the response and degrading the resolution are the EMEC support struc-

ture, the FCAL cone, and the liquid argon that filled the region between the EMEC and the cone.

In order to move forward with the analysis of the testbeam data, further work is required. First, the EMEC data require the correction to be applied in order to remove the residual η-dependence of the response. Once that correction is applied, a uniformity of response study could be performed in the EMEC. Obviously, the transition region between the three calorimeters requires further investigation. In order to more fully understand the effect of the dead material in this region, detailed Monte Carlo studies are needed. Specifically, the Monte Carlo studies will require accurate geometry information regarding the dimensions of the support structure in order to accurately simulate the testbeam setup. A Monte Carlo study would also help disentangle response effects due to the specific testbeam geometry from features of this transition region that can be expected in ATLAS.

References

[1] D.J. Griffiths, *Introduction to Elementary Particles*, John Wiley & Sons Inc., 1987.

[2] Particle Data Group, *Review of Particle Physics*, Physics Letters B, 592:1-1109, 2004.

[3] LHC conceptual design report. CERN/AC/95-05, 1995.

[4] ATLAS Collaboration, *ATLAS Letter of Intent*, CERN/LHCC/92-4, 1992.

[5] ATLAS Collaboration, *ATLAS detector and physics performance technical design report*, CERN/LHCC/99-15, May 1999.

[6] M. Lefebvre, Private communication, *Physics at the Large Hadron Collider*, Lake Louise Winter Institute, http://hepweb.phys.uvic.ca/~lefebvre/talks/lectures/, February 2005.

[7] E. Eichten et al., *Supercollider physics*, Reviews of Modern Physics, 56:579-707, 1984.

[8] B. Aubert et al., *Performance of the ATLAS electromagnetic calorimeter end-cap module 0*, Nuclear Instruments and Methods in Physics Research A, 500:178-201, 2003.

[9] B. Dowler et al., *Performance of the ATLAS hadronic end-cap calorimeter in beam tests*, Nuclear Instruments and Methods in Physics Research A, 482:94-124, 2002.

[10] J.C. Armitage et al., *Electron Results fro the ATLAS Electromagnetic Forward Calorimeter Module 0 Test Beam 1998*, ATL-LARG-2003-011.

[11] C. Cojocaru et al., *Hadronic calibration of the ATLAS liquid argon end-cap calorimeter in the pseudorapidity region* $1.6 < |\eta| < 1.8$ *in beam tests*, Nuclear Instruments and Methods in Physics Research A, 531:481-514, 2004.

[12] T. Ince, *Position Resolution of the ATLAS Electromagnetic Endcap Calorimeter*, Master's Thesis, University of Victoria, 2005.

[13] T.M. Hughes, *Pion Energy Reconstruction Methods for the ATLAS Electromagnetic and Hadronic Endcap Calorimeters*, Master's Thesis, University of Victoria, 2005.

[14] ATLAS Collaboration, *Liquid Argon Calorimeter Technical Design Report*, CERN/LHCC/96-41, 1996.

[15] C.W. Fabjan and F. Gianotti, *Calorimetry for particle physics*, Reviews of Modern Physics, 75:1243-1286, 2003.

[16] R. Wigmans, *Calorimetry: Energy Measurement in Particle Physics*, Oxford Clarendon Press, 2000.

[17] C. Grupen, *Particle detectors*, Cambridge University Press, 1996.

[18] S. Menke, Private communication, *Overview on Hadronic Calibration Approaches*, ATLAS Hadronic Calibration Workshop, http://agenda.cern.ch/fullAgenda.php?ida=a054396, July 2005.

[19] U. Amaldi, *Fluctuations in calorimetry measurements*, Physica Scripta, 23:409-424, 1981.

[20] P. Barrillon et al., *Electrical tests for the validation of the electromagnetic endcap calorimeter modules*, ATL-LARG-2003-004.

[21] ATLAS Collaboration, *Calorimeter Performance Technical Design Report*, CERN/LHCC/96-40, 1997.

[22] F. Djama et al., *Copper-Polyimide Multi-Layer Electrodes for the End-Cap Electromagnetic Calorimeter*, ATLAS LArg Note 88, December 1997.

[23] P. Puzo, *ATLAS Calorimetry*, Nuclear Instruments and Methods in Physics Research A, 494:340-345, 2002.

[24] CERN Experimental Areas Section, *Short introduction to the use of the h6 beam*, Version 3.0, http://ab-div-atb-ea.web.cern.ch/ab-div-atb-ea/BeamsAndAreas/h6/H6manual.pdf, May 2000.

[25] P. Gorbunov, Private communication, *ITEP Beam Chambers*, CBT-EC2 Meeting, http://agenda.cern.ch/fullAgenda.php?ida=a036104, November 2003.

[26] L. Kurchaninov and J. Rutherfoord, Private communication, *CBT-EC2 "Crack" Studies: Where is the Crack?*, Combined Testbeam Meeting EC2, ATLAS LAr Week, http://agenda.cern.ch/fullAgenda.php?ida=a042229, June 2004.

[27] M. Bieri, *Study of the 2004 End-cap Beam Tests of the ATLAS Detector*, Master's Thesis, Simon Fraser University, 2006.

[28] M. Vincter, Private communication, *LArg Pulse Accumulation for EC2*, Combined Testbeam Meeting EC2, ATLAS LArWeek, http://agenda.cern.ch/fullAgenda.php?ida=a052748, May 2005.

[29] M. Lefebvre and R. McPherson, Private communication, *Event Phase Reconstruction*, Combined Testbeam Meeting EC2, ATLAS LAr Week, http://agenda.cern.ch/fullAgenda.php?ida=a043764, September 2004.

[30] W.E. Cleland and E.G. Stern, *Signal processing considerations for liquid ionization calorimeters in a high rate environment*, Nuclear Instruments and Methods in Physics Research A, 338:467-497, 1994.

[31] R. McPherson, Private communication, *Signal Reconstruction using physics pulse shapes in CBT-EC2*, Combined Testbeam Meeting EC2, ATLAS LAr Week, http://agenda.cern.ch/fullAgenda.php?ida=a052748, May 2005.

[32] R. McPherson, Private communication.

[33] J. Rutherfoord, Private communication.

[34] M. Aleksa et al., *2004 ATLAS Combined Testbeam: Computation and Validation of the Electronic Calibration Constants for the Electromagnetic Calorimeter*, ATL-COM-LARG-2006-003.

[35] P. Schwemling, Private communication.

[36] P. Pralavorio and F. Djama, Private communication.

[37] P. Pralavorio, Private communication.

[38] P. Strizenec, Private communication.

[39] B. Aubert et al., *Performance of the ATLAS electromagnetic calorimeter end-cap module 0*, Nuclear Instruments and Methods in Physics Research A, 500:178-201, 2003.

[40] P. Barrillon et al., *Uniformity Scan in the Inner Wheel and the crack between the two wheels (η = 2.5) of the Electromagnetic End-cap Calorimeter*, ATL-LARG-2001-014.

[41] P. Barrillon et al., *Uniformity Scan in the Outer Wheel the Electromagnetic Endcap Calorimeter*, ATL-LARG-2001-012.

[42] R. Keeler and R. McPherson, Private communication.

[43] M. Schram, Private communication, *FCal Test Beam 2003 Energy Resolution*, Combined Testbeam Meeting EC2, ATLAS LAr Week, http://agenda.cern.ch/fullAgenda.php?ida=a055691, September 2005.